Combined theoretical and experimental study of the core-level electronic structure of ionic liquids

by

Ekaterina Gousseva

Submitted for the degree of Doctor of Philosophy

January 2023

Research Supervisors:

Dr Kevin R. J. Lovelock

Dr Ricardo Grau-Crespo

Department of Chemistry School of Chemistry, Food and Pharmacy

Declaration

I confirm that this is my own work and the use of all material from other sources has been properly and fully acknowledged.

Ekaterina Gousseva

To *Him*, whom I cannot thank enough

"But the Lord stood with me and gave me strength" 2 Timothy 4:17

Acknowledgements

To my main supervisor Dr K. R. J. Lovelock, who has always been generous to his students with his time, in many long, helpful discussions. For striking the right balance of support and freedom to be independent throughout his supervision. I am honoured to be your second official PhD student.

To my second supervisor, Dr R. Grau-Crespo, for always having my best academic interests at heart in his guidance. For his regular meetings, and always providing however much support I required at any given moment.

To collaborators and beam line scientists: Dr R. A. Bennett, Dr D. Duncan, Dr R Seidel and others, for their incredibly hard work and expertise, especially on beam times.

I am extremely grateful to the Royal Society for their ample funding in my studentship, allowing me to make the absolute most of these four years, where circumstances have allowed. Thank you to the UK Materials and Molecular Modelling Hub, Materials Chemistry Consortium and EPSRC for ARCHER, ARCHER2 and Young computing time.

To SDM, for treating my interests as his own in his enthusiastic mentorship during the time our PhDs overlapped and beyond.

To SG, for always being ready to be my cheerleader, not only through this monumental undertaking but consistently throughout our PhDs.

To JSM, for companionship and many a laugh in office and (seemingly endless) beam times.

And to HJS, for his unwavering encouragement, and for creating a stable environment from which I could flourish. I will always be grateful.

To those, whom I owe the most -

My dearest *mamma*, who paved the way to where I am today, in many more ways than one. For her truly unconditional love.

To my incredible grandparents and great-grandparents, models in seemingly endless faith, determination, grit and loyalty.

To OAP, godfather, OP and AAZ, through whom I have received so much love and light.

Finally, to my great grandma, who always wanted a *doctor* in the family.

Abstract

Ionic liquids (ILs) are a group of materials, composed solely of ions, which exist in their liquid state at functional temperatures *i.e.*, ≤100 °C. ILs are novel fluids which can exhibit unique combinations of desirable properties, compared to traditional molecular liquids. This ability means there is much interest in their use for a vast range of applications, from the most specialised to the most common, such as solvents, catalysis and energy storage or conversion. To employ a new material in any application, a thorough understanding of its nanoscopic and macroscopic behaviours is imperative. In ILs, the nanoscopic environment is far more complex than a molecular liquid. These materials consist of two different ions at minimum. To be liquid at low temperatures, the ions tend to be bulky or asymmetric. Furthermore, an extensive choice of ions produces an immense estimate of 10^6 potential ILs. Together, these attributes make the fundamental study of ILs and their electronic behaviours more intriguing than that of a typical liquid. One prominent experimental method used to study these behaviours is X-ray photoelectron spectroscopy (XPS). The core levels can be investigated to examine binding energy (E_B) shifts and peak widths to gather information on the system such as composition and chemical states. Further information, such as bonding, local geometric structures or oxidation states can only be hypothesised. In this thesis, a combined theoretical and experimental approach is used to investigate the nature of E_B shifts of ILs. This combined approach allows a more comprehensive analysis than would be possible with either method alone. In particular, an approach employing density functional theory (DFT) enables effective electronic simulation to complement the experimental data. ILs are studied in the bulk form and at an interface with a titanium dioxide (TiO_2) surface. It is first determined that the initial, ground state, of the IL system is the dominant influence in measured XPS peaks. The complex interplay of the various types of interactions in the IL system is carefully studied, to demonstrate

that when simulating these complicated systems, long-range interactions are critical to the electronic behaviour and a basic gas phase, lone ion pair approach is insufficient. The method developed to simulate E_B is applied to a further four ILs to demonstrate its validity in predicting component E_B separations. This method is also shown to reproduce peak E_B shifts observed in experiments, establishing for the first time that these shifts originate in the initial state rather than the final state. New XPS and normal incidence X-ray standing wavefield (NIXSW) data is presented for an IL monolayer on a rutile (110) TiO_2 surface. Excellent agreement is found between the experimental and the calculated geometric adsorption structure. Calculations on TiO_2 are further evaluated at a range of scales, from lone ion pair to bulk models, to find that the ions have contrasting preferred adsorption geometries based on the local liquid (or lack thereof) environment. Calculated bond length differences are observed between geometry optimisation calculations at 0 K and *ab initio* molecular dynamics (AIMD) simulations at 298 K and 398 K.

List of publications

I. Experimental measurement and prediction of ionic liquid ionisation energies

J. M. Seymour, E. Gousseva, A. I. Large, C. J. Clarke, P. Licence, R. M. Fogarty, D. A. Duncan, P. Ferrer, F. Venturini, R. A. Bennett, R. G. Palgrave and K. R. J. Lovelock * (*Phys Chem Chem Phys* **2021,** *23* (37), 20957-20973)

II. Resonant X-ray photoelectron spectroscopy: identification of atomic contributions to valence states

J. M. Seymour, E. Gousseva, R. A. Bennett, A. I. Large, G. Held, D. Hein, G. Wartner, W. Quevedo, R. Seidel, C. Kolbeck, C. J. Clarke, R. M. Fogarty, R. A. Bourne, R. G. Palgrave, P. A. Hunt, K. R. J. Lovelock (*Faraday Discuss.* **2022**, 236, 389-411)

III. Understanding X-ray Photoelectron Spectra of Ionic Liquids: Experiments and Simulations of 1-Butyl-3-methylimidazolium Thiocyanate

E. Gousseva, S. D. Midgley, J. M. Seymour, R. Seidel, R. Grau-Crespo and K. R. J. Lovelock (*J Phys Chem B* **2022,** *126* (49), 10500-10509)

Contents

Abbreviations

IL	Ionic liquid
E_B	Binding energy
XPS	X-ray photoelectron spectroscopy
IS	Initial state
FS	Final state
UHV	Ultra-high vacuum
FF	Force field
DFT	Density functional theory
AIMD	*Ab initio* molecular dynamics
VASP	Vienna *ab initio* simulation package
PBE	Perdew-Burke-Ernzerhof
B3LYP	Becke, 3-parameter, Lee–Yang–Parr
CL	Core level
FWHM	Full width half maxima
NISXW	Normal incidence X-ray standing wavefield

1. Introduction

1.1. Background

Televisions, artificial muscles, yarn, diesel engines and renewable energy – what do these all have in common? Ionic liquids (ILs) are playing a valuable role in the improvement or development of the industrial processes related to each of these products.[1-4] Today, there is a massive interest in ILs for a wide array of industrial applications due to their incredible versatility.[5-7] The nature of ionic liquids, liquids created from oppositely charged ions, grants freedom to select from a vast range of ions to create a material with entirely unique and specific properties. With this capability, it becomes possible to find a novel material which improves upon the desirable properties of the traditional material, without sacrificing performance.

Modern day use of the term ionic liquid (IL) is now broadly limited to discussing liquids, made exclusively of ions, which are liquid or have a melting point below 100 °C.[8, 9] The term 'ionic liquid' is used to distinguish a substance that carries all the benefits of a molten salt, while remaining liquid, a more useful state, at less cumbersome temperatures. The melting point of fluids covered under the term 'ionic liquid' is important to note, as "molten salts" melt at temperatures far closer to 400 °C to 800 °C yet could otherwise also be considered "ionic liquids". The material incompatibilities and handling difficulties that accompany the temperatures of molten salts overshadow the potential uses that they have in their liquid state.[10] ILs and molten salts share many of the same advantageous physical and chemical properties, including wide liquid ranges, low volatility, thermal stability and

tuneability. These desirable properties may have lent molten salts to applications that ILs are now considered for, but the practical limitations in their use meant they could not be explored as such.

Ionic liquids were first discovered in 1888,[11] but practical, air- and water-stable combinations appeared in 1992.[12] This discovery triggered a breadth of research into ILs as novel materials for industrial applications. Most notably, these include catalysts, energy storage and solvents. ILs are so versatile that it should be of no surprise that they have also been discovered naturally occurring, but this only happened in 2014.[13] It was recognised that when two species of ants compete, one gets sprayed with the other's venom. The sprayed ant then secretes and washes itself with formic acid, its own venom to counteract the attack. As these two venoms mix, a mixed-cation IL is produced.

The tuneability of ILs enables an estimated 10^6 to 10^{18} possible combinations.[5, 14] Tuneability is not limited to the choice of the cation or anion, or even several of each, but the possibility of any other additives – both organic and inorganic substances are soluble in ILs. This feature is particularly desirable in solvent application and ILs have been termed 'designer solvents'. As solvents, ILs provide unique capabilities: they can be hydrophobic or hydrophilic, slightly acidic or slightly basic, miscible or immiscible and have the ability to solvate and combine unusual reagent pairings.[9] In other applications, ILs provide the option of developing an existing process, making it more efficient, "greener" or improving the product quality.

One example of this development is in the application as anti-static materials - in liquid crystal displays (LCDs), methyl acrylate polymers have been the traditional material of choice, due to their high transparency.[15] During production, it is difficult to avoid contamination with foreign particles and so additives, such as tin oxide, are combined with the material despite the loss of transparency that they produce.[16, 17] ILs have been applied as anti-static agents successfully without loss of transparency in the polymer.[18] Another example can be illustrated by the process of transforming wood pulp into various products, including paper, cellophane or fibres. The dissolution of cellulose has typically involved high temperatures, dangerous side reactions and toxic and explosive solvents.[19-21] Considerable progress has been made in the utilisation of ionic liquids as solvents for cellulosic materials, creating a more green and safe process.[22, 23]

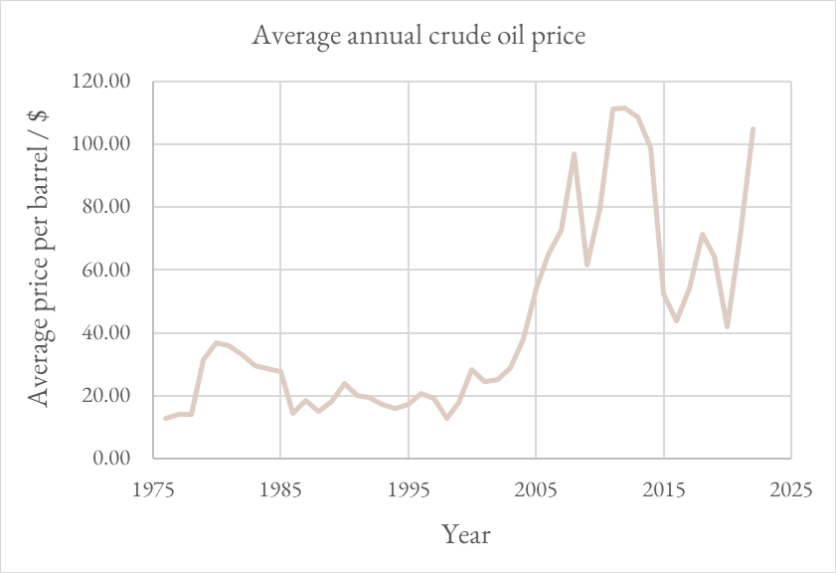

Figure 1.1 A plot of the average annual price of crude oil, per barrel, from 1976 to 2022.

Interest in ILs extends a great deal further; uses in liquid separation[24], carbon capture, gas sensing and energy conversion, for example. Crude oil – the raw material of many materials used traditionally in this immense variety of industrial applications[25] – is diminishing in supply and is famously volatile in price, particularly at the time of this writing (Figure 1.1). [26] The price stability of ionic liquids is potentially even more advantageous to large-scale processes in industry. A more comprehensive collection of the desirable properties that ILs can exhibit are illustrated in Figure 1.2. [7, 27]

It should be noted that ILs do not always offer an improvement in safety, environmentally friendly or "green" metrics, compared to the traditional material used in any given application. ILs do exhibit their own disadvantages and challenges, which makes it necessary to consider all aspects of the process' lifecycle to determine the real "benefit-cost" of employing these materials.[28, 29]

1.2. Bulk ionic liquids

It is the uniquely broad range of environments and interactions in an IL that enables the extraordinary potential for many properties and uses in these materials.[30] The short-range and long-range interactions are highly influenced by geometric structure. Consisting of a minimum of two entities, which are charged and often asymmetrical, the complexity of the microenvironments in these liquids is far higher than that of molecular liquids, *i.e.* only a single entity.[31] Due to the nature of ILs, polarisation and electron sharing behaviours between the ions can be expected. Partial charge transfer (CT) is a term used to characterise the complex nature of the anion-cation interactions.[32] This phenomenon describes charge movement or sharing between the cation and the anion in an IL. The phenomenon of CT has been discovered computationally[33-35] in the form of non-integer ion charges, but it has also been observed experimentally.[36] It has not been determined whether this effect is caused mostly by polarisation or orbital mixing.[32, 37-39] It is clear, however, that the extent of CT is strongly influenced by the choice of cation and anion in an IL. CT behaviour has been related to ion qualities, such as anion Lewis basicity[36], geometry or hydrogen bonding ability.[40]

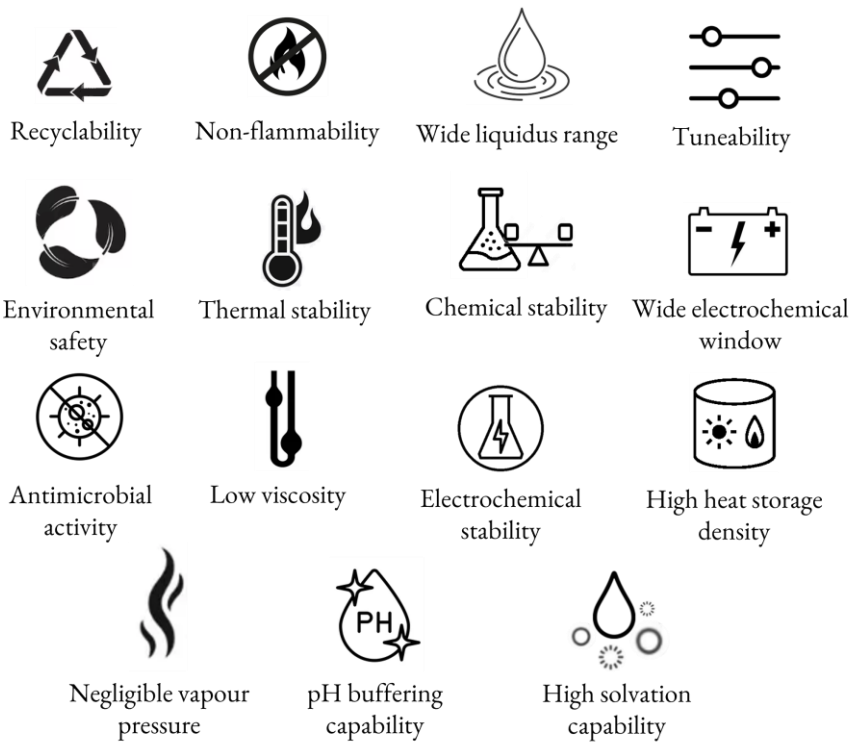

Figure 1.2 A scheme detailing many of the properties that ILs can exhibit, which make these materials so desirable in industrial applications.

In addition to the complexity of the intermolecular (or "interionic", *i.e.* between the cation and the anion) interactions, the seemingly endless cation and anion designs make it very difficult to characterise ILs. Much of the research into these liquids is based on attempting to understand how these fundamental features relate to the bigger picture. This bigger picture involves directly relating the choice of the cation and the anion to their physical and chemical properties[41], and the outcomes desired at application.

An adjustment in geometric structure engages electrons in the system, causing "shifts" in their behaviours. Valence electrons take part in intramolecular bonding and interionic interactions described above, which dictate the macroscopic properties of the material. Valence electron behaviour is particularly important where electrons are added or removed: reactivity, electrochemistry, and photochemistry. Core and valence electrons and their effects on one another are intertwined. Core level energies are directly related to the valence electronic structure, and any shifts in these core energies indicate a change in the atomic environment. An overall picture consisting of both valence and core behaviours is ideal for developing robust methods of predictive selection of ILs for any given application. Thus, deconvolution of electronic behaviours can be seen as the first step in a collaborative sequence of prediction, synthesis, and engineering. Two means of investigation are implemented in research based on ILs – macroscopic, measurements of physical and chemical properties or microscopic, using spectroscopic techniques or computational calculations to learn electronic behaviour trends.

This work focuses on the fundamental study of ILs in bulk and interfaces. X-ray photoelectron spectroscopy (XPS) is employed symbiotically with computational methods to investigate the origin of core level energy shifts and changes in response to cation choice, anion choice and the introduction of a surface. Validation of the XPS technique as an accurate method to probe ground state behaviours is demonstrated. Adsorption geometries and interactions are deconvoluted through calculation and normal incidence X-ray standing wavefield (NIXSW) experiments. A computational simulation method is developed and tested to be applied in future work on a wider selection of ILs.

1.3. Ionic liquids and surfaces

At a surface, the molecules of a liquid face a whole new environment compared to their bulk form. They have contact with either air, vacuum, or another material, have far fewer ionic liquid 'neighbours' and a different density. It is logical to expect these changes to directly impact the nanoscopic behaviours, physical and chemical properties of the liquid. One of the most common IL-surface systems are those of energy storage applications. The interest in ILs for various roles in different types of these systems is vast.[42-57] They are explored as either pure electrolytes or as additives to organic electrolytes. ILs have been found to improve safety, energy density and lifetimes compared to traditional electrolytes.[58-60]

Titanium dioxide (TiO_2) is a semiconductor, and in its various polymorphs, it is one of the most commonly studied materials in surface science and it is the most studied metal oxide.[61, 62] In particular, it has a range of functions in energy storage and conversion.[63-71] A well-researched material offers a known foundation while investigating new phenomena. TiO_2 has four common polymorphs: rutile, anatase, brookite and TiO_2-B. Of these, rutile in bulk form is the most thermodynamically stable. Particularly in its rutile form (Figure 1.3), TiO_2 is easily obtained and inexpensive. Of the rutile surfaces, the (110) surface is the most thermodynamically stable, and it has been calculated as having the lowest surface energy at 0 K.[72]

The nature of ILs and the popularity of TiO_2 together make a strong case for investigating their complex interface. In this thesis, the interface of TiO_2 and the ILs 1-ethyl-3-methyl-imidazolium thiocyanate $[C_2C_1Im][SCN]$ and 1-butyl-3-methyl-imidazolium thiocyanate $[C_4C_1Im][SCN]$ was explored both computationally, using first principles methods, and experimentally, using X-ray photoelectron spectroscopy (XPS) and normal incidence X-ray standing wavefields (NIXSW).

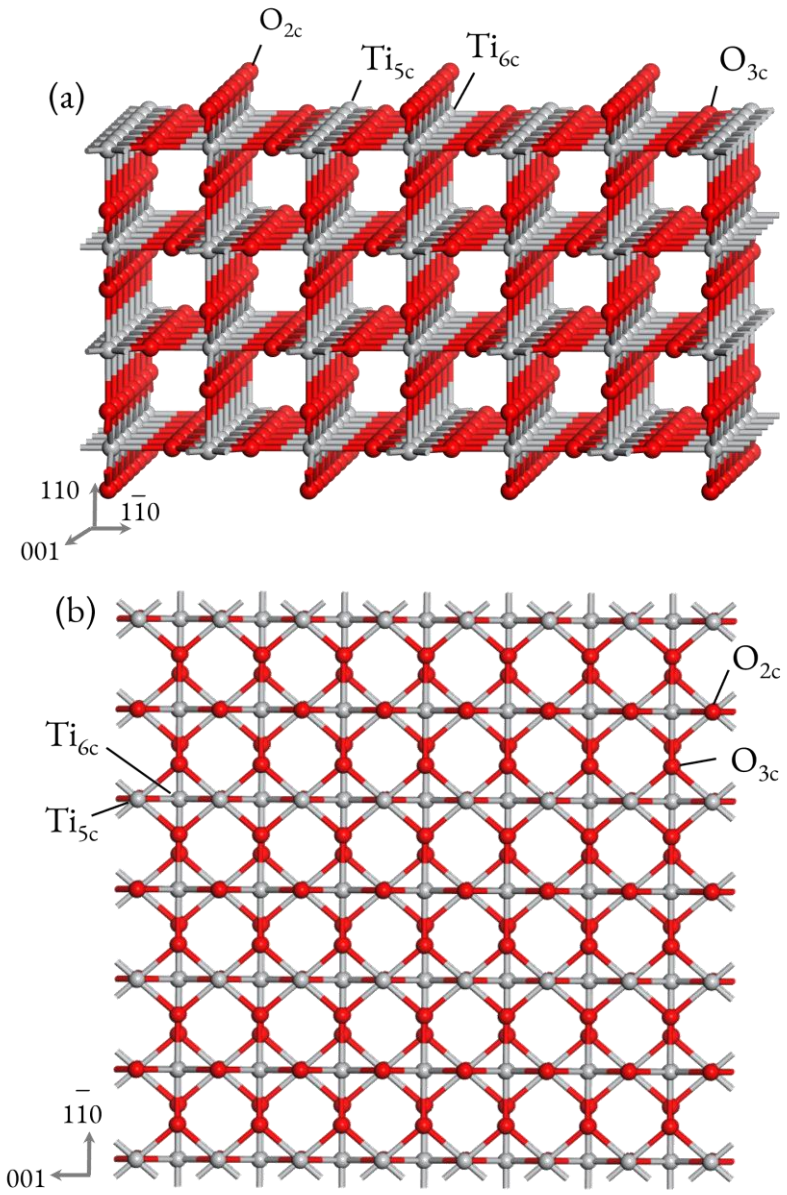

Figure 1.3 A visual representation of the TiO_2 rutile structure, cleaved at the (110) surface, from two viewpoints. Atoms are labelled by their coordination.

1.4. Imidazolium-based ionic liquids

The work presented in this thesis focuses exclusively on imidazolium-based ILs. This group of ionic liquids is defined by the presence of an imidazolium (Im) ring within the cation of an IL (Figure 1.4a). The first of these ILs to be synthesised was 1-ethyl-3-methylimidazolium tetrafluoroborate

$[C_2C_1Im][BF_4]$ in 1992,[12] and so Im-based ILs led the way for the "second generation" of these materials.[5] Since their discovery, this group of ILs has become the most widely studied, both experimentally and theoretically.[33, 41, 73, 74]

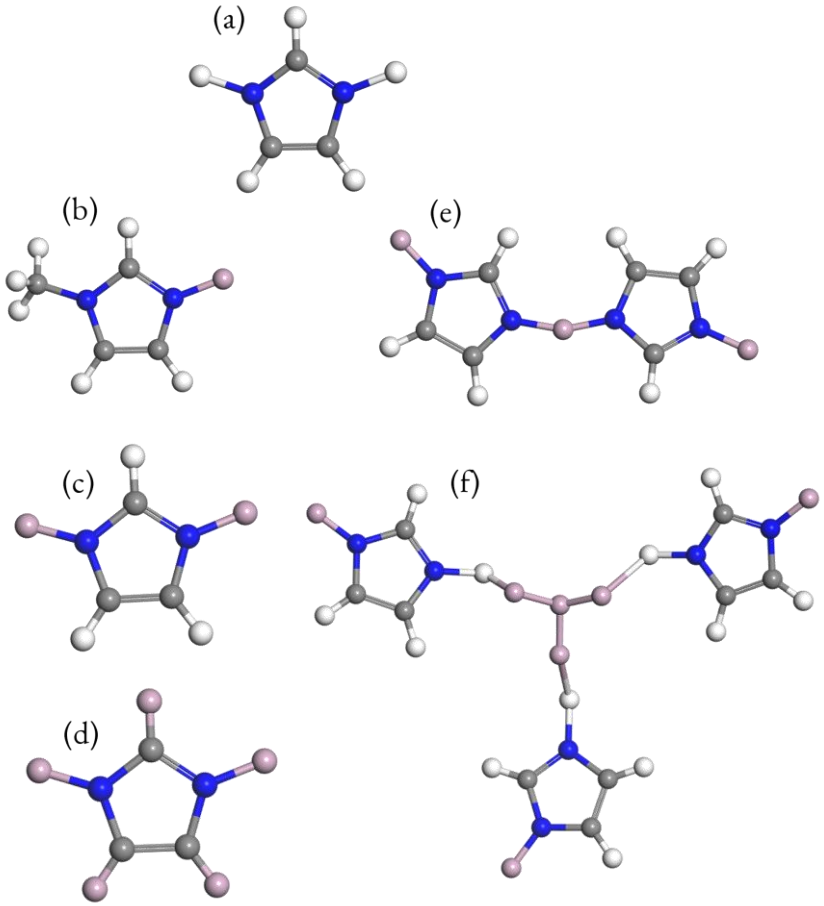

Figure 1.4 A scheme illustrating some synthesized Im-based cation designs. Blue denotes a nitrogen atom, grey a carbon atom, white a hydrogen atom and pink denotes an R-group, which could be any group consisting of carbon, nitrogen, or hydrogen. Charges are omitted for simplicity. Structures that are included are (a) imidazolium (b) disubstituted Im cation, in the notation $[C_nC_1Im]^+$, where R is an alkyl chain of *n* carbons, ≥2, (c) $[C_nC_nIm]^+$ where R is an alkyl chain of *n* carbons, ≥2, (d) fully substituted Im, (e) dicationic moiety, (f) tricationic moiety.

These ILs are relatively cheap, easily prepared, easily modified and have convenient melting points.[5] They have been found to demonstrate superior properties, such as radiation and electrochemical stability.[75, 76] The most common Im-based cation is the disubstituted 1-*alkyl*-3-methylimidazolium,

$[C_nC_1Im]^+$, (Figure 1.4b), where typically n = 2, 4 or 8. Due to their versatility and universality among this area of research, ILs with these cations were chosen for investigation in the present work. The Im core of this cation allows for a vast variety of functionalisation. The Im ring can, for example, be substituted with alkyl groups where $n \geq 2$ (Figure 1.4c) or, it may be fully substituted (Figure 1.4d). Substitutions may be alkyl groups or functionalised groups. Fully substituted Im-based ILs have increased electrochemical and thermal stability.[77]

Another route that has been investigated is joining Im-based cations *via* linkers to produce dicationic ILs (Figure 1.4e).[78] This approach adds several dimensions to the tuneability of these cationic moieties; the same or different cations may be linked, and the choice of linker (alkyl chain length) also affects the result. These have been investigated in organic synthesis[79], catalysis[80] and as solvents. In tricationic moieties (Figure 1.4f), the central moiety can also vary.[81, 82] These large molecules have found success as stabilisers for palladium nanoparticles.[81]

1.5. Aims and objectives

The main aim of this work is to contribute to the development of methods combining theoretical and experimental approaches to further understand the core-level electronic behaviours of ILs. The popular and most commonly-studied IL $[C_4C_1Im][SCN]$ is the focus throughout the thesis, with a brief venture into a selection of others (1-butyl-3-methylimidazolium bis(trifluoromethylsulfonyl)imide, $[C_4C_1Im][NTf_2]$, 1-octyl-3-methylimidazolium bis(trifluoromethylsulfonyl)imide, $[C_8C_1Im][NTf_2]$, 1-octyl-3-methylimidazolium thiocyanate, $[C_8C_1Im][SCN]$ and 1-octyl-3-methylimidazolium chloride, $[C_8C_1Im][Cl]$) for further method validation in Chapter 5. The results presented throughout contain theoretical calculations validated and compared to experimental results, both original data and data published by the group previously.

The work presented here is limited to fundamental research of these materials, to broaden the range of tools available to be applied where there is interest in proceeding with application-based research and materials engineering.

The specific aims of this thesis are;

I. To elucidate the source(s) of binding energy fluctuations within a single IL system, a result of complex cation-anion interactions.
II. To test the ability of *ab initio* methods in predicting core-level binding energies in ILs.
III. To investigate the validity of a range of computational model scales in replicating experimental results of bulk ILs and ILs on a semiconductor surface, of both XPS and NIXSW.

1.6. Thesis outline

The thesis begins by exploring the background and the general insights into the topic. This is followed by an overview of the methods utilised in the research that follows. The results chapters in this thesis are organised based on the progression of the research. Chapter 4 reports the results of a series of investigative DFT calculations on the complex bulk system of $[C_4C_1Im][SCN]$ to correlate the core-level binding energies with various aspects of the liquid. The method that is published[83] is applied in the work reported in Chapters 5 and 6. Chapter 5 builds on the work of the previous chapter, demonstrating that the method is valid across a variety of ILs. Chapter 6 delves into some materials science, equally weighted between calculations and experiments of $[C_4C_1Im][SCN]$ on a TiO_2 surface. Finally, general conclusions of the work are discussed, supported by ideas for future work for the further development of this research.

2. Experimental methods

2.1. X-ray Photoelectron Spectroscopy

2.1.1. Introduction

X-ray Photoelectron Spectroscopy (XPS) is an analytical technique developed based on the theory of the *photoelectric effect*, described by Einstein in 1905[84], which won him a Nobel Prize in 1921. The method, to measure binding energies (E_B) of electrons from both core and valence levels of materials, was only pioneered almost half a century later, with the first high resolution spectrum recorded in in 1954, by Siegbahn et al.[85] Commercial instruments took another 15 years to be produced and made widely available. Siegbahn received a Nobel Prize for his work in 1981.

XPS continues to be a popular investigation method today due to the accessibility, low cost and ease of result analysis. XPS has traditionally been used on solid samples due to the ultra-high vacuum conditions that are usually required. In XPS, X-rays of a known energy (hv) are directed at the sample. An electron is excited, escapes the sample and has its kinetic energy (E_{kin}) measured by a detector (Figure 2.1). The binding energy, E_B, is calculated using Eq. 1;

$$hv = E_B + E_{kin} + \varphi \qquad \text{Eq. 2.1}$$

Where $h\nu$ is the photon energy, E_{kin} the kinetic energy and φ is the surface work function, defined as the energy required to remove an electron from the surface of a material into infinite space, or vacuum. When comparing across the same orbital, the higher the E_B, the lower the electron density of the species. φ is difficult to determine for liquids[86, 87] and some solids, hence only relative binding energies (ΔE_B), with respect to a chosen reference, are considered. This reference could be the E_B of any atom that is minimally interacting with its changing environment, usually adventitious carbon in insulating solids.

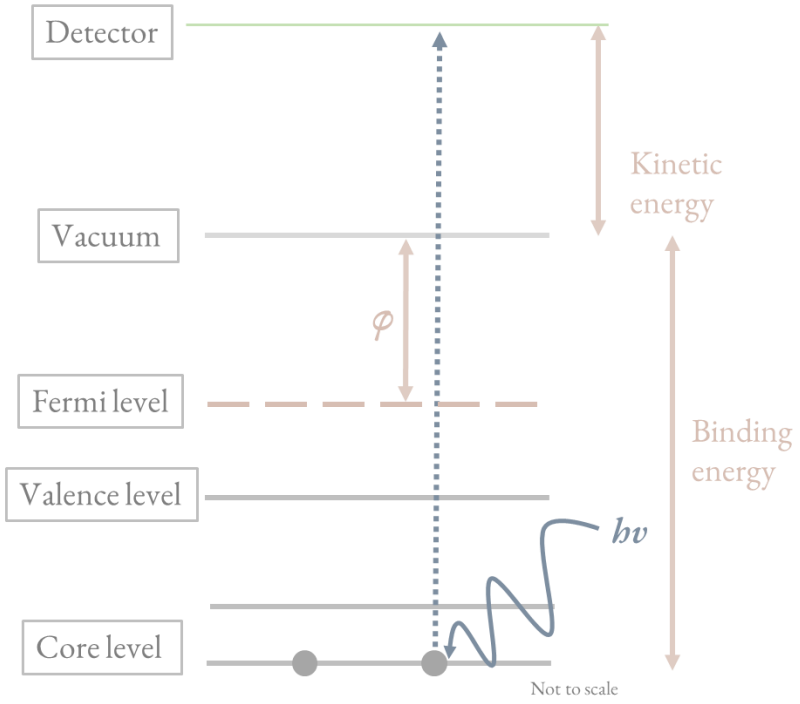

Figure 2.1 The process of X-ray photoelectron spectroscopy (XPS).

In core level XPS, the resultant E_B, peak area and intensity fluctuations in XPS spectra can reveal information not only relating to composition, but also the chemical state of the species. Measurements can help to understand the local geometric structures, oxidation states, bonding and band structures. These results are based on a significant assumption in XPS; that the E_B and peaks produce accurate and reliable information that can be interpreted and applied to the ground-state system, despite including some effects from the perturbed system.

$$E_B = E_{FS}(n-1) - E_{IS}(n) \quad \text{Eq. 2.2}$$

E_B is defined as the energy difference between the final state (the altered state once an X-ray has been applied and an electron removed, FS) and the initial state (or the ground state, IS), written in Eq. 2.2 where $E_{FS}(n - 1)$ is the FS energy and $E_{IS}(n)$ is the IS energy. Despite an array of research based on this assumption, no work has been published to conclusively demonstrate that the E_B obtained from XPS measurements of ionic liquids (ILs) are predominantly influenced by IS effects in the bulk phase. Attempts to assess influence of IS *versus* FS computationally has only been carried out on gas phase lone ion pairs.[88] IS effects include intramolecular bonding and intermolecular interactions. To continue reliably studying ILs using the XPS method, it is necessary to distinguish whether these ground state interactions are influencing the electronic behaviour represented in an XPS spectrum, or if 'final state-induced interactions' are dominating the peak characteristics.

Typically, XPS is a surface-sensitive technique. The further the X-rays penetrate the sample, the higher the probability of the exiting electrons undergoing inelastic scattering and contributing to the background of the spectrum, instead of the resolved peak. Increased depth of probing not only increases the chance of influencing the electron's kinetic energy, but also prevents some of these electrons from leaving the sample entirely. The average distance that an electron with a given E_{kin} can travel within the material can be described by the inelastic mean free path (λ). The general rule dictates that the higher the density of the material, the shorter the λ. Typically, probe depth is calculated as 3λ.[89]

Despite this limit to the probe depth, XPS can also be used as a bulk technique. There are two main approaches to increasing the probe depth; changing the angle of the sample to the detector or modifying $h\nu$. The probe depth usually varies by cos(θ), with θ as the detection angle. Increasing the sample-detector angle reduces the distance that the electron has to travel through to reach the surface of the material, reducing the chances of inelastic scattering of the escaping electrons. The total distance travelled (from atom to detector) remains the same. Increasing the $h\nu$ will increase the E_{kin} of the electrons, while decreasing $h\nu$ increases the cross-section and therefore ionisation probability.

The minimum path is at around 50 eV to 100 eV E_{kin}, the highest surface sensitivity.[90] This method of varying probe depth can only be employed when using a synchrotron source. For ILs, at E_{kin} between 800 eV to 1300 eV, probe depth at $\theta = 80$ is around 1-1.5nm, $\theta = 70^{\circ}$ between 2-3 nm and $\theta = 0^{\circ}$ is between 7-9 nm.[14] A simple check of measured stoichiometry at different depths and any intensity changes that occur can give an indication of any structure or composition change from bulk to surface. Throughout this thesis, the XPS results included have been confirmed as bulk measurements of the IL using this method.[91]

The general characteristics of an XPS spectrum consist of a peak plotted on axes of E_B versus intensity. In this thesis, elements characterised by XPS include C, N, S, O, F and Cl. A single peak is observed for a single state with s orbitals, while p, d, and f orbitals produce a doublet for a single state.

2.1.2. Instrumentation

XPS measurements are typically carried out under ultra-high vacuum (UHV) conditions (10^{-8} to 10^{-10} mbar), although in recent years, near-ambient pressure XPS (NAP-XPS) has also been developed, typically for catalytic systems. The primary reason for the requirement of UHV conditions is to conserve the E_{kin} of escaping electrons by preventing any interactions with gaseous particles on their journey to the detector. Liquids are typically unsuitable for study in UHV conditions due to their volatility, as the load on the pumping system becomes quickly unsustainable. ILs are a part of a small selection of liquids, which also includes metals and a few hydrocarbons, that exhibit a sufficiently low vapour pressure to be studied by standard XPS UHV apparatus.[92] The UHV conditions are also implemented to protect the sample from any interference that may alter its composition during measurement.

Traditionally, XPS experiments were carried out using laboratory X-ray sources (Figure 2.2). Standard laboratory sources for XPS only produce 'soft' X-rays, those with $h\nu < 5$ keV. X-rays in laboratory XPS are typically produced from Mg Kα or Al Kα sources with $h\nu = 1253.6$ eV and $h\nu =$

1486.6 eV respectively. The most common of these is the Al Kα source, with which the laboratory XPS included in this thesis was carried out.

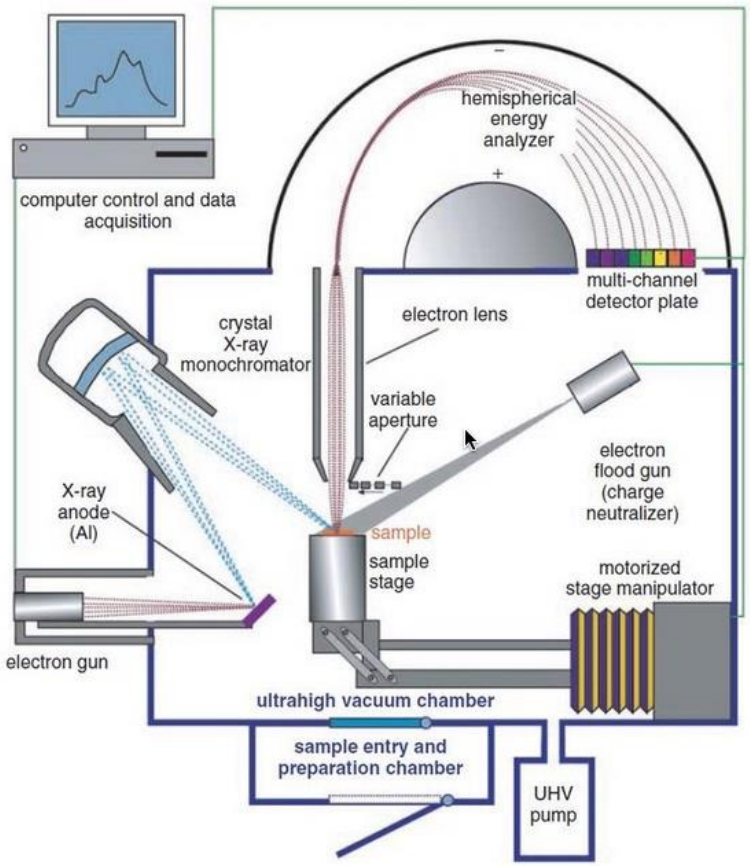

Figure 2.2 Scheme detailing the aspects of a laboratory XPS instrumental set up. Figure taken from literature.[89]

The main aspects of an XPS machine include the X-ray source, the monochromator and the electron detector or analyser. In a laboratory setup, electrons are aimed at the Al anode, causing the emission of X-rays together with electrons. This emission is passed through a quartz crystal monochromator and Al foil in order to minimise interference from weaker, "satellite" fluorescence lines, protect the sample from residual heat and increase the resolution of XPS spectra. This focused beam hits the sample, and photoelectrons are released and travel to the hemispherical analyser through the lens before reaching the detector. The lens dampens E_{kin} of the incoming electrons to match the chosen pass energy of the analyser. Once the electrons travel from the lens through the analyser, the number

of electrons at each energy are counted by the detector, and the information is transferred digitally to a computer.

The other most widely used type of X-ray source is synchrotron radiation. Synchrotron sources are created by electrons being accelerated by a series of magnets through a linear accelerator to a booster ring and into the storage ring, where they emit intense synchrotron light, from near infrared through to hard X-rays. Finally, the X-rays from the synchrotron light are directed through monochromators to beam lines, where the experiments are carried out (Figure 2.3). Synchrotron sources have the benefit of variable photon energy, high flux and high X-ray brightness. Though a flexible and high-quality source of X-rays, there are not many synchrotrons in the world, and therefore access for researchers is limited.

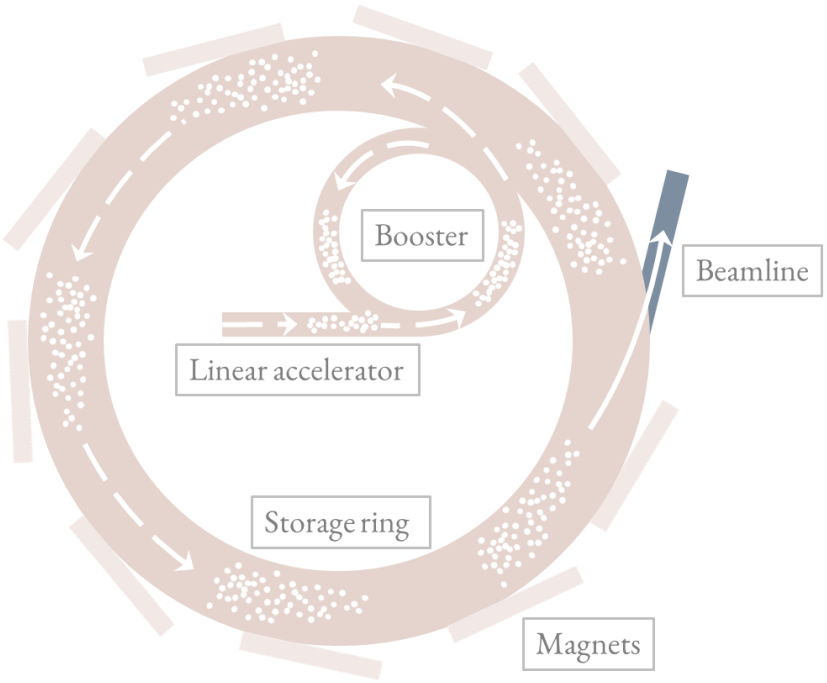

Figure 2.3 Schematic representation of the general synchrotron structure.

An inherent challenge in all XPS measurements is the phenomenon of sample charging. As electrons are released from the sample, a positive charge grows in the irradiated area. Sample charging moves the peaks to higher E_B and the non-uniform charge in the sample causes increased peak broadening.

The extent of the charging depends on the photon intensity (or flux) per sample area unit. Higher flux occurs in synchrotron sources (as the beam width is very focused, <500 μm) than in monochromated Al and Mg Kα sources. Smaller charging effects are experienced in standard Al or Mg Kα sources, and for ILs, the charging from these sources typically causes <0.5 eV E_B shifts. For conducting samples, charging can be compensated for by earth connection of the sample stage. For insulating or semiconducting samples, an electron gun may be used as a charge neutraliser to aim low energy electrons at the sample. This method can reduce the broadening caused from charging but may introduce negative E_B shifts. Another solution to sample charging is reducing the photon flux, but this approach requires increasing counts to compensate for the loss of spectral quality, thus increasing the risk of surface contamination from extended measurement times. Thus, especially in ILs, charge referencing is carried out during result analysis. E_B is referenced, most commonly, to C 1s of an alkyl carbon.[91] This reference is most widely used due to the presence of carbon in most ILs, either in the structure of one of the ions or as adventitious carbon, from contamination of the sample.

Another risk when irradiating a sample is beam damage. Beam damage is the decomposition of the sample caused or initiated by the X-ray radiation, resulting in bond breaking. Beam damage can be distinguished visually, as the sample may darken, or through the recorded spectra, where new states appear, such as in the C 1s region. In liquids, the decomposition products are able to diffuse away from the site of analysis and typically these effects on the spectrum are not observed in our work. It is considered that ILs may be safe from beam damage for 4 hours under a non-monochromated source.[93] However, these times would be significantly shorter for monochromated and synchrotron sources. Overall, it is not possible to estimate the rate of beam damage before an experiment, and experimental parameters need to be tested before production spectra are recorded.

A relatively novel XPS design that overcomes these challenges is liquid jet XPS. It varies from the traditional setup by replacing the sample on a substrate with a continuous jet of the liquid sample. This specialist apparatus avoids charging and beam damage, as the sample being investigated is continuously renewed. This method has its own limitations; the quantity of vapour, even in liquids with low volatility, can increase quickly and the required volume of sample can be expensive.

Finally, in any XPS setup, various processing chambers may be added for any pre-measurement sample processing. For the work presented in Chapter 6, sample preparation was carried out prior to analysis. For the deposition of $[C_4C_1Im][SCN]$ onto the rutile surface, a custom evaporation chamber was built by Dr Roger A. Bennett.

2.1.3. Measurements

Appropriate preparation of the instrumentation and the sample is required to minimise the existing and potential contamination with impurities. The main impurities found in ILs are water, halides, silicon grease and excess organics. Water is absorbed by ILs over time during storage while halides and organics most likely remain from the synthetic process. The XPS instrumentation may have gas remaining on the chamber walls, following a previous experiment, for example. Baking, degassing and sputtering are the processes employed to counteract the contamination. Baking involves heating the chamber to ~150 °C from many hours to several days, which allows the system to reach and maintain UHV conditions. Sputtering is the process of targeting the surface with Ar^+ ions to remove contaminants from the surface of the sample, under the conditions 500 eV, 5 μA for 10 mins.

Recording an XPS spectrum successfully requires a balance of a variety of settings. These include $h\nu$, resolution, counts, pass energy and sample-analyser angle. For a successful spectrum, the peaks should be well-defined with a high signal to noise ratio (S/N). The source of noise is from electrons that have undergone inelastic scattering, and these create the background. $h\nu$ from a laboratory Al Kα source is 1486.6 eV, although when measuring at a synchrotron, photon energy may be chosen according to the core levels being measured and is dependent on the photoionisation cross-section of the orbital. The photoionisation cross-section (σ_{ij}) is a measure of probability of an electron being ionised from orbital j of element i at a given $h\nu$.

Resolution is determined by measuring the full width half maxima (FWHM) of a peak. The higher the resolution, the more likely the peak may be resolved during analysis. Resolution, or the extent of broadening of an XPS peak, has two sources: sample and instrument. Instrumental broadening is caused by the energy range of the radiation source or the experimental settings such as pass energy.

The majority of broadening from the sample is determined by disorder of the sample, but it can also source from charging and core hole lifetime, which is the time taken to fill the core hole once an electron has been ejected. Generally, the closer the core level is to the nucleus, the faster it is likely to be filled and the higher the broadening. Lifetimes of C 1s, N 1s, S 2p and O 1s have been measured as 0.104 eV, 0.115 eV, 0.054 eV and 0.170 eV.[94-96]

The pass energy of the analyser is set according to which E_{kin} should be allowed to pass through to the detector. Modern analysers are set to constant pass energy mode. The analysing system consists of a collection lens, the energy analyser, and the detector. The collection lens limits E_{kin} of the electrons that can pass through to the analyser. The pass energy is the centre potential of the analyser. For example, if the lens is set to 100 eV, and the pass energy is 50 eV, an electron with E_{kin} of 150 eV will be able to pass through to the detector. The lens reduces the E_{kin} by 100 eV, leaving the electron with 50 eV E_{kin} to successfully pass through the centre of the analyser without hitting the hemispheres. A higher pass energy reduces the resolution of the instrument and increases counts, hence a pass energy of 5 to 25 eV is usually applied for high resolution scans, for measuring E_B, intensities and FWHM, and 50 to 200 eV for survey scans, where the aim is to determine the sample composition.

The general process of gathering data from a sample via XPS begins by measurement of a survey spectrum, for both known and unknown samples. This spectrum is measured for a wide energy range at low resolution to include regions of all the core regions that could be present. For unknown samples, the purpose is to learn the elements in the composition and for known samples, to check for any present impurities. Following this check, a smaller region is measured with high-resolution in order to analyse specific features.

2.1.4. Analysis

2.1.4.1. Charge referencing

Mentioned briefly in Section 2.1.1., charge referencing in XPS analysis is necessary as the work function φ, required for the determination of absolute E_B, is difficult to measure.[86] Any reference may be chosen, as long as the reference is kept constant between any different spectra being compared during analysis. In ILs, the peak most commonly selected for charge referencing is the C_{alkyl} 1s, to a value of 285 eV. C_{alkyl} 1s is chosen due to its presence in most ILs, either by composition or contamination. If no C_{alkyl} is present, N_{anion} 1s may be chosen as a reference.[91] The value of C_{alkyl} 1s at 285 eV has been found to be a reference to the Fermi level of long alkyl chains – typically 8 membered and above. Recently, researchers have refined referencing methods. Research developments have determined a new charge referencing value, referenced to vacuum level, of 289.58 eV for adventitious carbon atoms on a metal surface.[97-101] The first application of this referencing value to ILs was carried out by our research group.[91] This referencing choice was used for the length of this work, and all of the experimental XPS data was referenced to the value of C_{alkyl} 1s at 289.58 eV. Calculated data was also referenced to this value when comparing the experimental and calculated survey spectra.

It is worth noting that there is always likely to be an error in measurements, despite charge referencing for a range of reasons, such as charging, fluctuations in the equipment, etc. This error is estimated at ≤0.1 eV for the experimental data presented in this thesis. This error is a conservative estimate, mostly corresponding to comparison of spectra measured over multiple experiments.

2.1.4.2. Peak fitting model

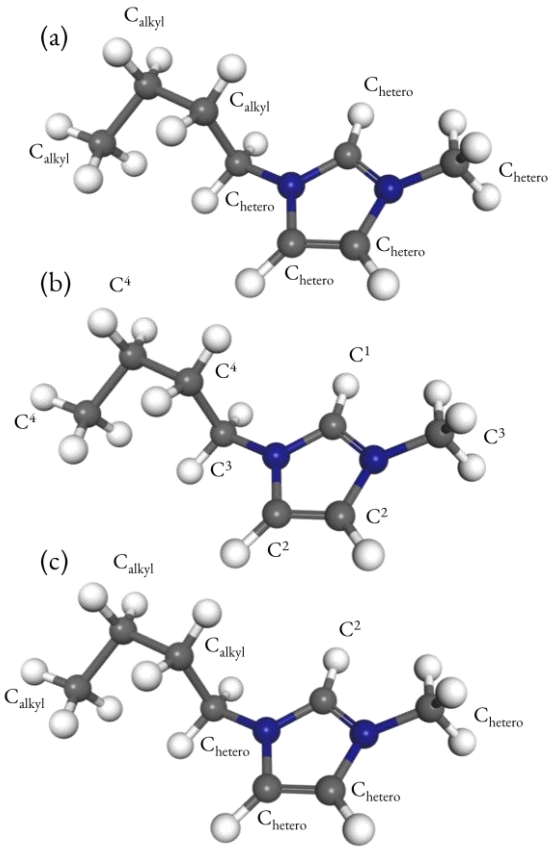

Figure 2.4 The cation $[C_4C_1Im]^+$, labelled according to three different C 1s high resolution XPS peak fitting approaches. In this work, atoms of $[C_nC_1Im]^+$ cation are labelled according to **(c)**.

Peak fitting can be quite complex, particularly for materials such as ILs. As they are liquid, and typically consist of asymmetric ions, they have a relatively wide range of atoms and environments, compared to materials traditionally studied by XPS – solids, typically metal oxides. Some XPS spectra are clear, and the peaks are easily assigned, such as the N 1s core level. In ILs, when both the cation and the anion contain a nitrogen atom, the peaks are often well-defined and separated. However, one of the most important core levels studied in ILs is the C 1s. In imidazolium-based ILs, studied in this thesis, this spectrum is difficult to resolve. The C 1s peaks in these ILs are close enough

to overlap, yet different enough to suggest separate environments, particularly with higher resolution instrumentation.

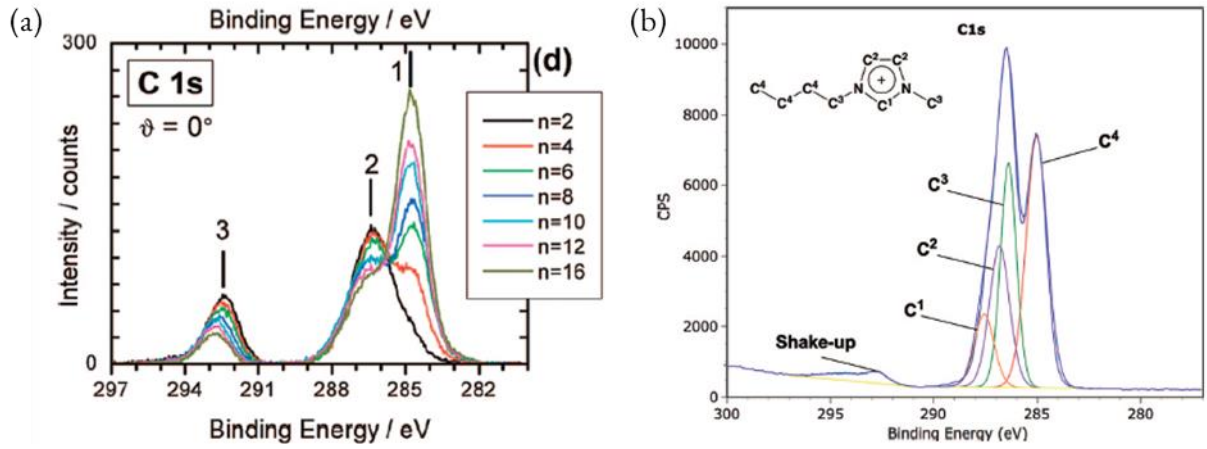

Figure 2.5 (a) C 1s XP spectra of $[C_nC_1Im][NTf_2]$ where n = 2 to16. Peaks labelled 1 and 2 are the cation peaks, C_{alkyl} and C_{hetero} respectively. Figure taken from literature.[102] **(b)** C 1s XP spectrum of $[C_4C_1Im][BF_4]$ with peak fittings, labelled according to Figure 2.4b. Figure taken from literature.[103]

The ambiguity of the C_{cation} 1s peaks has led to a range of fitting interpretations, each grouping the carbons differently and fitting the experimental peaks with 2, 3 or 4 components. The labelling of the cation in each of these methods is presented in Figure 2.4. Non-monochromated sources produce low resolution, and so usually only 2 overlapping peaks can be distinguished. In one fitting method, these have been fitted with a peak for each, C_{alkyl} at the lower E_B peak and C_{hetero} at the higher E_B peak (Figures 2.4a, 2.5a). Here, C_{hetero} classifies any carbon attached to a hetero atom, in this case nitrogen. A second fitting model for C 1s fits these with 4 separate peaks: C^1, C^2, C^3, C^4 (Figures 2.4b, 2.5b). This distinguishes all the different carbon environments in the cation: alkyl chain, carbon bonded to 2 nitrogens, ring carbon bonded to 1 nitrogen and alkyl carbon bonded to 1 nitrogen. The fitting model that is used in this thesis fits 3 peaks to this spectrum, defined as C^2, C_{hetero} and C_{alkyl}, (Figure 2.4c, 2.6). In the IL 1-butyl-3-methyl-imidazolium thiocyanate $[C_4C_1Im][SCN]$, these peak areas are constrained to a ratio of 1:5:3 for each carbon environment,

respectively. Table 2.1 contains the peak area constraint ratios for all of the ILs for which experimental data is included in this thesis.

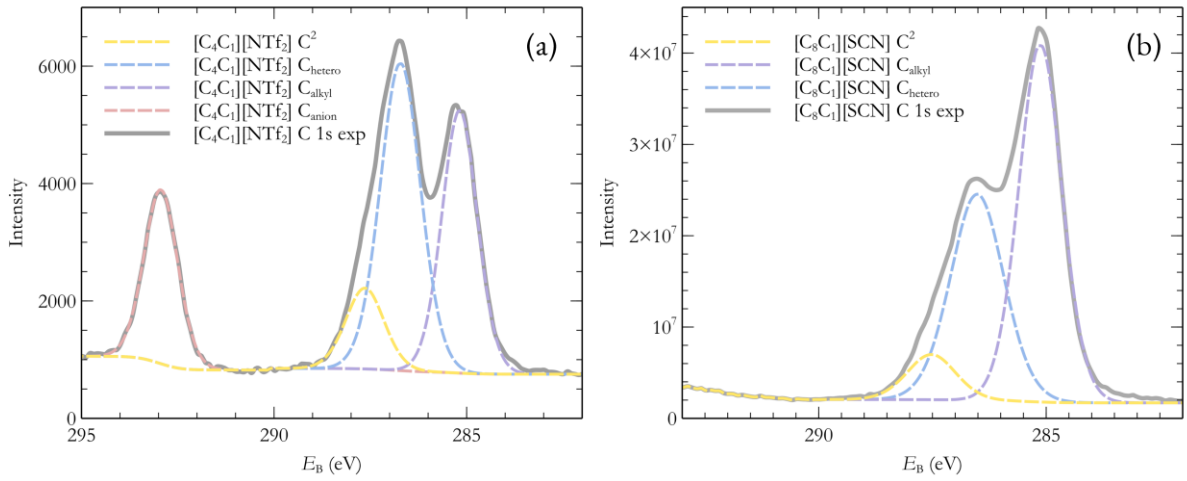

Figure 2.6 XPS peaks fitting of the C 1s high-resolution spectra of $[C_4C_1Im][NTf_2]$ **(a)** and $[C_8C_1Im][SCN]$ **(b)**, as approached in this work.

While 1-butyl-3-methylimidazolium bis(trifluoromethylsulfonyl)imide, $[C_4C_1Im][NTf_2]$ has a distinct and separate C_{anion} peak, there is no resolved C_{anion} peak in the spectra of the ILs containing an $[SCN]^-$ anion. Despite $[C_4C_1Im][SCN]$ only having 4 C_{hetero} atoms in the cation, the anion does not produce a distinct peak and the assumption is made that the anion peak is incorporated within the main C 1s peaks, and this is accounted for as an additional C_{hetero} environment (see Table 2.1).

Table 2.1 Tabulated XPS fitting parameters for C_{cation} 1s core level, for each IL investigated in the present work.

Ionic Liquid	Peak area constraint ratio C^2:C_{hetero}:C_{alkyl}
$[C_4C_1Im][SCN]$	1:5:3
$[C_8C_1Im][SCN]$	1:5:7
$[C_4C_1Im][NTf_2]$	1:4:3
$[C_8C_1Im][NTf_2]$	1:4:7
$[C_8C_1Im][Cl]$	1:4:7

All XPS data was fitted using CASAXPS software. A Shirley background was employed:

$$S_S(E) = k \cdot \int_E^{+\infty} P(E')\, dE' \qquad \text{Eq. 2.3}$$

where $S_S(E)$ is the Shirley background intensity, $P(E')$ is the peak as a function of the electron energy E and k is an arbitrary constant. The GL(30) line shape was used for all fittings:

$$\mathrm{GLP}\,(x; F, E, m) = \exp\left[-4\ln 2\,(1-m)\frac{(x-E)^2}{F^2}\right] \Big/ \left[1 + 4m\,\frac{(x-E)^2}{F^2}\right] \qquad \text{Eq. 2.4}$$

Where F is the function width, E the core level energy and mixing parameter, m, was set to 0.3 to produce a a 70% Gaussian and 30% Lorentzian mix, as in experimental peak fitting. Values 0 and 1 are pure Gaussian and pure Lorentzian respectively.

2.2. Normal Incidence X-ray Standing Wavefields

The normal incidence X-ray standing wavefield (NIXSW) method is based on the interference caused by incoming and diffracted X-ray beams of the same incidence to produce a standing wavefield (Figure 2.7). The interaction of this standing wavefield with the atomic core levels enables investigation of the spacings between the surface and the adsorbate. NIXSW produces a periodic probability map of the investigated layers above the surface.

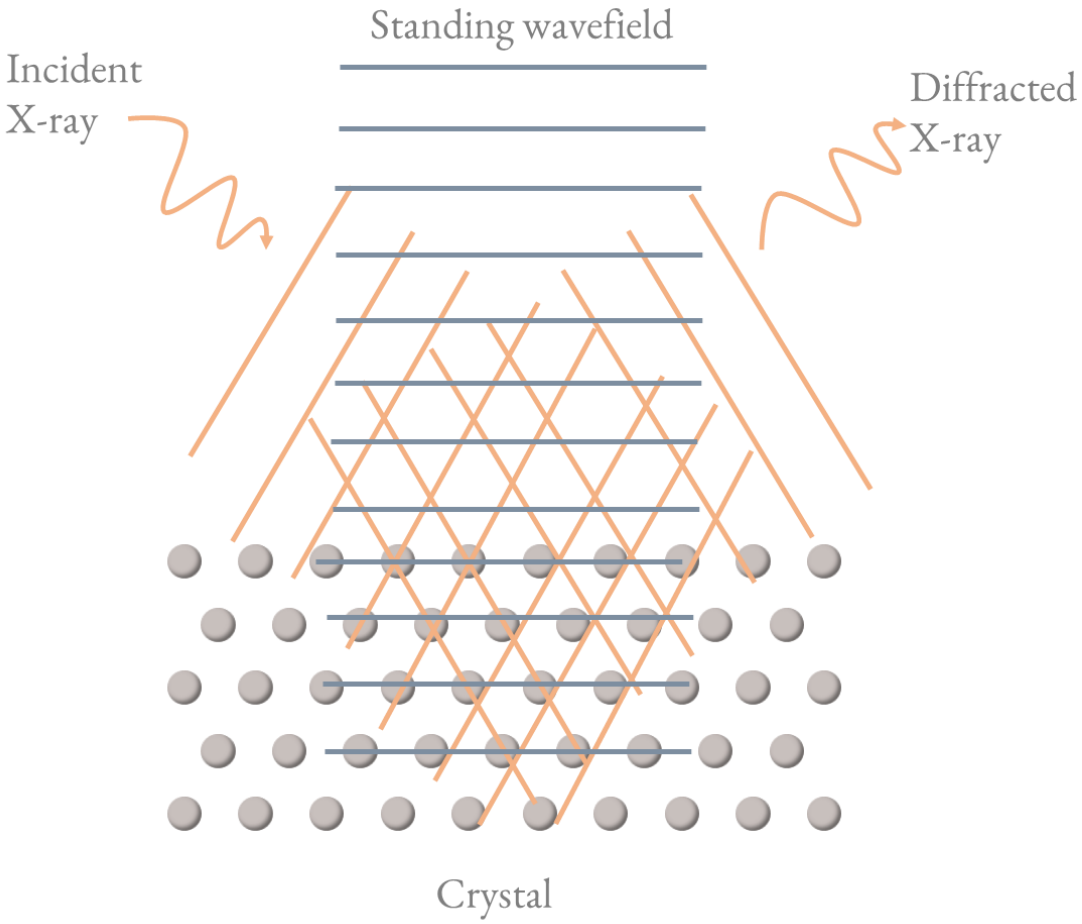

Figure 2.7 Scheme depicting the basis of NIXSW. Formation of X-ray standing wavefield in and above a crystal by the interference of incident and reflected X-rays is depicted. Figure adapted from literature.[104] Figure is not to scale.

The results from this method, which was used to study an IL-titanium dioxide (TiO_2) interface, are reported in Chapter 6 of this thesis. Probability map cross-sections were extracted from the data (Figure 2.8) to determine the adsorption positions of the anions of the IL $[C_4C_1Im][SCN]$ and to make predictions of adsorbed geometries. These experiments were carried out on a collaborative beamtime, with Dr. Roger Bennett (RAB), Dr Jake Seymour (JMS), Dr Kevin R. J. Lovelock (KRJL) and Dr David Duncan (DD). RAB analysed the results, using an analysis script from DD, and created the figures with NIXSW results in Section 6.5.1.

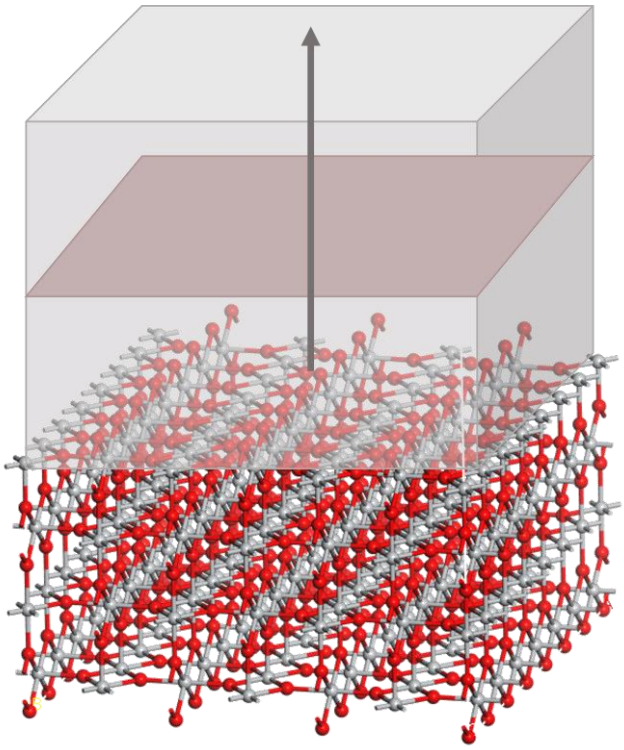

Figure 2.8 Visual representation of the probed area above the surface, in grey, using NIXSW. Two-dimensional cross sections of the probed area (beige) were extracted to determine adsorbate positioning above the surface. The solid surface represented here is TiO_2.

2.3. Limitations

The experimental X-ray based methods described above present some challenges when studying a system. One of these is the length of time that it can take to successfully collect high quality data. If specialised conditions or applications are being studied, between sample preparation and measurements, it can take several days, even a week, to collect data for a single IL with NIXSW or half a day with XPS. A great example of this is the experimental work presented in this thesis on TiO_2, in Chapter 6. Particularly when carrying out experiments at synchrotrons, applications must be made at least 6 months in advance of the awarded beamtime. Meticulous planning is required for every beamtime; approach, which samples will be measured in order of priority and plans for best- and worst-case scenarios have to be made. When working with a new IL or an additional aspect such as a surface, the experiment is dictated by the unknown. The experiment could go very well, and an array of publishable results could be collected within a week, or the sample may prove itself to be particularly difficult and the whole week of beamtime is spent learning the sample's behaviours, such as beam damage, charging, *etc*. This knowledge can only be applied to achieve publishable data after another application and beamtime award cycle.

Finally, only limited information can be gleaned from the results, guesswork or assumptions have to be made. This is where a computational approach can maximise the result output of experiments.

2.4. Facilities

The laboratory XPS data presented in this work is from experiments that have been carried out at UCL and Imperial XPS facilities. The synchrotron XPS data presented has been collected from BESSY II synchrotron at the UG-49 beam line with the SOL^{3}PES end-station and Diamond Light Source at the I09 beam line. The NIXSW experiments were carried out at Diamond at the I09 beam line.

3. Computational methods

3.1. Introduction

Computational simulation may be considered as the third branch of scientific investigation, after experiment and theory. Modelling and simulation have a long history of contributions to chemistry. Visualisation of atoms began in two dimensions, on paper, by Dalton as far back as 1808 (Figure 3.1).[105] Progress was slow to begin with, as 3D representations only appeared around 1952, with Newman projections.[106] The development of the first computers with sufficient power for theoretical calculations occurred during the 1950s, and one of the first virtual atomistic models was produced in 1966 by Karplus et al. (Figure 3.2).[107]

While the first science Nobel prizes were awarded in 1901 in chemistry and physics, it took another 65 years for the recognition of computational work with a Nobel. The first Nobel prize in Theoretical Chemistry was awarded jointly to Kohn and Pople in 1998 for the "development of the Density Functional Theory" and "development of computational methods in Chemistry", respectively. Almost 50 years after the first animations, Karplus, Levitt and Washel were awarded a joint Nobel prize for the development of multi-scale models for complex chemical systems in 2013.

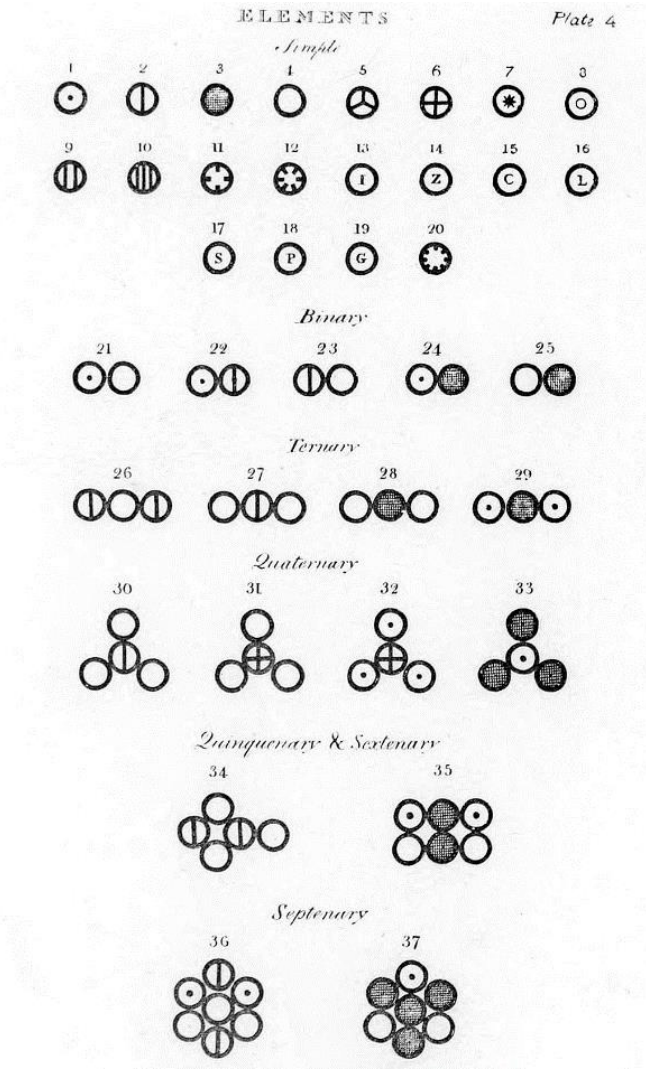

Figure 3.1 An excerpt from A New System of Chemical Philosophy by John Dalton[105], an example of some of the first atomic visual representations.

With these developments and their applications, physicists, chemists and biologists have been granted the ability to observe atomic dynamics - translations, vibrations and rotations - on the sub-nanoscale. It became possible to simulate and visualise the transition states, atomic and electronic movements. The success of computational methods in chemical research is demonstrated by the exponential rise in research publications with the search terms *"computational"* and *"chemistry"* on Web of Science (Figure 3.3).

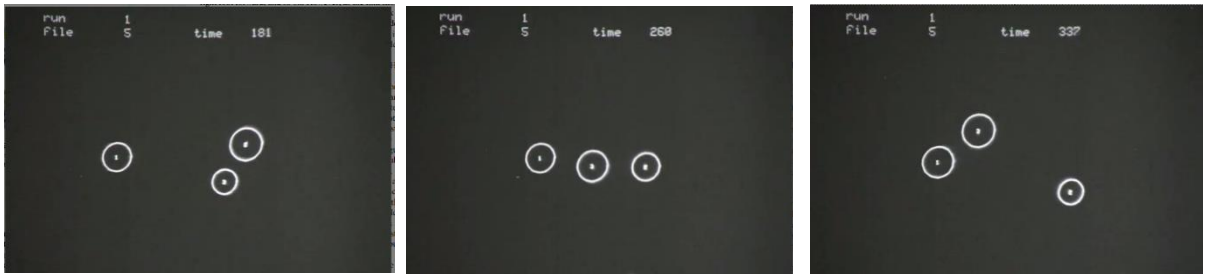

Figure 3.2 Stills from the first animation of a simple three-atom reactive collision by Karplus et al.[107]

Typically combined with experimental results for benchmarking or validation, computational chemistry is used to clarify mechanisms and pathways of reactions and interactions. As an example, the correct interpretation of XPS spectra is not always clear – in the case of atomic oxygen on an aluminium (111) surface, the deconvolution of the experimentally measured XPS peaks was not supported by theoretical calculations. The calculated results guided the re-evaluation of the analysis and a new interpretation was developed, satisfying both experiment and calculation.[108]

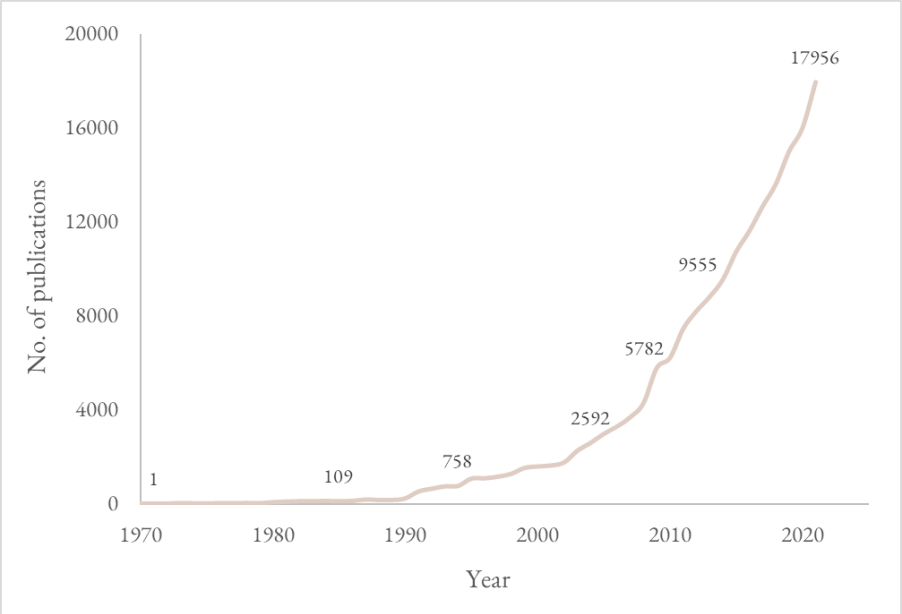

Figure 3.3 Graphical representation of the exponential rise in computational chemistry research publications from 1970 to 2020. Data from a search of the terms "computational" and "chemistry" on Web of Science.

Computational research methods can be broadly divided into classical and *ab initio* methods, all aiming to calculate the energy of a set of atoms in a given configuration. Classical (or empirical) methods use approximate potentials to describe the interactions between the atoms, called force fields (FF). These potentials have parameters that are often fitted to reproduce experimental data, and can be used, for example, in classical Molecular Dynamics. *Ab initio* – literally '*from the beginning*' - methods are based on quantum mechanics and only require physical constants as inputs. These methods are more sophisticated, allowing predictions of properties, interpretation of experiments, testing and validation of less accurate methods and benchmarking for classical methods without the need for experimental data.[109-113]

3.2. Classical Molecular Dynamics

Classical methods do not explicitly describe electrons, but rather represent atoms as spheres connected by springs. Potentials are used to describe the dynamics and interactions of a system, called force fields (FF). The terms in a FF include internal bond dynamics, consisting of stretching, bending and torsion, and terms for the intermolecular interactions, such as van der Waals and electrostatic behaviours. For liquids, the Lennard-Jones type potentials are convenient.[114] This approach is relatively economical in computational power and therefore the system sizes that can be computed are orders of magnitude larger than those that can be computed using *ab initio* methods. Despite this, it is considered that due to the static nature of non-covalent interactions with this method, this approach overlooks a range of important many-body effects. In ILs, these include partial charge transfer, hydrogen bonding and polarisation. Another known limitation of FFs is their tendency to be accurate only in modelling the specific system for which they are developed and under certain conditions. Developing FFs is a challenging and time-consuming task, as they require parameterisation against experimental or *ab initio* data, which might not be available for the material of interest. Therefore, the applicability of the FF may be significantly limited.

The complex network of interactions in ILs proves difficult to model using universal FFs, and so many FFs have been developed and refined for ILs. These include all-atom FFs[115-118], united-atom

FFs[119-121] and virtual site FFs.[122]. Polarisable FFs have also been applied with the aim of improving the representation of many-body effects in ILs.[38, 110, 123-129] These FFs enable simulation of electron movement within the ion in response to the external environment, however, they do not allow for polarisation or charge sharing between ions. These effects have been compensated for by the reduction of the formal charges of each ion (typically between ±0.7 and ±0.9).[33, 39, 123, 130-133] This approach can also face transferability issues between different ILs.

In classical molecular dynamics (MD) simulations, the trajectories of the atoms are calculated using Newton's second law of motion. The FF, a function of the atomic coordinates, is used to calculate the potential energy, and from its gradient, the instantaneous force acting on each atom can be obtained. The equations of motion are discretised with respect to time, so that the positions, velocities, and forces are recalculated at time points separated by a timestep. The timestep should be short enough for the forces acting on the atoms to be almost constant during that time, but not too short, to avoid the simulation from proceeding too slowly.

Depending on the properties being investigated, MD simulations may be carried out in the microcanonical, canonical or the isothermal-isobaric ensembles. The microcanonical ensemble keeps the number of particles (N), total volume (V) and total energy (E) constant and is abbreviated to NVE. The canonical ensemble replaces the constant energy with a constant temperature (T), and is therefore known as NVT, whereas the isothermal-isobaric ensemble additionally replaces the constant volume with a constant pressure (P) respectively and is abbreviated to NPT.

Classical MD may be the method of choice for ILs when the study is based on geometric structure or transport properties, for example. However, it has been shown that minor adjustments to any aspect of the classical MD simulation can considerably affect the simulated structural and dynamic properties.[37]

Classical MD was only applied in this work for pre-equilibration runs, using the Dreiding FF, before the *ab initio* molecular dynamics production runs. Dreiding is a generic FF which works well for organic and main group inorganic molecules.[134] By pre-equilibrating with a FF, the *ab initio* molecular dynamics starts from a more reasonable distribution of coordinates and velocities, and equilibrates more rapidly, saving computing time.

3.3. Ab initio methods

Ab initio methods are the gold standard for computational accuracy, as they are based on quantum mechanics and treat electrons explicitly. Accessing the electronic structure computationally is particularly useful for combining simulations with experimental techniques that probe electronic structure, like XPS. In ILs, charge re-distribution between ions is an important phenomenon, whose investigation requires the explicit treatment of electrons.

In quantum mechanics, the *Born-Oppenheimer approximation* is applied, which leads to a separate treatment of electron and nuclear motion.[135] This is a reasonable approximation, as the nuclei have a much larger mass and move much more slowly than the electrons. Thus, it is possible to calculate the lowest energy state of the electrons for a given system of nuclei in fixed positions. *Ab initio* computational methods are based on the Schrödinger equation, published by Erwin Schrödinger in 1926. Most *ab initio* methods try to solve the time-independent, nonrelativistic Schrödinger equation:

$$\hat{\mathrm{H}}\psi = E\psi \qquad \text{Eq. 3.1}$$

The Schrödinger equation determines the wavefunction ψ, which allows the prediction of all properties in a quantum mechanical system, and the energy states E of the system, from the Hamiltonian Ĥ. It can be solved exactly only for simple systems, such as a single-electron system. The Hamiltonian for systems of interacting electrons and nuclei, in the Born-Oppenheimer approximation[135], can be written as:

$$\hat{\mathrm{H}} = -\frac{\hbar^2}{2m}\sum_{i=1}^{N}\nabla_i^2 + \sum_{i=1}^{N}V(\boldsymbol{r}_i) + \sum_{i=1}^{N}\sum_{j<i}U(\boldsymbol{r}_i,\boldsymbol{r}_j) \qquad \text{Eq. 3.2}$$

where $\hbar$ is the reduced Planck's constant, m is mass of the electron, N the total number of electrons in the system, $V(\boldsymbol{r})$ is the total electrostatic potential that an electron at position $\boldsymbol{r}$ experiences by interacting with all the nuclei in the system, and $U(\boldsymbol{r}_i,\boldsymbol{r}_j)\sim 1/|\boldsymbol{r}_i-\boldsymbol{r}_j|$ is electrostatic repulsion

between electrons i and j. The first term defines the kinetic energy of the electrons, the second is the interaction between an electron and the nuclei and the third term is the interaction between different electrons.

The wavefunction is a function of each coordinate of every electron in the system, *i.e.* $3N$ variables (or $4N$ if we include spin, see more in Section 3.5.1). For systems with more than one electron, the solution to the Schrödinger equation becomes impossible to calculate analytically. In order to solve the equation numerically, it is common to express the multielectron wavefunction in terms of one-electron wavefunctions, for example via a Slater determinant in Hartree-Fock theory, and then obtain a one-electron Schrödinger equation. The solution of any of these requires knowledge of all of the other individual electron wavefunctions simultaneously. This makes solving the Schrödinger equation an iterative process, where one needs to start with a certain approximation for the one-electron wavefunctions, and then use the calculated wavefunctions to solve the equation again, and repeat until self-consistency is obtained.

Beyond the numerical difficulties in calculating a wavefunction, a more fundamental problem of this quantity is that it cannot be directly measured – in theory, only the positional probability of N electrons may be observed. The closely related electron density at a particular position, $n(\mathbf{r})$, can be used instead of the wavefunction to characterise the electronic structure. The electron density may be expressed in terms of the individual electron wavefunctions as:

$$n(\mathbf{r}) = 2 \sum_i \psi_i^*(\mathbf{r})\psi_i(\mathbf{r}) \qquad \text{Eq. 3.4}$$

3.4. Density Functional Theory

Density functional theory (DFT) is a method that is based on the Hohenberg and Kohn (HK) theorems and Kohn and Sham's derivations, in an attempt to solve the Schrödinger equation as accurately as possible. Theorem I by Hohenberg and Kohn[136] states that:

The full many-particle ground state is a unique functional of the electron density.

Theorem II states that:

The electron density that minimizes the energy of the overall functional is the true electron density corresponding to the full solution of the Schrödinger equation.

Theorem I leads to the logical conclusion that the electron density contains all the information about the system, including the wavefunction Ψ. However, the electron density is a function of only three coordinates (plus spin), rather than $3N$ (or $4N$) coordinates as in the full wavefunction solution to the Schrödinger equation.

Theorem II states that the "true" functional from theorem I, once known, would allow the determination of the ground state energy and density through variation of the density to minimise this functional. Hence, the main challenge is to determine this true functional.

Kohn and Sham (KS) developed a further approach to apply properties of a homogenous gas to inhomogenous systems in theoretical calculations.[137] The KS energy functional is expressed by:

$$E[n(\mathbf{r})] = T_e[n(\mathbf{r})] + V_{ne}[n(\mathbf{r})] + V_{ee}[n(\mathbf{r})] + E_{XC}[n(\mathbf{r})] \qquad \text{Eq. 3.5}$$

The first three terms, in order, include kinetic energy of electrons, nuclear-electron potential and electron-electron potential. The first three terms contain ~99% of the total energy. The other ~1% is attributed to the exchange-correlation functional, E_{XC}. The kinetic energy term T_e is expressed as a non-interacting system of electrons with the same density as the interacting system of electrons. The

density that minimises that energy is defined by one-electron KS wavefunctions, which satisfy the single electron equation:

$$\left[-\frac{\hbar^2}{2m}\nabla^2 + V(\mathbf{r}) + V_H(\mathbf{r}) + V_{XC}\right]\psi_i(\mathbf{r}) = \varepsilon_i\psi_i(\mathbf{r}) \qquad \text{Eq. 3.5}$$

The terms, in order, include the kinetic energy of electrons, the potential of an electron and the nuclei, the Hartree potential and an exchange-correlation term. The Hartree potential describes the electron as interacting with the average of entire electron 'cloud' which also includes the electron being considered. This produces a self-interaction error, as an electron cannot interact with itself.

3.4.1. Exchange-correlation functionals

The exchange-correlation functional contains non-classical electronic effects. Spin of an electron is a principle that only exists in the quantum chemical approach. In classical mechanics, electrons are only capable of repelling one another. In quantum chemistry, electrons have an additional quality, spin, which allows electrons with opposite spins to also attract one another. This phenomenon is termed the "exchange" interaction.

Correlation is a term defined by way of the Hartree Fock (HF) theory, which has been mentioned above. In HF, the multielectron wavefunction is written as a simple combination (the Slater determinant) of one-electron orbitals. The "correlation" interaction is defined as the difference between the true ground state energy and the energy calculated by HF using a complete basis set.

The exact exchange-correlation functional in KS theory is unknown, but a range of approximations have been developed. One class of these functionals uses the generalised gradient approximation (GGA). It uses information from the local electron density and the local gradient of the electron density. One of the most widely used, also used in most of this thesis, is the Perdew-Burke-Ernzerhof (PBE) functional.[138] A small number of calculations were carried out using the hybrid Becke, 3-parameter, Lee-Yang-Parr (B3LYP) functional.[139, 140] Hybrid functionals use a fraction of the exact exchange from HF, and the remaining exchange-correlation contribution from DFT.

3.5. Ab initio MD

There are two main types of *ab initio* molecular dynamics (AIMD) approaches: Car-Parrinello (CPMD) and Born-Oppenheimer (BOMD). In CPMD, the electron density is only calculated at the beginning of the simulation and subsequently propagated with atomic positions. In BOMD, the KS equations (Section 3.4) are solved to calculate the electronic structure at each timestep. The energy is calculated based on the atomic positions. As a function of the atomic positions, the energy can then act as the interatomic potential to calculate the forces on the atoms and the coordinates are updated. This process is computationally intensive and therefore models have to be quite limited in size, for ILs this is anywhere from a single pair to 64 pairs, depending on the size of the ions making up the IL and the calculation type chosen.[141] Only BOMD was employed in this thesis, and this is the method referred to as AIMD in the following results.

3.6. Electronic calculations

Solving the KS equations (Section 3.4) requires an iterative method, and this is called the self-consistent field method (SCF). An initial electron density is guessed, and the KS equations are solved to find the single-particle wavefunctions. The new electron density is calculated using the single particle wavefunctions. The two electron densities are compared, and if they are the same, or within a determined convergence limit, then the electron density can be considered the ground-state density, or converged. If these criteria are not fulfilled, then the initial electron density requires updating. Electronic calculations include single point energy calculations or geometry optimisations. Both types of calculation employ the SCF method. In single-point energy calculations, the atoms are not moved. Geometry optimisations are carried out at a temperature of 0 K, and the atoms are moved until convergence is reached, i.e. a geometry where the interatomic force is close to zero and the energy of the system is at a flat portion of the potential energy surface.

In this work, geometry optimisations were carried out with the CP2K code[142] using the Broyden–Fletcher–Goldfarb–Shanno (BFGS) optimiser[143] and single point calculations to obtain core levels were carried out using VASP.[144-147]

3.7. Pseudopotentials

A pseudopotential is an approximation applied to describe the core of an atom and its relation to the valence electrons. The valence electrons of an atom take part in chemical bonding and are responsible for chemical and physical behaviours and properties, while the core electrons do not take part in bonding and are tightly bound to the nucleus. Thus, pseudopotentials split the description of atoms into a core potential, including frozen core electrons and the nucleus, and valence electrons, explicitly treated. This approach reduces the number of planewaves required, requiring less computational power, although it could be considered not to be truly *ab initio*. In this thesis, the Goedecker, Teter and Hutter (GTH) norm-conserving pseudopotentials[148] are employed in the CP2K code. Another type of commonly used pseudopotentials are those from the projector augmented wave (PAW) method.[146, 149] These match the pseudopotential to the all-electron wavefunction behaviour, so the core electrons are treated explicitly, albeit kept frozen. This method is implemented and used in this thesis with the VASP code.

3.8. Dispersion corrections

Dispersion forces, or van der Waals forces, are long-range electronic interactions related to non-local correlation terms. Because of the non-locality, these interactions are not described well by the local GGA functional. In liquids, these long-range forces are cumulative and become significant. The neglect of these forces by standard GGA functionals has been overcome by development of empirical corrections to the functional which provide an excellent representation of these forces. Grimme corrections are one of the most commonly employed correction schemes, namely Grimme-

D2[150] and Grimme-D3.[151] In this work, the bulk IL and the IL-TiO_2 simulations employed the DFT-D2 and the DFT-D3 methods respectively.

3.9. Basis sets

To solve KS equations, we need a basis set to expand the KS wavefunctions. Basis sets are formed of a collection of basis functions, used to describe the electron density around a nucleus. Generally, basis sets are chosen differently depending on which type of system the DFT method is being used for. The two main types of system studied using DFT are molecular (finite) and extended (periodic) systems. In molecular systems, a linear collection of localised all-electron basis functions, or atomic orbitals, are typically used. In periodic systems, linear collections of plane wave basis functions are usually employed due to their simplicity in describing the single particle wavefunction.

In molecular systems, the two most common atomic orbital types are Slater-type orbitals (STOs) and Gaussian-type orbitals (GTOs). STOs represent hydrogen-like atoms and exhibit exponential electron decay away from the nucleus. These describe electrons close to the nucleus well, but do not represent many-electron interactions as accurately. GTOs are far more commonly used, as it is much cheaper computationally to calculate molecular orbitals or overlapping functions than with STOs. Basis sets come in a hierarchy, dependent on their size. The larger the basis set, the more accurately the electrons are described, though also the larger the computational cost. Single zeta (SZ) basis sets use a single basis function to describe each valence orbital. Split-valence basis sets represent the valence orbitals using more than one basis function. Different functions have different ranges and describe interactions at a larger spatial extent from the nucleus. There are double (DZ), triple (TZ) and quadruple zeta, *etc.* basis sets. Additional functions, namely diffuse and polarisation functions, can be added to a basis set to further increase accuracy. Diffuse functions are important for describing anions, as they allow description of the electrons further away from the nucleus. Polarisation functions allow orbitals to adapt in the presence of other electrons.

In this work, DZ basis sets were used in combination with the pseudopotential (Section 3.8) in the CP2K code. In Gaussian 16, the 6-31G (d,p) basis set was employed. This basis set comprises of 6

primitive Gaussians for each core atomic basis function, 3 primitive Gaussians to describe the inner valence basis function and 1 primitive Gaussian to describe the outer valence basis function, with diffuse and polarisation functions.

3.10. Codes

3.10.1. CP2K

CP2K is a free software package that can be used for all types of systems, but is especially utilised for computationally efficient AIMD calculations. One of the methods implemented in CP2K that allows for fast DFT calculations is the Gaussian and plane wave (GPW) method. This method involves combining localised basis functions with plane waves to reduce the computational resource that would be required for plane wave only approaches. CP2K employs multiple grids for different plane wave energies. In this thesis, five multigrids with a cutoff of 1100 Ry and a relative cutoff of 70 Ry was employed. The DZVP-MOLOPT-SR-GTH basis set was used for all production runs. This is a DZ (Section 3.10) valence description with polarisation functions. MOLOPT refers to the basis sets being optimised for systems with localised electron density, and GTH signifies the pseudopotential (Section 3.8). Further details are described in the appropriate chapters.

3.10.2. VASP

The Vienna ab initio simulation package (VASP) specialises in the simulation of periodic systems with plane wave methods. In this thesis, VASP was employed for core-level calculations, in the initial state (IS) and the final state (FS) approximations. In VASP, these electronic level calculations are carried out by first calculating the valence structure using the PAW potentials, then freezing the valence electrons while the core electrons are unfrozen for the core level calculation. For the FS method, the valence electrons are unfrozen following the simulated ejection of the core electron. In the IS approximation, core level binding energies (E_B) are calculated in the given geometry which

then require conversion into E_B. In the FS approximation, an electron is simulated as leaving the specified core level into vacuum, by keeping the number of valence electrons fixed. VASP version 6.1.1 was also used to calculate the site potentials, which is the average of the electrostatic potential at the atom core.

3.10.3. Gaussian 16

Gaussian 16 is a program best suited for molecular calculations when using limited computational power. It is very easy to use as it is developed with GaussView 6 to visualise and extract data in an intuitive manner. Gaussian 16 employs localised basis functions and it was used in this thesis for gas phase lone ion calculations in Chapter 4.

3.11. Facilities

The computational facilities used in this work include local and national computing resources. Locally, a high-performance computing tower consisting of an 8 core Intel Core i9-9900K Processor with 32 Gb RAM was utilised.

National resources used were YOUNG, ARCHER and ARCHER2. YOUNG is part of the UK Materials and Molecular Modelling Hub for computational resources, which is partially funded by EPSRC. It consists of Xeon Cascade Lake hardware with 40 core nodes. ARCHER consisted of Cray XC30 hardware composed of 24 core nodes. ARCHER2 is composed of HPE Cray EX hardware with 128 core nodes.

YOUNG, ARCHER and ARCHER2 were used equally as the primary computing resources for the theoretical portion of the work presented in this thesis.

4. Understanding X-ray photoelectron spectra of ionic liquids: experiments and simulations of 1-butyl-3-methylimidazolium thiocyanate

4.1. Abstract

We demonstrate a combined experimental and computational approach to probe the electronic structure and atomic environment of an ionic liquid, based on core level binding energies. The 1-butyl-3-methylimidazolium thiocyanate [C_4C_1Im][SCN] ionic liquid was studied using *ab initio* molecular dynamics and results were compared against previously published and new experimental X-ray photoelectron spectroscopy (XPS) data. The long-held assumption that initial-state effects in XPS dominate the measured binding energies is proven correct, which validates the established premise that the ground state electronic structure of the ionic liquid can be inferred directly from XPS measurements. A regression model based upon site electrostatic potentials and intramolecular bond lengths is shown to account accurately for variations in core-level binding energies within the ionic liquid, demonstrating the important effect of long-range interactions on the core-levels, and throwing into question the validity of traditional single ion pair ionic liquid calculations for interpreting XPS data.

 KRJL and RGC conceptualised the study and supervised the

work. EG performed the computer simulations, with guidance from SDM and RGC. JMS, KRJL and RS contributed the experimental measurements and methods. EG wrote the original manuscript draft, with contributions from all authors.

4.2. Introduction

Ionic liquids (ILs) are liquids composed exclusively of ions. Their interesting potential properties, including large electrochemical windows, wide liquid ranges, tunability and low melting points,[14, 152] make them desirable for a range of applications, from catalysis to batteries.[6, 27, 153-155] Macro and mesoscopic properties, unique to each IL, are determined by interactions between the cation and anions.[156] A thorough study of molecular-level interactions in ILs could lead to a method to predict structure, properties and reactivity,[157, 158] and eventually suitability for specific applications. The donation of electron density from anion to cation, often termed charge transfer, has been debated in the IL literature, along with the importance of ion polarisability.[32, 37] The distance-dependence of electronic cation-anion inter-ion interactions for ILs, particularly important for understanding the dynamics of ILs, is currently unclear. Furthermore, the range of electronic environments present in the IL has been probed computationally, but not compared to experimental data.[128, 159]

X-ray photoelectron spectroscopy (XPS) is a very useful tool to understand these interactions. XPS has traditionally been used on solid or gaseous samples, due to the required ultra-high vacuum conditions (UHV).[89, 160] XPS can, however, be applied to ILs as they exhibit very low vapor pressure, and therefore are part of a limited group of liquids that can be studied using standard UHV XPS apparatus.[103, 161, 162] XPS has been used for ILs to probe both surface geometric structure (*e.g.* by varying the IL surface-detector angle)[163-165] and bulk electronic structure.[14] The study of ILs *via* XPS offers many opportunities, but also faces several obstacles.

Core-level binding energies, E_B, can be used to understand the electronic structure of ILs as E_B is the difference between the ground state and an excited state with a core hole.[166, 167] E_B shifts are caused by valence electron behaviour, which in turn is affected by the chemical environment around the ion. The position of the core level peak in the ground state, relative to the vacuum (or at times the

Fermi level for experimental data), determines what is called the initial-state (IS) in E_B. The ground state electronic structure is related to the atomic environment, *i.e.* bonding and interactions. When an electron is photoemitted from the core level, the other core and valence electrons relax. The magnitude of this relaxation affects the E_B value and is called the final-state (FS) effect.

Inter-ion electronic effects of the anion on the cation have been demonstrated using XPS; however, whether this effect is due principally to IS or FS effects is unclear.[36] It is usually assumed for XPS of ILs that IS effects dominate the measured E_B. [36, 102, 168-206] It is an important assumption because, if correct, it means that experimental E_B shifts give valuable clues to ground state electronic structure of ILs. Many studies have been carried out under this assumption, relating E_B of core levels to atomic charge, oxidation state, or electronegativity, to understand and potentially make predictions on structure and reactivity.[36, 102, 168-206] However, this assumption has so far proved impossible to establish exclusively using experimental methods; core-level E_B values have been compared to shifts in near edge X-ray absorption fine structure (NEXAFS) spectroscopy edge energies and Auger parameter values to try to determine the relative influence of IS and FS effects in XPS for ILs.[207, 208]

The combination of experimental E_B and theoretical models to study ILs has had limited use to-date. It has been applied to study partial charges and models of a single ion or a pair (one anion with one cation).[36, 88, 205, 206, 208] Two studies reported calculations on larger model systems (ion 'clusters', up to eight ion pairs), but comparisons were only made for valence levels, not for core levels.[209, 210] Comparisons of core E_B to calculated atomic charges have also been made, which are based on the assumption that IS effects dominate E_B shifts.[36, 205, 207, 208 209] E_B of core levels have been calculated for ILs, [206] but rarely are core holes explicitly included and only on small scale systems such as lone ions or ion pairs.[88, 180]

The XPS signal from an IL arises from contributions from a distribution of E_B values that reflects the range of chemical environments coexisting in the IL. Thus, the broadening of an experimental XPS core level peak has the potential to give information on the geometric structure of a sample.[211] The full width at half maximum (FWHM) of a measured core-level peak will contain contributions from a range of factors, including: X-ray source and analyser resolution from the apparatus[212], charging[97], core-hole lifetime[213] and sample geometric structure effects[214]. For XPS of liquids, only

water FWHM have been widely published; the structural disorder contribution to the FWHM for liquid phase water and ions solvated in water is around 1.0 eV[214, 215]. The experimental FWHM was interpreted in relation to the liquid phase geometric structure, *e.g.* the hydrogen bonding in liquid water[215]. For ILs, no investigations of the structural disorder contribution to the FWHM have been made. Developments in *ab initio* molecular dynamics (AIMD) have seen improvements in speed and accuracy, [113] which has allowed its use in the simulation of ILs.[109, 113, 141, 216-228] Despite this, no theoretical studies of core levels in bulk liquid phase with explicit ions have been carried out on ILs, to the best of our knowledge. A combined approach is required, including computer simulations validated by experimental data, such as peak positions and broadening.

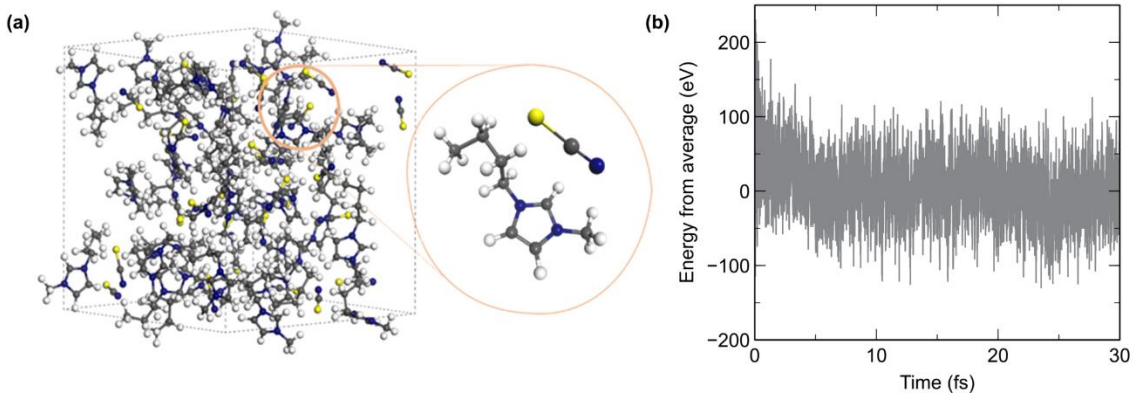

Figure 4.1 (a) Simulation cell used in this work, which is repeated under periodic boundary conditions. The cell consists of 32 pairs of $[C_4C_1Im][SCN]$ to create a disordered liquid phase. (b) Potential energy of the system at each time step over the course of the AIMD calculation. A configuration for further core hole calculations was taken at a step with average energy to produce 32 conformers.

In this work, we present a theoretical study of core-level E_B values and distribution in a bulk IL system, $[C_4C_1Im][SCN]$. Experimental XPS data is available for $[C_4C_1Im][SCN]$ in the literature.[207, 208] AIMD is used here to simulate a bulk model of this IL, which was chosen due to desirable properties of both the anion and the cation. $[C_4C_1Im]^+$ is one of the most commonly studied cations and further understanding of its behaviours will be an asset in several areas of research. Its relatively small size is convenient for expensive AIMD calculations. The anion, $[SCN]^-$, is also small. The negatively charged S and N atoms potentially allow for hydrogen bonds to be created in the bulk

system.[207, 208] $[SCN]^-$ is particularly interesting as it is a pseudohalide, yet $[C_4C_1Im][SCN]$ has one of the lowest viscosities among ILs,[229] in contrast to $[C_4C_1Im]^+$ $[PF_6]^-$, for example.[230] Core E_B values were calculated using density functional theory according to two approximations: i) including IS effects only (we call this the IS approximation), and ii) including both IS and FS effects via explicit consideration of the core hole (we call this the FS approximation). We demonstrate an excellent match between experiment and calculations. We show that IS effects are the major contributor to experimental core level E_B, a significant contribution to the sphere of researching ILs using XPS methods. Variation of E_B(core) was assessed in relation to a range of interactions, only possible within a bulk calculation. A model that describes the variations of E_B within the IL is presented. The structural disorder contribution to FWHM was compared between theory and experiment.

4.3. Experimental Methods

X-ray Photoelectron Spectroscopy

Liquid jet XPS measurements for K[SCN] in water were carried out at the UG-49 (SOL^{3}PES end-station) at the BESSY II electron storage ring.[231] The Sol^{3}PES experimental setup is equipped with a Scienta Omicron R4000 HIPP-2 hemispherical electron analyser. K[SCN] (Sigma-Aldrich, purity ≥99.0%) was dissolved in ultra-pure water. The mole fraction of K[SCN] in water was x = 0.01, *i.e.* 0.5 M. Non-resonant XPS regions were recorded at $h\nu$ = 700.0 eV. The pass energy was 100 eV. The analyser angle was 54.7° (magic angle geometry). All non-resonant XP spectra were fitted using the CASAXPS software. Fitting was carried out using a Shirley background and GL30 line shapes (70% Gaussian, 30% Lorentzian). Photoelectron spectra E_B for $[C_4C_1Im][SCN]$ were effectively charge referenced to the literature value of $E_B(C_{alkyl}\ 1s)$ = 289.58 eV (which corresponds to alignment with vacuum).[91] Photoelectron spectra E_B for K[SCN] in water were charge referenced to $E_B(N_{anion}\ 1s)$ = 402.37 eV, as $E_B(N_{anion}\ 1s)$ = 402.37 eV for $[C_4C_1Im][SCN]$ when charge referenced to $E_B(C_{alkyl}\ 1s)$ = 289.58 eV. Experimental data for all $[C_4C_1Im][SCN]$ measurements was taken from an earlier publication by our group,[109] where all the experimental details may be found.

4.4. Computational methods

Ab initio Molecular Dynamics

A 32 ion pair model of $[C_4C_1Im][SCN]$ with a density of 1.07 g cm^{-3} [232] was simulated using AIMD with the Quickstep code in CP2K, based on the Gaussian and plane waves method (GPW) and using the direct inversion in iterative subspace (DIIS) technique. After pre-equilibration using the classical force field DREIDING, the AIMD simulation was run for 30 ps with a timestep of 1 fs. The potential energy variations were equilibrated after less than 10 ps of AIMD. This simulation was carried out at 398 K controlled by Nosé thermostat in the NVT ensemble. The PBE functional[138] was employed, with D2 corrections by Grimme[150, 233] to account for dispersion interactions. A configuration at the end of the simulation, with energy close to the average, was extracted to carry out core-level calculations. An increased temperature of 398 K reduces viscosity and allows for equilibrium to be achieved faster, thus reducing the computational cost of the calculation while remaining in a range safe from thermal decomposition.

Core-Level Calculations

Calculations of E_B(core) were carried out in the Vienna Ab Initio Simulation Package (VASP).[145] A snapshot configuration with an energy close to the AIMD average was chosen to calculate the distribution of E_B values across the 32 ion pairs. The core-level calculations also used the PBE exchange correlation functional employed for the AIMD. The core-valence electron interactions were described using projector augmented wave (PAW) potentials.[146, 149] The number of planewaves in the basis set expansion of the wavefunctions was chosen by setting the kinetic energy cutoff to 400 eV. All core level energies of the system were calculated in this same configuration, for IS and

FS. Test calculations showed that the distribution of binding energies was not significantly affected by choosing or adding other configurations.

The IS approximation to calculate E_B(core), as defined in this work, is obtained from the Kohn-Sham (KS) orbital energies. The KS orbital energies are calculated after a self-consistent calculation of the valence charge density. No core hole is produced, and therefore any core hole-related effects are omitted. Only IS effects influence E_B and the orbital energies, or core levels (CL), are converted to E_B simply, by:

$$E_B = -CL \quad \text{Eq. 4.1}$$

These values, as obtained from VASP, are aligned with an internal energy reference, so only relative values are meaningful. Here, we shifted the calculated core-level values to match experiment, as explained below.

In contrast, for the FS approximation, the calculation involves creating a core hole explicitly. In the FS method used in VASP, it is assumed the nuclei are static, due to the timescale of the excitation of an electron. Additionally, the other core electrons in the atom are not allowed to relax once the core hole has been created. This may create a slight error, specifically in relation to a lack of lifetime broadening of the resultant peak. The energy extracted is the total energy of the system, including the core hole. This means that the calculated energy is again useless as an absolute energy, and only relative energies can be used. In this work, we have aligned the average FS energy with the average IS energy, to give FS values that are comparable with experiment. This method provides an internal comparison of values, *i.e.* the absolute value has no inherent meanings, other than its relation to other E_B values. Absolute energies were not considered, but rather the difference between energies (ΔE_B).

Molecular Calculations

Test calculations of isolated $[SCN]^-$ anions were performed using Gaussian16.[234] These single point energy calculations were carried out with the 6-31g(d,p) basis set[235, 236] and the B3LYP functional.[139] These tests were designed to separate intra-ion from inter-ion contributions to E_B. Intra-ion

interactions were characterised by the lengths of S-C and N-C anion bonds. One bond was kept constant while the other was modified. The constant bond length was determined by taking an average of the 32 bond lengths in the configuration. For S-C, this was 1.65 Å and for N-C it was 1.20 Å. The same method in Gaussian16, as above, was used to optimise the ions with the second bond length varied at an interval of 0.02 Å, and the E_B was extracted from orbital energies. We studied short-range interactions by extracting radial distribution functions (RDFs) and visually assessing each anionic environment.

Gaussian-Lorentzian Peaks

A Gaussian Lorentzian Product (GLP) function is one of several types of functions used to fit peaks in experimental XPS measurements.[237] XPS peaks are typically expected to be Lorentzian, but due to the various sources of broadening, this shape is distorted and compensated for by including Gaussian mixing in the function. To form a peak from the 32 data points for each core level, Eq. 4.2 was applied to the values; where mixing parameter, m, was set to 0.3 as in experimental peak fitting. Values 0 and 1 are pure Gaussian and pure Lorentzian respectively. The function width, F, was set at either 0.7 eV or 1 eV for high resolution and survey scan peaks, respectively.

$$\mathrm{GLP}\,(x; F, E, m) = \exp\left[-4\ln 2\,(1-m)\frac{(x-E)^2}{F^2}\right] \Big/ \left[1 + 4m\,\frac{(x-E)^2}{F^2}\right] \qquad \text{Eq. 4.2}$$

In the investigation of ILs using XPS, survey scans are typically used to determine the presence of impurities of the sample. They are measured to see what elements are present, and their abundance, using a high pass energy and low resolution. These settings result in greater apparatus broadening contributions to the peaks. High resolution scans are measured with low pass energy. These are used to identify chemical states and typically have lower broadening than survey scans. Calculated peaks were slightly shifted in position and normalised by intensity for improved comparison with

experiment. Values were shifted by +21.2 eV and +27.0 eV and intensities corrected by the height of the C 1s peak.

4.5. Results and Discussion

4.5.1. Initial-State vs Final-State Approximations to the Core-Level Binding Energies

A comparison between calculated binding energies in the IS and FS approximations was carried out to identify the dominant effects. Since the calculation in the FS approximation includes both IS and FS effects, a strong positive linear correlation (Figure 4.2) is reasonable confirmation that FS effects are minor, and therefore IS effects are the primary influence on E_B(core). E_B(S 2p) values calculated in the FS approximation showed strong correlations with the corresponding values calculated in the IS approximation (R^2 = 0.950). Correlation between results in the IS and FS approximations was also good for E_B(N 1s) (R^2 = 0.995), although the correlation is weaker if N_{anion} and N_{cation} are considered separately (R^2 = 0.77 and R^2 = 0.74, respectively). The reason why the E_B(N 1s) were more affected by FS effects than $E_B(S_{anion}\ 2p)$ was investigated further, and it will be discussed below.

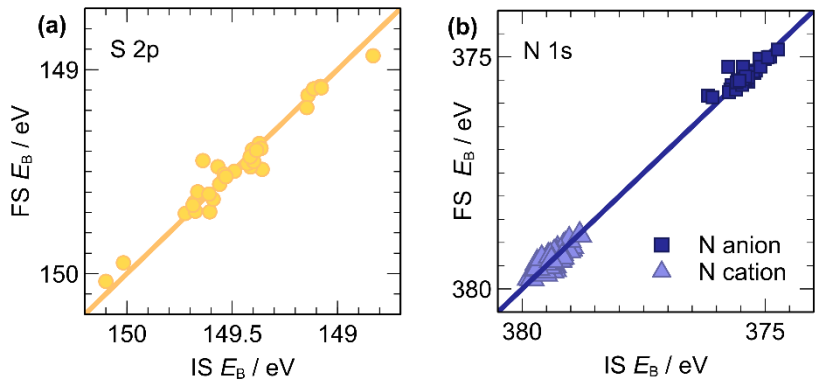

Figure 4.2 Linear correlations between binding energies calculated in IS and FS approximations for (a) E_B(S 2p) and (b) E_B(N 1s). The $y = x$ line is plotted as a guide. R^2 = 0.95 (a), 0.77 (b, anion) and 0.74 (b, cation).

The deviations from the y=x line in these plots are due to final-state effects. However, these deviations are small in comparison with the spread of the values: in Figure 4.2a (for S2p core levels) the maximum absolute deviation is 0.19 eV and the mean absolute deviation is only 0.04 eV, in a range of 1.3 eV. In Figure 4.2b (for N 1s core levels), the maximum absolute deviation is 0.54 eV but the mean absolute deviation is only 0.09 eV, in a range of 5.0 eV.

The conclusion about the absence of strong FS effects is important because it means that XPS E_B can be related directly to the ground state electronic structure of the IL, which is the primary reason we turn to XPS to study these systems. Furthermore, it facilitates our theoretical study of the distribution of core-level binding energies in the IL bulk liquid, because calculations in the IS approximation are computationally cheaper and much simpler: in this case, one single-point calculation produces 32 to 64 data points, whereas in the FS approximation, individual calculations explicitly including a core hole at each atom in the liquid are required for each data point. In what follows, the reported binding energies were obtained in the IS approximation, unless otherwise stated.

Having established the validity of the IS approximation, the accuracy of the calculated distribution of E_B(core) was tested against experiment. The experimental survey XP spectrum was plotted and compared against our calculated survey spectrum (Figure 4.3). Quantitative and qualitative analysis of neighbouring peaks showed the overall accuracy of the computed results to be high, despite the omission of FS effects. Most E_B separations are within a 3.5% deviation from experiment. In particular, a high-resolution scan comparison shows $\Delta E_B = E_B(N_{cation}\ 1s) - E_B(N_{anion}\ 1s)$ are 4.1 eV in experiment and 4.0 eV in calculated peaks (Figure 4.3b), which is in excellent agreement. The only significant discrepancy in the survey scan plot is a calculated 55.2 eV separation between S 2s and S 2p levels, whereas in experiment the separation was 64.2 eV; this is almost a 9 eV change between the two sets of results, or a 14% error.

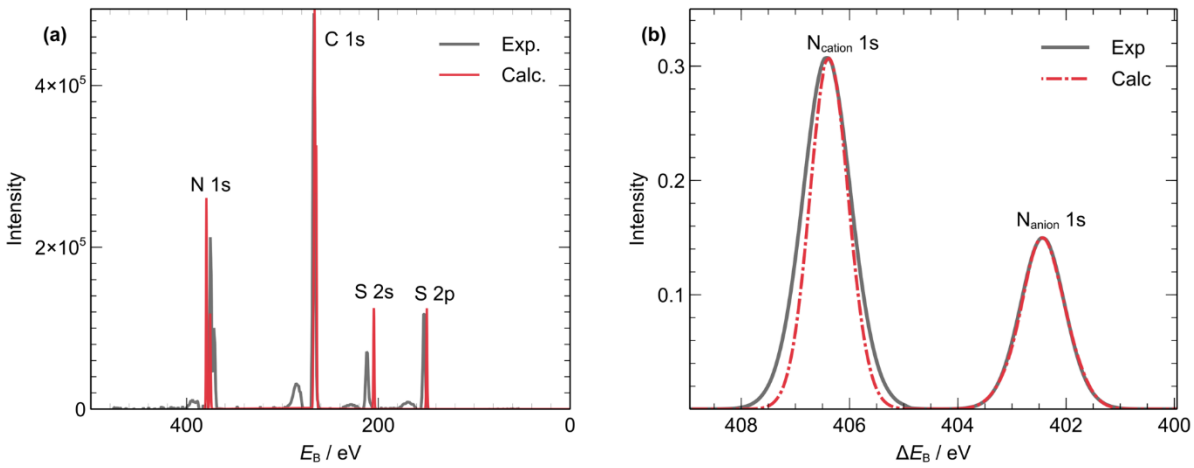

Figure 4.3 Initial-state effect calculations. (a) Experimental survey scan (grey) overlayed with the calculated survey scan (red). Calculated scan was shifted by +21.2 eV and intensities were corrected using the C 1s peak. The calculated peaks were broadened with a width of 1 eV to mimic experimental broadening. (b) High resolution scan of N 1s peaks. The calculated peaks were broadened with a 0.7 eV width to mimic experimental broadening and shifted by +27.0 eV. Small experimental peaks at higher E_B to main peaks are satellite peaks.

A comparison of C 1s peaks further confirmed the success of the IS calculations in replicating experimental measurements. Our new experimental data has shown the position of the C 1s anion peak from $[SCN]^-$, previously unidentified, alongside a fitting model used for the C 1s peak (Figure 4.4a).[238] This fitting model, as discussed in Section 2.1.4.2, was developed after measurement of high resolution experimental XPS C 1s spectra, which clearly shows a single wide peak with a shoulder. The width of the peak and the shoulder suggest multiple environments, which are fitted according to how many hetero atoms they are bonded to: C_{alkyl}, C_{hetero} and C^2. Visual comparison of experimental and calculated peaks from this work (Figure 4.4b) of the same species shows very good agreement – each peak position is matched within 0.1 eV. The experimental FWHM of C bonded to a single N (blue, C_{hetero}) is larger than the calculated, due to the unresolved $[SCN]^-$ contribution in the experimental fitting.

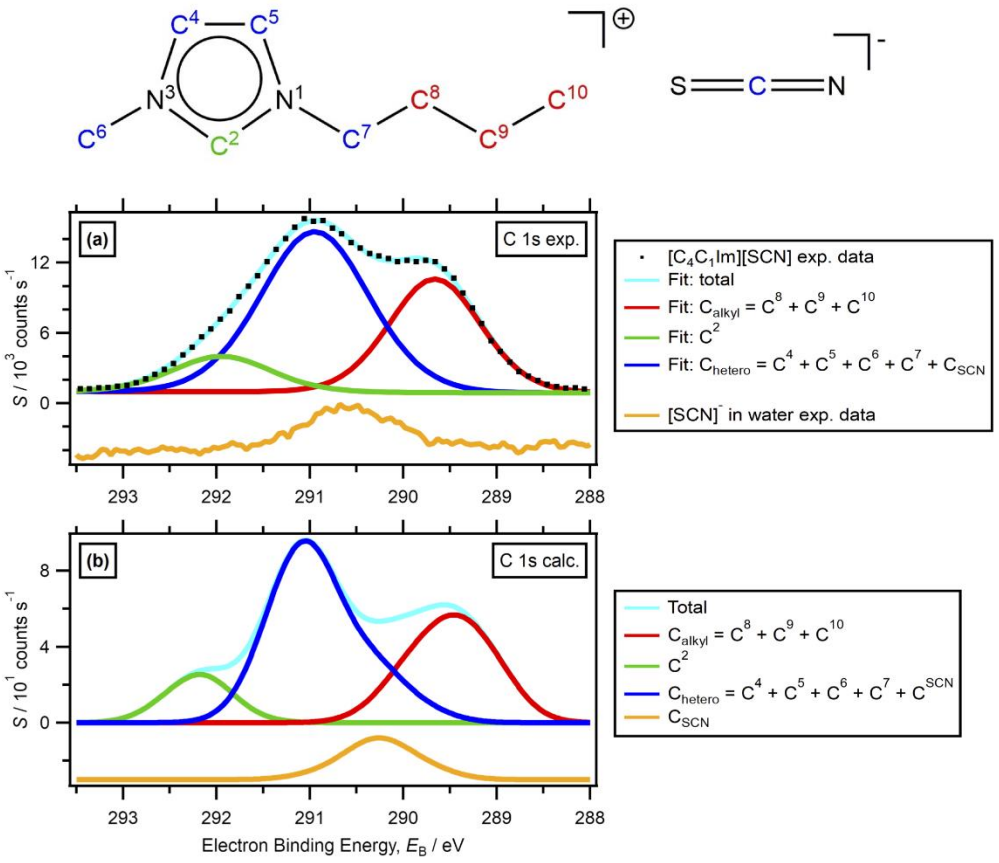

Figure 4.4 C 1s XPS. (a) Experimental C 1s peak fitting model for $[C_4C_1Im][SCN]$ published in reference 93; fitted with peaks for C_{alkyl}, C_{hetero} and C^2. C_{hetero} is likely to contain contributions from the C_{anion} peak, increasing its FWHM. Experimental peak of C_{SCN} from K[SCN] in water. (b) Peaks calculated in this work, with a width function of 1 eV (see Section 2.5 for more details), separated into C_{alkyl}, C_{hetero}, C^2 and C_{anion}. Calculated C_{SCN} extracted for comparison to experimental E_B. Charge referencing for XP spectra is explained in Section 2.1.

4.5.2. Peak Broadening

In E_B calculations, instrumental and lifetime broadening are not simulated. A comparison between measured and calculated data of N_{anion} 1s and N_{cation} 1s peaks shows a very good N_{anion} 1s broadening match and a good N_{cation} 1s match (Figure 4.3b). A visual assessment of the same plot, but with a 0.5 eV width function, shows that the peaks do not match as well, and some asymmetry is present (ESI Figure A1). Experimental broadening for this data set is estimated as apparatus contributions of ~0.45 to 0.65 eV and lifetime contributions of 0.054 eV and 0.115 eV for S 2p and N 1s respectively,

totalling ~0.5 eV;[95, 239] charging contributions are negligible.[238] Using an apparatus broadening value of 0.65 eV, the calculated structural broadening values were found to be in the range of 0.55 eV to 0.82 eV.

Testing increased sample sizes did not increase the N_{cation} 1s peak width to provide a better match to the experimental width, and only a slight improvement in peak symmetry was noted. There are two possible explanations for the slight peak width discrepancy in the spectrum; i) the AIMD calculation is lacking accuracy in the disorder description of the system, or ii) the experimental broadening value is underestimated. As the experimental broadening value is not an exact estimate and is likely to fluctuate between calibration and successive experiments, we believe the latter is the most likely source of the slight discrepancy.

4.5.3. Effects of Intra-Ion and Inter-Ion Interactions on the Core-Level Binding Energies

Intra-ion interactions were analysed through comparison of S-C bond length to the relevant $E_B(S_{anion}$ 2p) and N-C bond length to $E_B(N_{anion}$ 1s). Both plots produced a weak linear correlation (Appendix Figure A2). Visual assessment and the RDFs for the analysis of short-range interactions did not produce a clear pattern of short-range interactions in relation to E_B, and this was not investigated further. Neither short-range or intra-ion effects were found to be the dominant influence over E_B fluctuations. Longer-range interactions were characterised by calculating the site potential at each atom. The site potential is defined in VASP as the average of the electrostatic potential in the core region of a given atom. This site potential is affected by both short-range and long-range interactions. Plots of site potentials against E_B for each atom clearly demonstrated that $E_B(S_{anion}$ 2p) correlates almost perfectly with site potential, with very little deviation (Figure 4.5a). Although $E_B(N_{anion}$ 1s) also correlates very well with site potential, the deviation is slightly higher than for S 2p (Figure 4.5b). We successfully interpreted these patterns by further comparison with internal bond lengths in the form of a multiple regression model for E_B, based on both site potential and bond length values. The multiple regression produced a new model for E_B prediction (Figure 4.5c, 4.5d) which was compared against the actual calculated E_B. The model was found to be highly accurate,

with a root mean square deviation (RMSD) of only 0.01 eV and 0.02 eV for S_{anion} 2p and N_{anion} 1s respectively. In comparison to the linear regressions, which have RMSD values of 0.03 eV and 0.10 eV, respectively, accuracy is increased substantially, particularly for N_{anion} 1s.

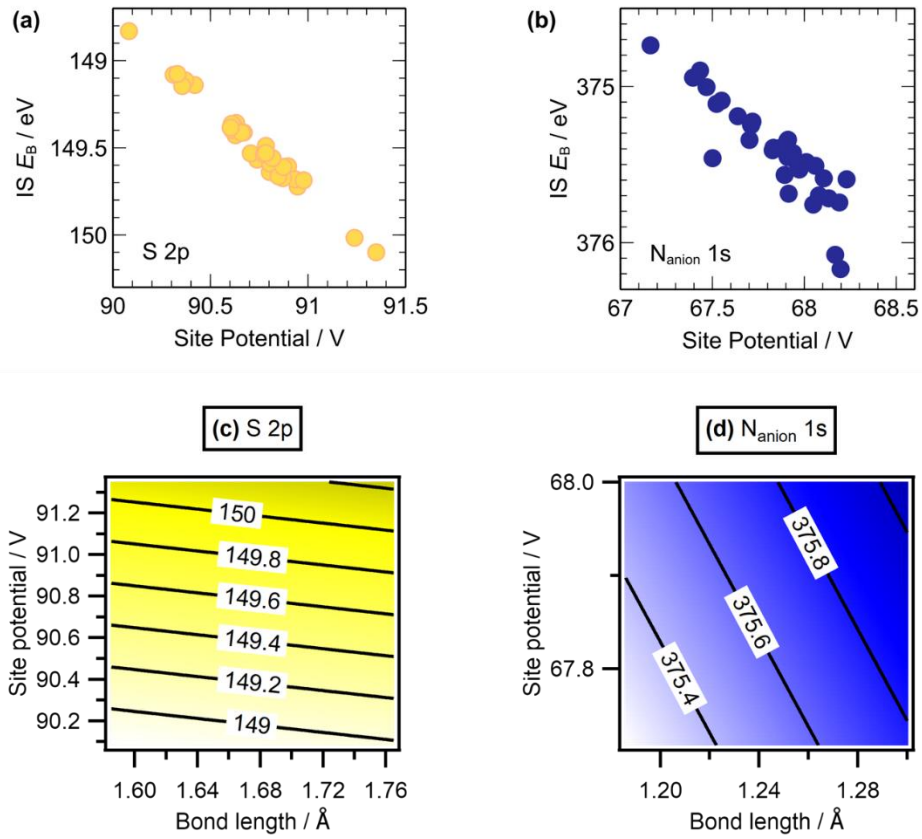

Figure 4.5 Correlation of IS E_B with site potential (SP) for a) S 2p (yellow) and b) N_{anion} 1s (blue). Contour maps of bi-linear prediction models for c) S 2p (yellow) and d) N_{anion} 1s (blue) with E_B being a function of both the site potential and the bond length.

The strong correlation of E_B(S 2p) with site potential was assumed to be the result of the large, highly polarisable nature of the atom.[240] The electron cloud is understood to be more susceptible to the influence of collective electrons in a disordered bulk IL system than an atom like nitrogen, which is smaller and denser than sulfur. The valence and core electrons of a nitrogen atom were expected to be influenced more strongly by the N-C internal bond length than the sulfur atom is by the S-C internal bond length, due to the higher electron density in the N-C bond. Calculations found that

when the S-C or N-C bond was altered in turn, the $E_B(N_{anion}\ 1s)$ undergoes higher energy changes with the same % bond length variation (Figure 4.6).

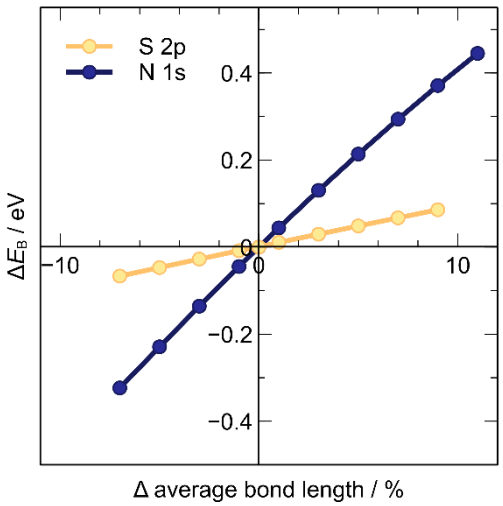

Figure 4.6. Plot of E_B change with variation of internal bond length in the anion $[SCN]^-$. Bond S-C for S_{anion} 2p and N-C for N_{anion} 1s.

The finding that E_B correlates very well with site potential shows that single ion pair studies are insufficient to describe the structure and interactions within a real IL system. Single ion or ion pair calculations are, by definition, based on the assumption that short-range or intramolecular interactions dominate E_B broadening. Gas-phase models seem to overestimate the cation-anion interaction when the long-range structure is missing.[241] A slight improvement to this is an implicit solvent model or ionic pair 'clusters'; however, these models cannot explicitly simulate long-range disorder of the liquid system. Focusing on a single ion pair increases chances of error when calculating E_B. This study found a ~1 eV range in E_B fluctuations for a single atom type (Figure 4.2). A single ion pair, especially when optimised, could fall within the extremes of this range, rather than in the middle, or average of this range of E_B. Particularly when resolving shifts of <0.5 eV, this value has been shown to be within our error margin and any findings related to a shift of this size may be entirely insignificant. This would likely result in inaccurate conclusions on the bulk system.

4.6. Conclusions

This study found a strong correlation between experiment and DFT calculations, demonstrating for the first time that IS contributions were the primary contributor to E_B values in the IL $[C_4C_1Im][SCN]$. This system is representative of a wide array of ILs, suggesting that IS effects would be the primary contributor to most ILs. This finding suggests that either FS effects are negligible or are similar across all atoms, so do not contribute to peak separations. Furthermore, we confirm that the effect of the anion on the cation, observed using XPS for many ILs, was driven by an IS effect; moreover, charge transfer can be confirmed as occurring in the ground state. We confirmed that E_B was closely linked to site potential in the anion of $[C_4C_1Im][SCN]$. Site potential is influenced by all (both short- and long-range) interactions of the bulk system. We found no evidence to show that short-range, intermolecular interactions are sufficient on their own to describe the liquid phase E_B variation. Site potential did not offer a perfect correlation with E_B. The discrepancy was found to mostly correspond to intramolecular bond length fluctuations. With both site potentials and internal bond lengths, we produced a predictive model for E_B, which was found to be highly accurate for this IL.

5. Effects of chain length, anion and temperature on X-ray photoelectron spectra of ionic liquids

5.1. Abstract

Following the development of a method for the theoretical prediction of core-level XP (X-ray photoelectron) spectra in ionic liquids (ILs) in the previous chapter, the work in this chapter explores the validity of this method across a range of four additional imidazolium-based, $[C_nC_1Im]^+$ cation, ILs. This group of ILs was carefully selected for variation of cation alkyl chain length and anion choice. Investigation of the impact that the cation or anion choice has on IL electronic structure can be extrapolated to how these changes affect macroscopic behaviours, in theory. The effects of cation chain length, the choice of anion and the temperature at simulation on core binding energies (E_B) were explored. The accuracy of this method is further established, as the agreement between experimental and calculated E_B is found to be excellent.

The conceptualisation of this work was by KRJL and EG. EG is the primary author and contributor to the computational procedures. Experimental XPS data taken from previous work of our research group. Analysis carried out by EG, with guidance from KRJL. Figures created by EG.

5.2. Introduction

The first of the modern air- and water-stable ILs to be synthesised, 1-ethyl-3-methylimidazolium tetrafluoroborate, $[C_2C_1Im][BF_4]$[12], contains an imidazolium ring in the cation. Following this discovery, research into imidazolium-based ILs has grown and they have become the most commonly studied of these materials. These ILs have particularly practical melting points and electrochemical stability.[242] Even this relatively specific cationic group offers incredible design freedom. Many variations of the organic component are easily synthesised, including variation in alkyl chain length or functional groups and anions provide a wide choice between organic and inorganic, in a range of sizes, *etc*. The tuneability that makes ILs so versatile also contributes to the difficulty of their characterisation; any adjustment to the cation or anion will affect the interionic interactions which contribute to the macroscopic properties of the liquid.

The physical and chemical properties of ILs can be correlated with their structure: both geometric and electronic. Structure influences cation-anion (*i.e*. interionic) interactions within the system, contributing to macroscopic behaviours. Gathering a vast database of IL macroscopic properties could enable the selection or guide the synthesis of an IL based on desired characteristics for any given application. Behaviours of interest to industry include viscosity, surface tension, transport properties, ideal glass transition temperatures, conductivity, thermal stability *etc*. Access to data on the interionic interactions and reactions is granted through the elucidation of electronic structure and behaviours. Measuring, or even simulating, every IL combination to create a database of these properties is unfeasible in the real world. One approach to achieve this aim is the development of a predictive system, which begins with the electronic study of a few carefully selected ILs. This method can produce results and patterns which can evolve into reasonable predictions, to be applied to structurally or electronically similar ILs.[91]

Increasing cation chain length has shown decreasing conductivities in ILs, such as $[C_nC_1Im][BF_4]$[243, 244] and $[C_nC_1Im][NTf_2]$. The biggest difference in conductivity is between $n = 2$ and $n = 4$. Increasing chain length is considered to increase interionic interactions, reducing the mobility of the ions. Anion variation has also been found to influence conductivity. For example, from Cl^- to $[BF_4]^-$

, conductivity increases with size, but decreases again for larger anions.[243] Anion effects on the physical properties of ILs also include changes to hydrogen bond donor and acceptor ability, with implications on solvation properties.[245] Temperature variation, though not directly affecting the IL structure, affects energy in the system and electronic differences may be observed. Conductivity, surface tension and viscosity in particular have been shown to change with temperature. Briefly mentioned in Chapter 4, an increased temperature in molecular dynamics (MD) simulation of liquids achieves a faster equilibration of the system due to increased ion mobility. Particularly in systems with high viscosity, equilibration would otherwise not be possible.

One way of measuring or defining the changes in interionic interactions is the phenomenon of partial charge transfer (CT). In ILs, due to the significant fluctuation in interactions between the ions, yet a large gap between the highest occupied molecular orbital (HOMO) and lowest unoccupied molecular orbital (LUMO) of the ions, the phrase CT denotes charge "sharing" rather than a formal donation. This effect has also been called "non-integer charge transfer". Ultimately, CT is a term employed in fundamental IL research to describe the strength of the interactions between the anion and the cation in an IL. Another approach to indexing the interaction ability or probability is the use of Kamlet-Taft parameters, β, indicating the ability as an electron donor, which is an indirect measure of basicity. [245-247]

Core-level X-ray photoelectron spectroscopy (XPS) is an experimental method that is used to investigate electronic behaviour.[160] The measured E_B are related back to the interionic interactions and geometric structure. For this relationship to be valid, the initial, unperturbed state of the system must be the main influence in the measurements. This assumption has been held in IL XPS research for many years, until the publication, from which Chapter 4 was adapted, demonstrated that indeed, the IS was dominant in experimental E_B measurements, using combined XPS experimental and computational methods.[83] This work not only demonstrated that results from experimental XPS shifts apply to the ground state behaviour, but also developed a method for simulating the core electronic behaviour in ILs with good accuracy.

Core XPS measurements for a range of ILs to determine the effects of the anion and cation have been carried out previously.[36, 93, 102, 164, 168, 169, 199, 203] In $[C_8C_1Im]^+$-based ILs, the choice of anion has

been found to affect the cation, causing E_B shifts on the imidazolium ring atoms; the smaller and more basic the anion, the stronger the interionic interactions, hence more charge is shared from anion to cation.[36] As the cation receives more negative charge, the imidazolium ring becomes less positively charged and more ready to surrender electrons in the XPS process, moving peaks to lower E_B. It was determined, using ion pair gas phase calculations, that anion-cation charge sharing was mostly dependent on proximity between the ions, rather than the extent of hydrogen bonding. Though a significant finding, this work did not confirm the results are relatable to the initial state (IS) effects, rather than being caused by final state (FS) effects. The IS is the system in its ground state, which, once perturbed by an X-ray, becomes the FS. Furthermore, calculations on gas phase ion pairs were shown to be unreliable in the conclusions from the work of Chapter 4, as they inherently cannot account for bulk long-range interactions.[83] These interactions were demonstrated to be the major contributing influence to E_B fluctuations.

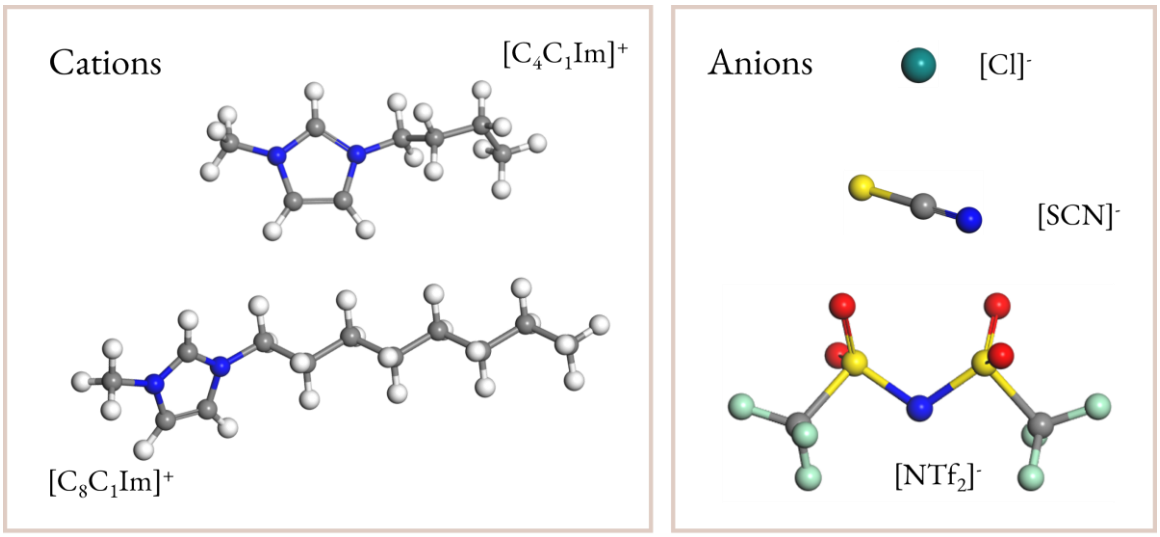

Figure 5.1 Structural representation of the constituent ions of all the ionic liquids investigated in this chapter. Atoms by colour are carbon (grey), nitrogen (blue), sulfur (yellow), oxygen (red), fluorine (light green) and chlorine (dark green).

The following chapter is an extension of the work presented in Chapter 4. The combined experimental and computational method using the IS approximation for the calculation of E_B was

applied to a larger range of imidazolium-based ILs, with the cation $[C_nC_1Im]^+$ where $n = 4$ or $n = 8$. E_B shifts of the range of ILs were compared. The scope of this chapter covers effects on core E_B shifts of cation alkyl chain length, anion variation and temperature effects.

The chosen ILs for this area of the work were $[C_4C_1Im][SCN]$ (from Chapter 4), 1-octyl-3-methylimidazolium thiocyanate, $[C_8C_1Im][SCN]$, 1-butyl-3-methylimidazolium bis(trifluoromethylsulfonyl)imide, $[C_4C_1Im][NTf_2]$, 1-octyl-3-methylimidazolium bis(trifluoromethylsulfonyl)imide $[C_8C_1Im][NTf_2]$ and 1-octyl-3-methylimidazolium chloride, $[C_8C_1Im]Cl$. The structures of the ions in these ILs are represented in Figure 5.1. These ILs were carefully selected to represent a wider array of ILs, based on the existing experimental XPS data and the liquid properties affected through changes to the anion. Investigation of cation chain length effects required a choice of ILs with the most contrasting alkyl chain lengths. The $[C_8C_1Im]^+$ cation was selected for comparison to $[C_4C_1Im]^+$ as $n = 8$ is the longest alkyl chain of the $[C_nC_1Im]^+$ ILs that remains in the liquid state at room temperature, maintaining consistency with the XPS measurements of the other ILs. Furthermore, it has been suggested that $E_B(C_{alkyl}\ 1s)$ remains at the same value in chain lengths of ≥8 carbons, important for experimental charge referencing in XPS.[102] The anion $[NTf_2]^-$ is bulky, flexible and contains halogen atoms – the opposite of $[SCN]^-$. Cl^- is small, symmetrical, and the IL $[C_8C_1Im]Cl$ has a low enough viscosity to be able to simulate it using *ab initio* molecular dynamics (AIMD), while being closely representative of $[C_4C_1Im]Cl$. $[C_8C_1Im]Cl$ also has a melting point low enough to make XPS measurements in its liquid state at room temperature possible.

Chapter 4 reported results that demonstrated the dominating influence of IS on the core level energies of the ionic liquid $[C_4C_1Im][SCN]$. Although the results showed very good agreement with experimental data and supported this assumption in the chosen IL, a larger dataset is desirable to apply this conclusion to a wider range of ILs. Analysing the data for this collection of ILs would produce a far more comprehensive conclusion regarding the influence of the IS on core E_B shifts.

5.3. Computational methods

The methods from Section 4.2 for AIMD and core-level calculations were applied in the work of this chapter. Other than the data for Figure 5.2, E_B for all ILs studied in this chapter were calculated using the IS approximation. These methods were applied to the ILs $[C_8C_1Im][SCN]$, $[C_4C_1Im][NTf_2]$, $[C_8C_1Im][NTf_2]$ and $[C_8C_1Im]Cl$. The data for 1-butyl-3-methylimidazolium thiocyanate, $[C_4C_1Im][SCN]$, was taken from the previous chapter. The densities were set as 1.01 g cm^{-3}, 1.44 g cm^{-3}, 1.32 g cm^{-3} and 0.97 g cm^{-3} for $[C_8C_1Im][SCN]$, $[C_4C_1Im][NTf_2]$[248], $[C_8C_1Im][NTf_2]$[249] and $[C_8C_1Im]Cl$[250] respectively. For consistency, the geometry at step 20,000 of the AIMD was extracted for the core level calculations for each IL.

Calculated peaks for C 1s experimental *versus* computational data comparisons were referenced to the respective $E_B(C_{alkyl}\ 1s)$ for each IL, which were in turn effectively referenced to vacuum, as in Chapter 4. For N 1s experimental *versus* computational data comparisons, calculated peaks were referenced to the experimental $E_B(N_{anion}\ 1s)$ peak of the respective IL. The results considering calculated data only were referenced to the calculated $E_B(C_{alkyl}\ 1s)$ peak position of $[C_8C_1Im][NTf_2]$.

Intensities of the calculated peaks were only adjusted when plotting the calculated results against the experimental results, for practicality of comparison.

5.4. Experimental methods

The XPS data was taken from an earlier publication by our group.[238] All data was effectively charge referenced to $E_B(C_{alkyl}\ 1s) = 289.58$ eV, which is in alignment to vacuum.[91]

5.5. Results and discussion

5.5.1. Initial state vs final state

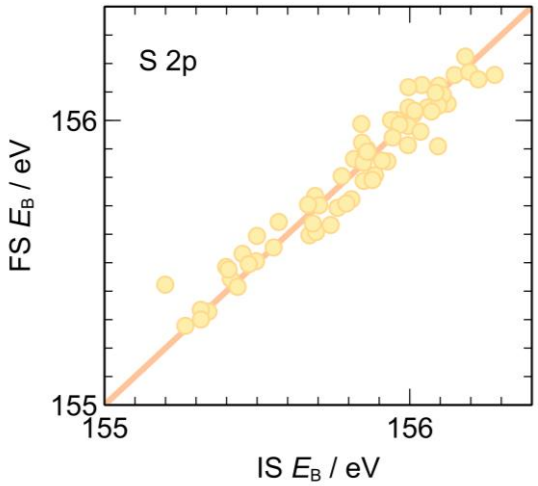

Figure 5.2 Plot of S 2p E_B calculated using the initial state (IS) approximation vs E_B obtained using the final state (FS) approximation for the IL $[C_4C_1Im][NTf_2]$.

The IS approximation to calculate EB involves taking the inverse of the calculated core level energy, while in the FS approximation, the removal of an electron from the selected core level and into vacuum is simulated and the energy calculated (Chapter 4). The comparison of the IS to the FS approximation was carried out in Chapter 4 for both S 2p and N 1s for $[C_4C_1Im][SCN]$. Plots of both sets of data showed a great linear correlation, confirming that IS dominates in resultant E_B. Although a breakthrough finding for the field of researching ILs using XPS, this was only demonstrated for a single IL. Further comparison of the IS approximation *versus* FS approximation in the $[C_4C_1Im][NTf_2]$ IL produced the same linear correlation observed for $[C_4C_1Im][SCN]$ (Figure 5.2). For the S 2p core level, maximum deviation is 0.22 eV, average deviation of 0.05 eV over a 1.08 eV range. In comparison, in the data for $[C_4C_1Im][SCN]$, the maximum absolute deviation is 0.19 eV and a mean absolute deviation of 0.04 eV, in a range of 1.3 eV. The difference is marginal between the two ILs, with the $[C_4C_1Im][NTf_2]$ showing a slightly higher deviation compared to the range of E_B, though this difference is not considered to be noteworthy. The difference in range of E_B is unexpected, as $[NTf_2]^-$ is a larger, more flexible anion, which may be expected to exhibit a higher range of environments for any of its atoms than the small, rigid $[SCN]^-$ anion. The range of E_B(Cl 2p) for Cl^- is even larger than S 2p for the $[SCN]^-$ anion, at 1.44 eV, so a pattern is observed. An explanation for this trend may be that with such large cations, a smaller and more basic anion causes a greater variation in the extent of electronic or charge sharing, as a result of reduced steric

hinderance. These charge sharing effects may influence the core levels more strongly than a larger range of geometries from a larger anion like $[NTf_2]^-$.

5.5.2. Temperature effects

The temperature at simulation of $[C_8C_1Im]Cl$ was 498 K, higher than all the other ILs at 398 K. This choice was necessary due to the high viscosity of $[C_8C_1Im]Cl$ (~0.900 Pa•s[230, 251] at 333 K compared to $[C_8C_1Im][NTf_2]$ at 0.023 Pa•s[252, 253] and $[C_4C_1Im][SCN]$at 0.017 Pa•s[229, 254]),which prevented equilibration at a reasonable timescale at 398 K using AIMD. Additional simulations of the remaining ILs ($[C_4C_1Im][NTf_2]$, $[C_8C_1Im][NTf_2]$, $[C_4C_1Im][SCN]$ and $[C_8C_1Im][SCN]$) were carried out at 298 K to assess the validity of E_B comparison across different temperatures. The results showed no change in N 1s E_B with respect to temperature for $[C_4C_1Im][SCN]$ and only a small change (0.10 eV) for $[C_8C_1Im][NTf_2]$, within the estimated error for this work (Figure 5.3). This result validates the comparisons of the ILs simulated at 398 K with $[C_8C_1Im]Cl$ simulated at 498 K in the following sections.

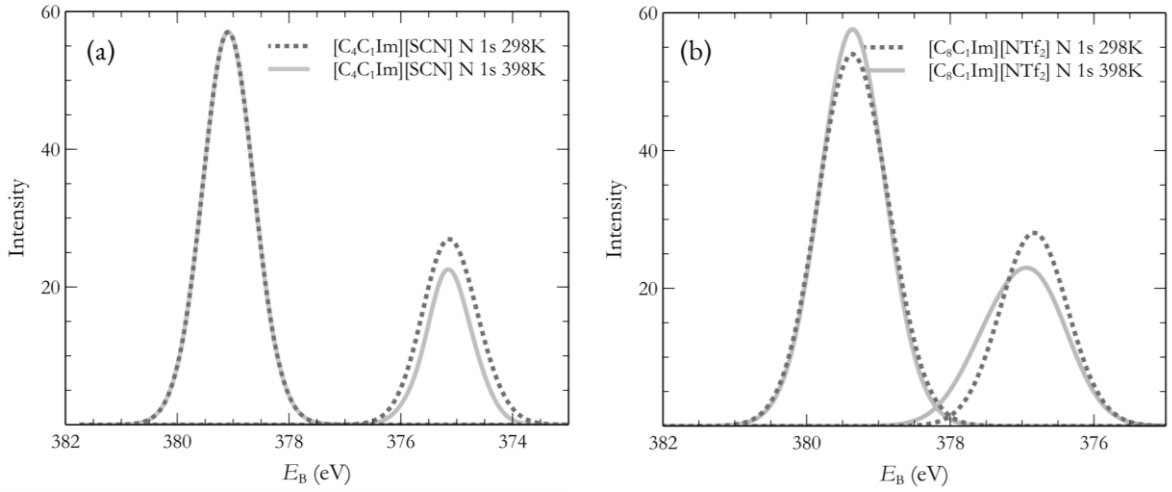

Figure 5.3 (a) Plotted calculated high-resolution N 1s peaks of $[C_4C_1Im][SCN]$ at 298 K and 398 K. **(b)** Plotted calculated high-resolution N 1s peaks of $[C_8C_1Im][NTf_2]$ at 298 K and 398 K.

5.5.3. Broadening and peak separations

The N 1s and C 1s peak E_B separations between experimental and calculated results were used to demonstrate the accuracy of the method applied in Chapter 4. Analysis of the same comparisons in the additional ILs studied in this chapter shows consistently high accuracy of the calculated XP spectra. (Figure 5.4). The calculated N_{cation}-N_{anion} 1s peak E_B separation in $[C_8C_1Im][SCN]$ is shown to be 4.10 eV, a 0.0 eV deviation compared to experiment (also 4.10 eV). Results in Chapter 4 for $[C_4C_1Im][SCN]$ showed a 4.00 eV E_B separation, a deviation of 0.1 eV from experiment (4.10 eV). The $[NTf_2]^-$-based ILs show a less ideal match, with a higher deviation of the calculated results from the experimental N_{cation}-N_{anion} peak E_B separation, although these are still within a reasonable error. The calculated N_{cation}-N_{anion} peak separation is 2.56 eV for $[C_4C_1Im][NTf_2]$, compared to 2.70 eV experimentally (Figure 5.4c), and 2.42 eV for $[C_8C_1Im][NTf_2]$, compared to 2.60 eV experimentally (Figure 5.4d). These results produce a 0.14 eV and 0.18 eV deviation from the experimental peak separation, for $[C_4C_1Im][NTf_2]$ and $[C_8C_1Im][NTf_2]$ respectively.

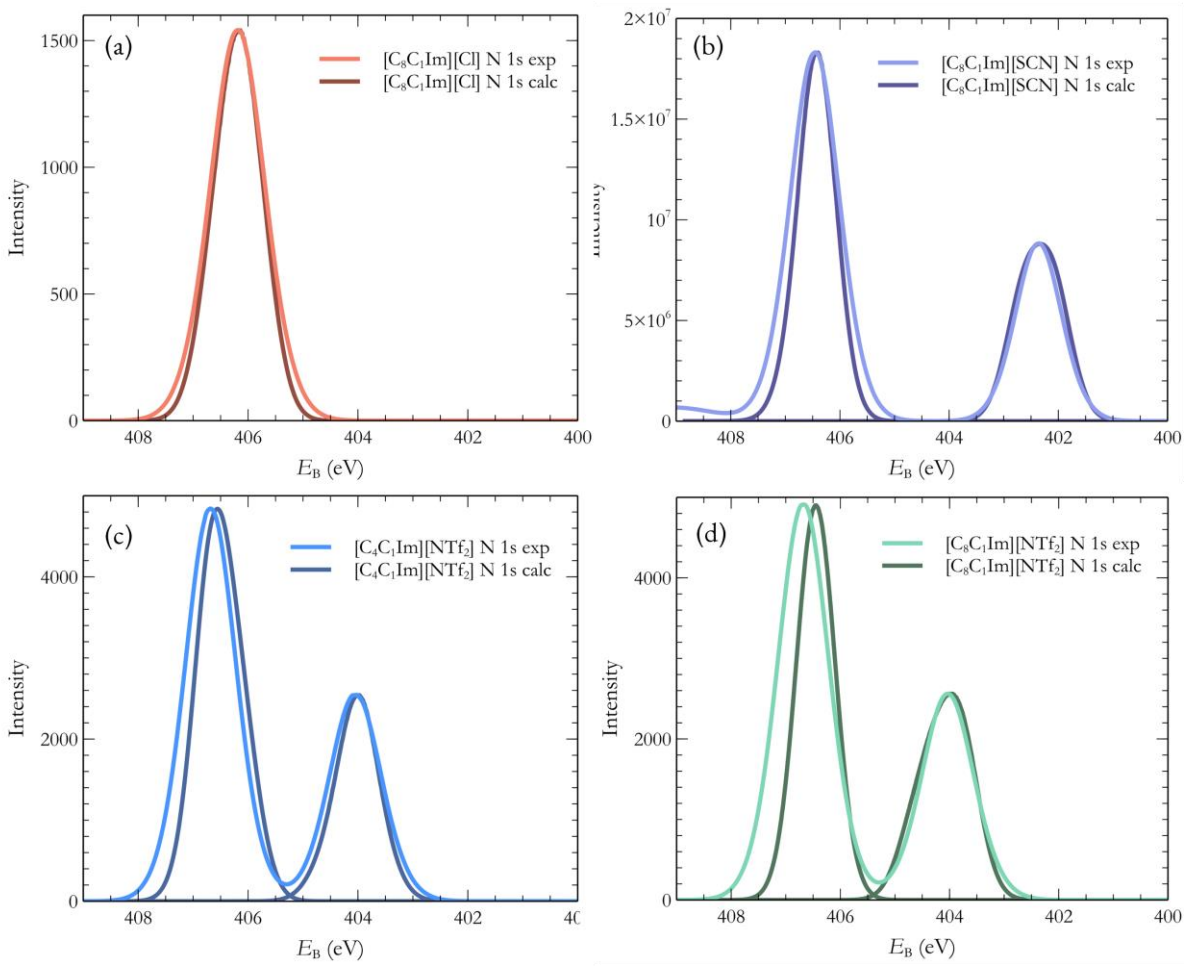

Figure 5.4 Plots of N 1s experimental high-resolution XP spectra vs calculated XP spectra. N 1s anion and cation calculated peaks have been normalised separately. **(a)** $[C_8C_1Im]Cl$ **(b)** $[C_8C_1Im][SCN]$ (normalised by factor of 4 (N_{cat}), 4 (N_{an})) **(c)** $[C_4C_1Im][NTf_2]$ (normalised by factor of 111 (N_{cat}), 113 (N_{an})) **(d)** $[C_8C_1Im][NTf_2]$ (normalised by factor of 9 (N_{cat}), 137 (N_{an})).

Peak asymmetry of the calculated N_{anion} 1s peaks is noticeably varied. In Figure 5.4c, $[C_4C_1Im][NTf_2]$ the N_{anion} 1s peak shows low peak asymmetry, comparable to that of $[C_4C_1Im][SCN]$, found in the previous chapter. However, in the longer-chained variations $[C_8C_1Im][SCN]$ and $[C_8C_1Im][NTf_2]$, the N_{anion} 1s peak, a slightly greater peak asymmetry can be observed (Figure 5.4b,d).

The broadening in the calculated N_{anion} 1s peaks of $[C_8C_1Im][SCN]$ and $[C_8C_1Im][NTf_2]$ is higher than their 4 carbon chain counterparts. In particular, the difference is notable between $[C_4C_1Im][NTf_2]$ and $[C_8C_1Im][NTf_2]$. There is no broadening difference in the experimental peaks

between these ILs. In $[C_4C_1Im][NTf_2]$, the calculated N_{anion} 1s peak does not quite match the experimental as it is slightly less broad, while in $[C_8C_1Im][NTf_2]$ the calculated peak is slightly more broad than the experimental. Although a bulk simulation provides a range of data points to simulate the sample broadening, additional instrumental broadening must be compensated for in the calculated XPS peaks. An added instrumental width value of 0.7 eV was selected for $[C_4C_1Im][SCN]$ in Chapter 4, and this value was found to be a perfect match for the N_{anion} 1s peak, but the resultant overall width was significantly lower than the experimental data in the N_{cation} 1s peak. Across the range of ILs studied here, the width value of 0.7 eV seems to be a good compromise, matching the experimental $[C_8C_1Im]Cl$ N_{cation} 1s peak remarkably well.

While it is possible that these broadening differences can be attributed to the ionic structures and electronic behaviours, the magnitude of these differences seems relatively insignificant. Added to the lack of noticeable peak broadening differences in experimental results, this rationale leads to the conclusion that these peak broadening inconsistencies between the different ILs are most likely resulting from calculations.

The peak asymmetry could be simply due to an insufficient number of data points extracted from the calculation. In this case, adding data from more snapshots would produce a symmetrical peak over this range. Viscosity of the IL may also be an influence for the asymmetry in the calculated N_{anion} 1s peaks of $[C_8C_1Im][SCN]$ and $[C_8C_1Im][NTf_2]$. At 333 K, the viscosities are ~0.015 Pa•s[255, 256] and ~0.023 Pa•s of $[C_4C_1Im][NTf_2]$ and $[C_8C_1Im][NTf_2]$ respectively. A higher viscosity also leads to diminished ion mobility and a less homogeneous liquid structure. In an AIMD simulation, a liquid requires sufficient potential energy or time to equilibrate and become representative of the real system. A higher viscosity may be overcome by increased temperature or longer simulation time. The former is the ideal choice as it does not affect the computational cost of the calculation and is more likely to achieve an equilibrated structure by speeding up the movement of the ions. Finally, the choice of geometry extracted from the AIMD calculation, from which the E_B was calculated, may be the cause of the broadening and symmetry discrepancies between experiment and calculation. The same number step from the AIMD was extracted across all ILs, and the relative potential energy at that step was not considered.

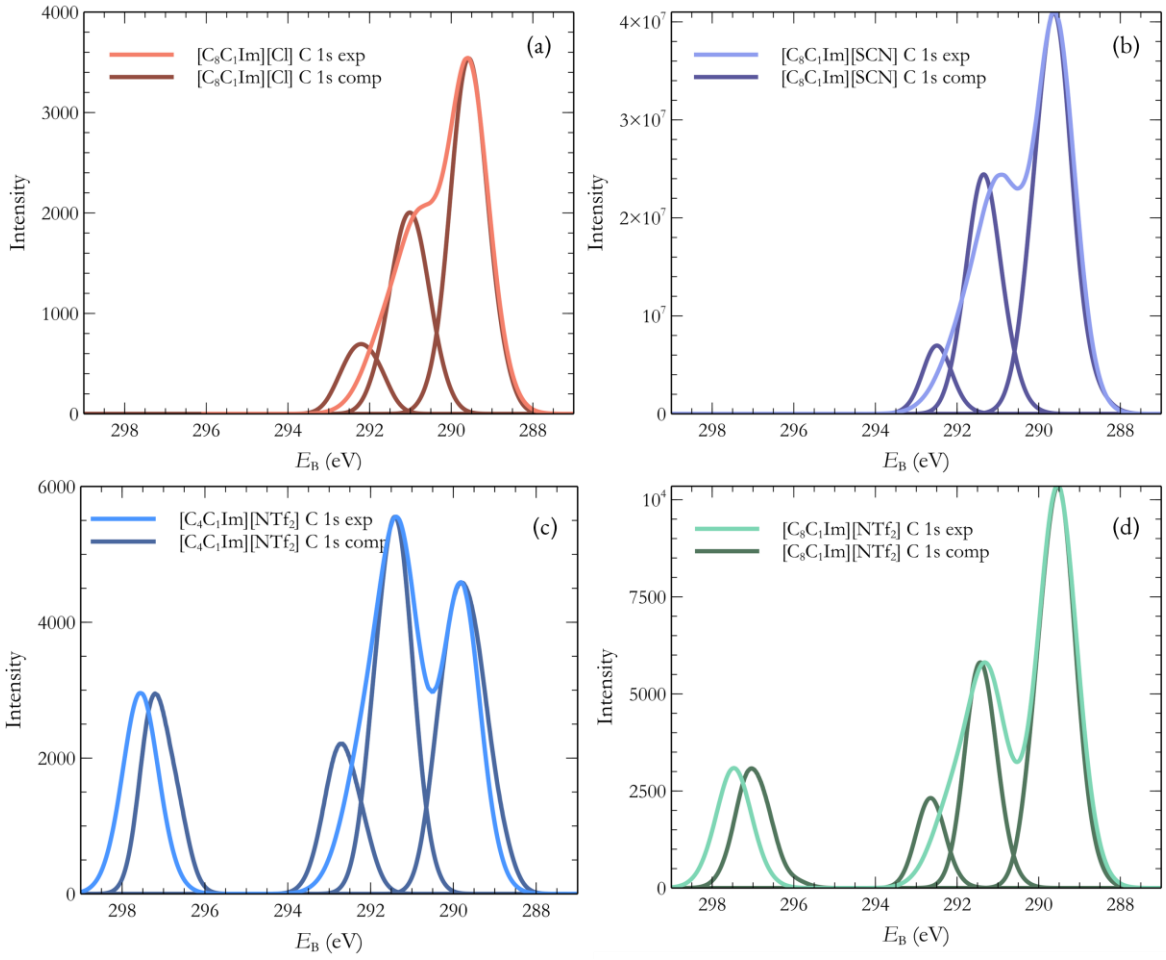

Figure 5.5 Plots of C 1s experimental high-resolution XP spectra vs calculated XP spectra. From highest E_B to lowest E_B, peaks are C^2, C_{hetero} and C_{alkyl}. C 1s calculated anion and cation peaks have been normalised separately. **(a)** $[C_8C_1Im]Cl$ **(b)** $[C_8C_1Im][SCN]$ (normalised by factor of 273648 (C^2), 294269 (C_{hetero}), 301138 (C_{alkyl})) **(c)** $[C_4C_1Im][NTf_2]$ (normalised by factor of 133 (C_{an}), 100 (C^2), 68 (C_{hetero}), 9 (C_{alkyl})) **(d)** $[C_8C_1Im][NTf_2]$ (normalised by factor of 145 (C_{an}), 90 (C^2), 62 (C_{hetero}), 74 (C_{alkyl}))

All C 1s calculated peaks (C_{alkyl}, C_{hetero} and C^2) were predicted to be in the correct order, with only small differences in E_B separations. For bulk liquid simulations of such complex systems, this is a great result. Comparison of the calculated C 1s peaks to the experimental data show reasonable fits, although across all of the ILs, E_B separations in the calculated C 1s peaks of the cation are consistently overestimated. In particular, the C^2 peak is calculated to be at higher E_B than the experimental. The percentage increase in calculated E_B separation relative to experimental separation of the peaks

$E_B(C_{alkyl}\ 1s)$ and $E_B(C^2\ 1s)$ ranges from 16 to 25%, the lowest for $[C_8C_1Im][NTf_2]$ (Figure 5.5d) and highest for $[C_8C_1Im][SCN]$ (Figure 5.5b). This finding could suggest the calculated $E_B(C_{cation}\ 1s)$ should be scaled for an improved match to experiment, and this approach has been taken with valence XPS.[206] Increasing the accuracy of the exchange-correlation functional in the calculations may also improve reproduction of the experimental peak separations.

The calculated C_{anion} peaks in ILs with the $[NTf_2]^-$ anion is at a lower E_B than experiment, resulting in a reduced separation between $E_B(C_{anion}\ 1s)$ and $E_B(C_{cation}\ 1s)$. It is difficult to deduce the possible cause for this slight discrepancy. Overall, the match from the initial, unperturbed core level energies to the experimental measurements is very good for both N 1s and C 1s high resolution spectra.

5.5.4. Anion effects

Once the accuracy of the calculated XPS results was validated against experiment, the calculated N 1s and C 1s core XPS spectra were assessed for E_B shifts with respect to changing anions. As there was only data for all three anions (Cl^-, $[SCN]^-$ and $[NTf_2]^-$), for the $[C_8C_1Im]^+$ ILs, only these were considered. All $[C_8C_1Im]^+$ ILs were referenced to the calculated C_{alkyl} 1s of $[C_8C_1Im][NTf_2]$, which was at 264.54 eV. The calculated data replicates the E_B pattern observed in experiment for both N 1s and C 1s core levels. The total shift from Cl^- to $[NTf_2]^-$ is 0.42 eV for N_{cation} 1s and 0.45 (±0.03) eV for C 1s. This is in excellent agreement with the experimental data, which exhibits a 0.40 (±0.04) eV shift (Figure 5.6).

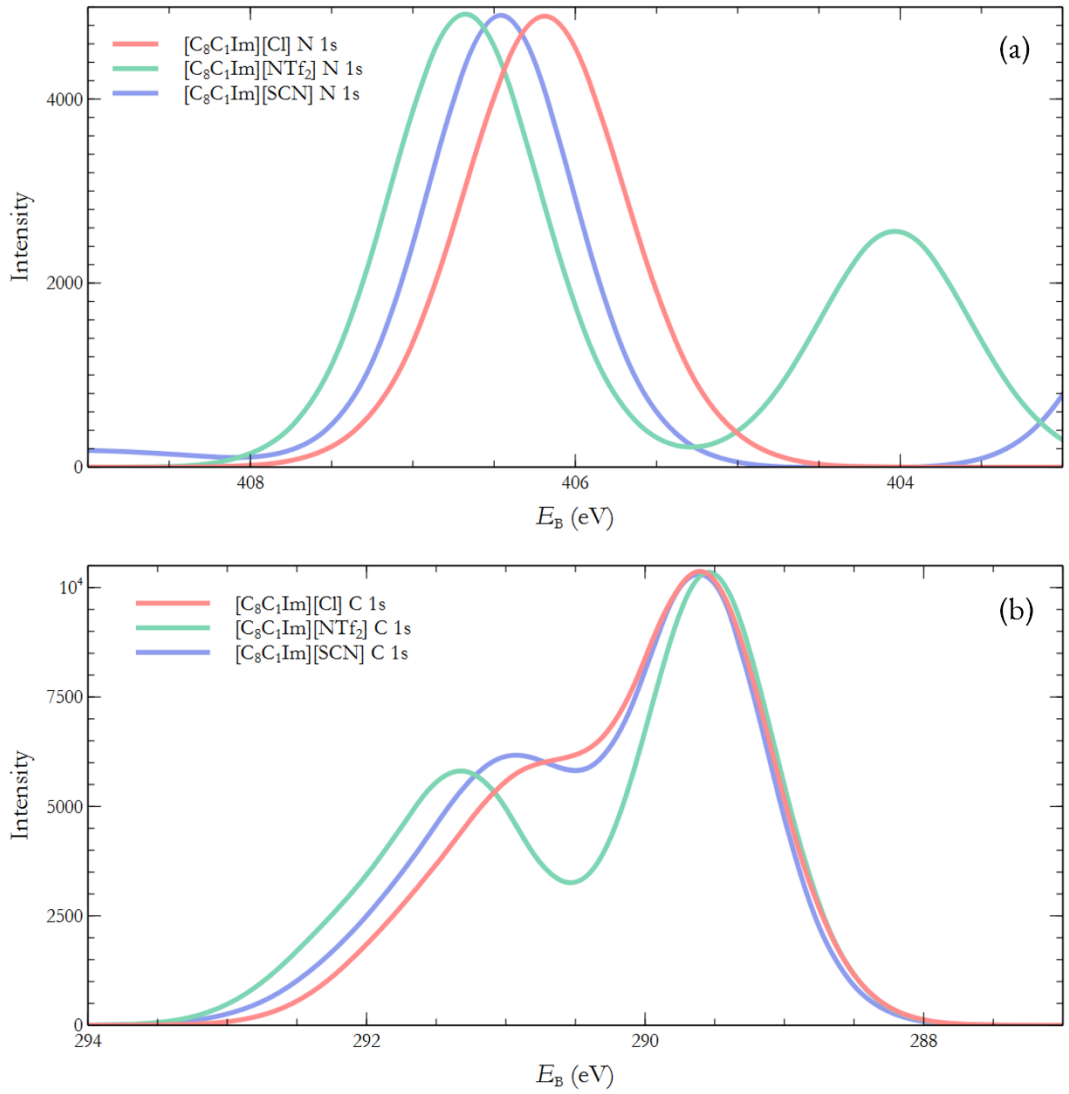

Figure 5.6 (a) Experimental high-resolution N 1s spectra, E_B scale cut for clarity. **(b)** Experimental high-resolution C 1s spectra, only showing the cation peak for clarity. From highest E_B to lowest E_B, components include C^2, C_{hetero} and C_{alkyl}. All peaks effectively referenced to vacuum, C_{alkyl} 1s at 289.58 eV.

Across the $[C_8C_1Im]^+$-based ILs, the N_{cation} 1s peak of the Cl^- is at the lowest E_B, followed by $[SCN]^-$ and $[NTf_2]^-$ anions at progressively higher E_B, respectively (Figure 5.7). This ordering of the E_B is consistent with experimental measurements. The smaller, more basic the anion, the lower the E_B peak. The stepwise E_B shifts from Cl^- to $[SCN]^-$ to $[NTf_2]$ are 0.021 (±0.05) eV . The largest anion-induced E_B shifts between the ILs are observed in the C^2 peaks. Overall, these results are very positive, confirming that these anion-dependent shifts in E_B are caused by IS effects, and thus validating previous literature which attributes this E_B shift to the ground state chemical behaviour.[36]

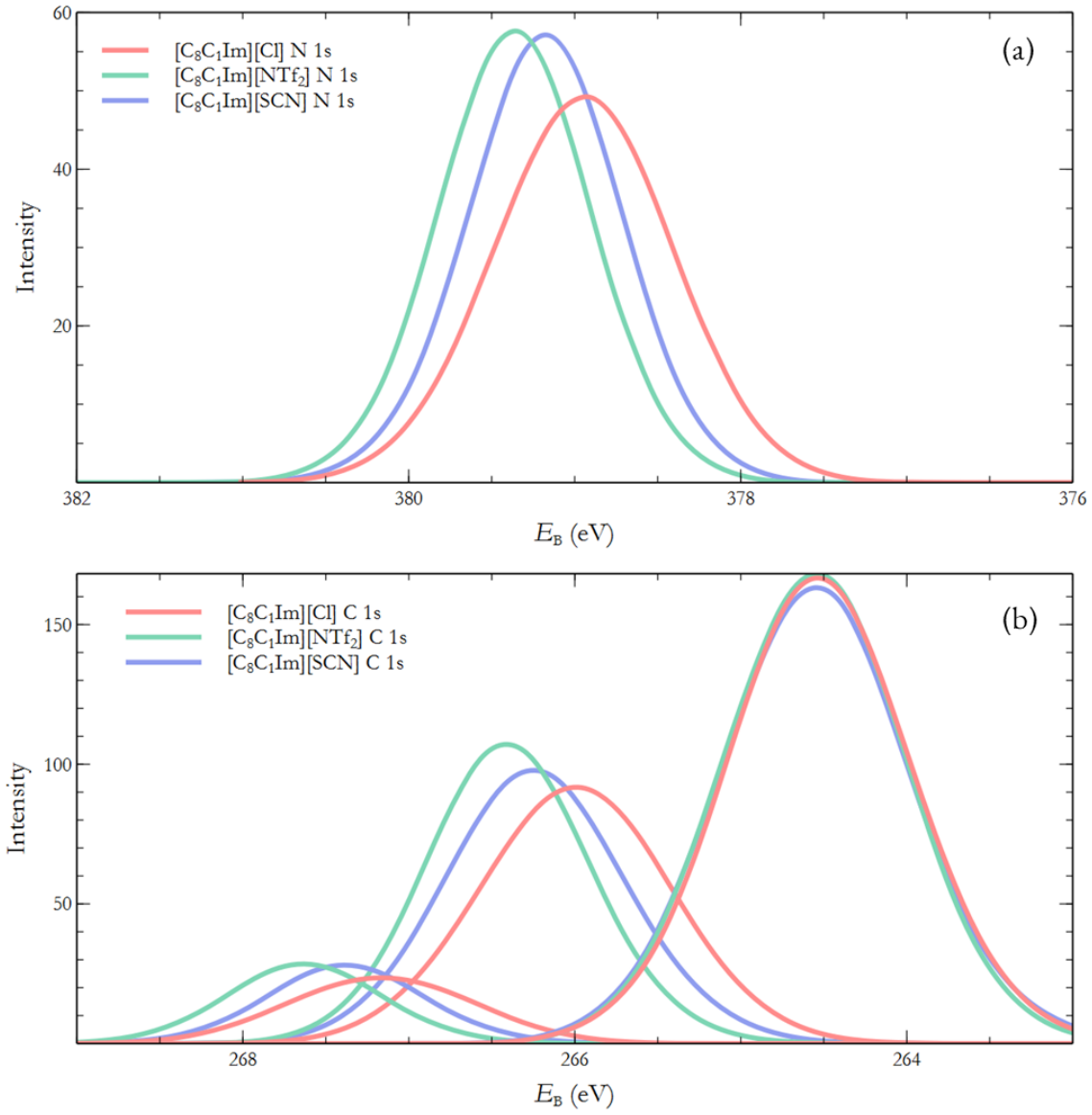

Figure 5.7 (a) Calculated high-resolution N 1s spectra, only showing the cation peak for clarity. Peaks broadened with a width of 1 eV to mimic experimental broadening. All peaks referenced to calculated C_{alkyl} 1s of $[C_8C_1Im][NTf_2]$, at 265.54 eV. **(b)** Calculated high-resolution C 1s spectra, only showing the cation peak for clarity. Peaks broadened with a width of 1 eV to mimic experimental broadening. All peaks referenced to calculated C_{alkyl} 1s of $[C_8C_1Im][NTf_2]$, at 265.54 eV. From highest E_B to lowest E_B, peaks are C^2, C_{hetero} and C_{alkyl}.

5.5.5. Cation chain length effects

As with temperature, discussed in Section 5.5.2, the change in the chain length of the alkyl functional group in the imidazolium-based cation ($[C_nC_1Im]^+$), from n = 4 to n = 8, was found to have no effect on the E_B peaks. Figure 5.7 demonstrates that there is no change in the N_{cation} 1s and N_{anion} 1s peak E_B separation between the experimental datasets of $[C_4C_1Im][SCN]$ *versus* $[C_8C_1Im][SCN]$ (Figure 5.8a) and $[C_4C_1Im][NTf_2]$ *versus* $[C_8C_1Im][NTf_2]$ (Figure 5.8b). The calculated data exhibits a small E_B shift in both comparisons of these ILs, but this shift is not considered to be significant.

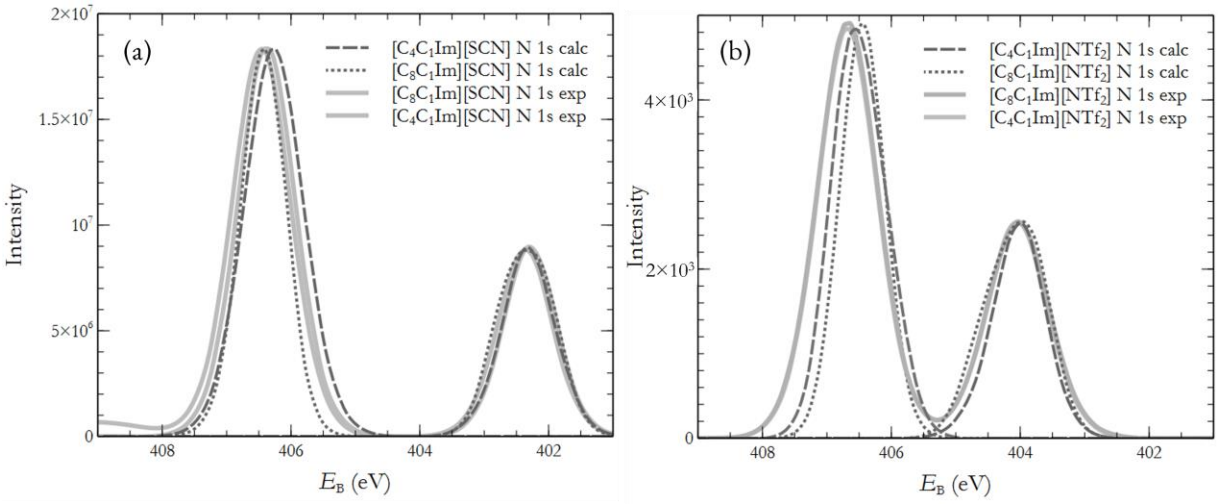

Figure 5.8 (a) Plotted experimental and calculated high-resolution N 1s peaks of $[C_4C_1Im][SCN]$ and $[C_8C_1Im][SCN]$. $[C_4C_1Im][SCN]$ intensity adjusted to match $[C_8C_1Im][SCN]$ intensity. **(b)** Plotted experimental and calculated high-resolution N 1s peaks of $[C_4C_1Im][NTf_2]$ and $[C_8C_1Im][NTf_2]$.

5.6. Conclusions

This work has further applied and evaluated the accuracy of a method developed to predict core XPS spectra in ILs using bulk phase simulations, first demonstrated in Chapter 4. This approach established that IS contributions are dominant in measured E_B for a total of 5 ILs: $[C_4C_1Im][SCN]$ (from Chapter 4), $[C_8C_1Im][SCN]$, $[C_4C_1Im][NTf_2]$, $[C_8C_1Im][NTf_2]$ and $[C_8C_1Im]Cl$. Research in the field XPS of ILs has been carried out under this assumption for many years, and these results validate the conclusions of a vast number of publications.

Experimental peak E_B and relative peak positions were replicated excellently by the calculations, even in atomic environments with very similar E_B, as with C_{cation} 1s. The C^2, C_{hetero} and C_{alkyl} peaks were calculated to be in the correct relative positions for all ILs investigated, with only small deviations in comparison to experimental E_B values. N_{cation} 1s and N_{anion} 1s peak E_B separations showed no difference between calculation and experiment for $[C_8C_1Im][SCN]$, and only minor differences in the other ILs, $[C_4C_1Im][NTf_2]$ and $[C_8C_1Im][NTf_2]$. High agreement was found between calculation and experiment in terms of peak broadness and symmetry.

The spread of E_B across the S 2p and Cl 2p core levels showed dependence on the anion of the IL. The IL $[C_8C_1Im]Cl$, with the small, basic anion Cl^-, had the largest range of E_B while $[C_8C_1Im][NTf_2]$ with the large $[NTf_2]^-$ anion has the narrowest range of E_B. Anion dependence of the core levels N 1s and C 1s was observed in the calculated data, following the experimental trend. The E_B shift from the lowest to the highest peak E_B ($[C_8C_1Im]Cl$ and $[C_8C_1Im]$ $[NTf_2]$, respectively) aligned remarkably well with the experimental E_B shift. The alkyl chain length in the cation $[C_nC_1Im]$ (where $n = 4$ and $n = 8$) was found to have no effect on E_B.

Temperature effects cannot be investigated experimentally. In simulations, a temperature difference of 100 K in the AIMD was found to have no effect on calculated E_B in any of the ILs studied. This result is favourable for the future of IL simulation using AIMD, as it enables the simulation of ILs with high viscosities at no additional computational power.

Some refinement of the method applied to predict core level XP spectra of ILs may be required in future work. The extraction of a larger set of data points to determine the calculation error would be a good first step to take before considering investigation of effects of the theory level.

6. Elucidating Geometric and Electronic Features of TiO_2-Ionic Liquid Interface

6.1. Abstract

The previous chapters have explored the fundamental behaviour of ionic liquids (ILs) using experimental and calculated core-level X-ray photoelectron spectroscopy (XPS) data. Moving one step closer towards application-based research, the following chapter investigates the IL-titanium dioxide (TiO_2) interface.

This work was conceptualised by EG, RGC, KRJL and RAB. The custom-built evaporator used in the experiments presented in this chapter was built by RAB and commissioned by RAB, EG and JMS. Experimental measurements were carried out on a collaborative beamtime with RAB, KRJL, DD, EG and JMS. The normal incidence X-ray standing wave (NIXSW) results presented in this chapter have been analysed and the related figures created by RAB. These results have been included in this chapter alongside the computational work to compare accuracy of the calculations and to build a complete picture of the geometric structure of the ionic liquids on the rutile (110) TiO_2 surface. The discussion related to this data and these figures was written by EG with guidance from RAB. All other figures created and data analysis carried out by EG. All calculations carried out by EG, with guidance in procedure from RGC.

6.2. Introduction

ILs have shown incredible potential in the field of electrochemistry and energy applications.[76, 257-266] A search in Web of Science using the terms "*energy*" and "*ionic liquid*" demonstrates the vast interest on this topic, with over 1,000 related publications annually since 2014. The characteristics that ILs exhibit which make them well-suited in this area include wide electrochemical windows, chemical and thermodynamic stability, and low vapour pressure. Implementation of ILs as a replacement for organic solvents can improve safety and stability in these devices.[267, 268] In energy applications, ILs form an interface with a material, often a semiconductor. ILs have been investigated at interfaces with an extensive list of surfaces, including lithium oxide[49], aluminium[56], graphene[54, 263], as a few examples. The semiconductor TiO_2 is the most widely studied metal oxide due to its diverse range of properties. TiO_2 is cheap, readily available, environmentally friendly and has high stability and safety.[269] Efficient photocatalytic behaviour and excellent electronic properties have led to TiO_2 being widely applied in energy conversion and storage research efforts.[270-273] Of the TiO_2 crystal structures, rutile (Figure 6.1) is the most thermodynamically stable and commonly studied, particularly the 110 surface.[61, 274]

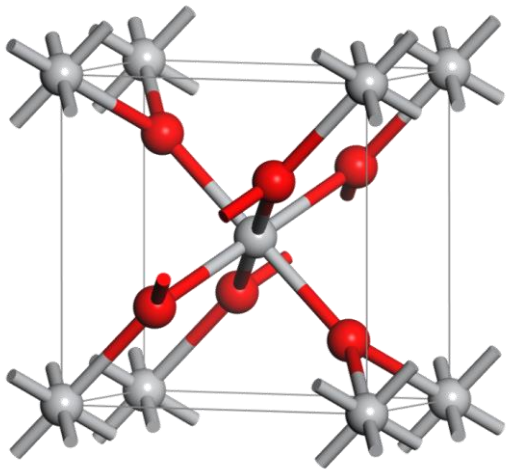

Figure 6.1 Visualisation of the rutile bulk unit cell.

Fundamental study of the electronic and geometric behaviours of the IL in the presence of a surface is necessary to guide further semiconductor-electrolyte design for improvements in electron transfer rates and overall device stability, longevity, and safety. X-ray photoelectron spectroscopy is a widely used technique to measure the binding energies (E_B) of core and valence levels. The core level XPS technique works particularly well with ILs, due to the negligible vapour pressure and their well-defined core level peaks. Core level E_B shifts are caused by changes to the valence electron structure, which reacts to the atom's surrounding environment. Normal incidence X-ray standing wavefields (NIXSW) allow access to buried interfaces, producing spatial probabilities of atoms above the surface. The density functional theory (DFT) computational approach models electrons explicitly, thus being the natural choice for simulating core levels and attaining geometry predictions with good accuracy.

Despite the interest of ILs in energy-based applications, fundamental experimental, computational, or combined studies of ILs on a TiO_2 surface are limited to-date. The IL 1-ethyl-3-methyl-imidazolium bromide, $[C_2C_1Im]Br$, has been studied on the rutile (110, 001) and anatase (100, 001) surfaces.[275] The IL 1-ethyl-3-methyl-imidazolium thiocyanate, $[C_2C_1Im][SCN]$, has been studied in bulk form using AIMD[216], on graphene[276] and on the anatase (101) surface with DFT methods.[277] 1-butyl-3-methyl-imidazolium thiocyanate, $[C_4C_1Im][SCN]$, has been studied using AIMD and DFT in bulk form (Chapter 4).[83] As far as we are aware, neither $[C_2C_1Im][SCN]$ nor $[C_4C_1Im][SCN]$ have been studied theoretically on the rutile (110) surface. To the best of our knowledge, the NIXSW technique has never been applied to the investigation of ILs. Only one study has carried out a monolayer-scale characterisation of an IL-semiconductor interface.[278] The IL 1-ethyl-3-methylimidazolium bis(trifluoromethylsulfonyl)imide, $[C_2C_1Im][NTf_2]$, was applied monolayer by monolayer to a selection of semiconductors and explored systematically using XPS and ultraviolet photoelectron spectroscopy (UPS). TiO_2 was not one of the semiconductors investigated.

In this chapter, $[C_4C_1Im][SCN]$ and rutile (110) interface is characterised by vacuum deposition of an IL monolayer and a combination of XPS, NIXSW and theoretical techniques. Computationally, interfaces were modelled at multiple scales to complement the experimental data. Two ILs, $[C_2C_1Im][SCN]$ and $[C_4C_1Im][SCN]$ were modelled to further compare the effect of the cation in

qualitative analysis. Investigation of the geometric features demonstrates excellent agreement between NIXSW and calculated results.

6.3. Computational methods

Structural models

Four 'scales' of IL on the TiO_2 surface were investigated: single ions, ion pair, monolayer and bulk. The IL $[C_2C_1Im][SCN]$ was modelled as single ions ($[C_2C_1Im]^+$, $[SCN]^-$) and as bulk IL (34 pairs) on the rutile surface. $[C_4C_1Im][SCN]$ was modelled as a single ion pair, a monolayer (four cations, four anions) and as bulk IL (32 ion pairs) (Table 6.1).

The bulk $[C_2C_1Im][SCN]$ was packed at a density of 1.18 g cm^{-3} [279] before combining with a TiO_2 slab to form a model sized 20.7 Å × 19.5 Å × 36.5 Å. The geometry of $[C_4C_1Im][SCN]$ was taken from the AIMD calculation presented in Chapter 4, before combining with the TiO_2 slab to create a box sized 20.7 Å × 19.5 Å × 40 Å. Both models created a structure where the IL is situated between two rutile (110) surfaces, producing a total of six interfaces: four of $[C_4C_1Im][SCN]$ and two of $[C_2C_1Im][SCN]$. The approximate thickness of the IL layers was 25.5 Å and 23.5 Å respectively.

Table 6.1 Tabulated representation of calculations carried out, including the number of configurations calculated and type of calculation carried out for each 'scale' of calculation.

	Model	No. of configurations	Geometry Optimisation	AIMD
$[C_2C_1Im][SCN]$	Single $[SCN]^-$	3	✓	
	Single $[C_2C_1Im]^+$	4	✓	
	Bulk (34 pairs)	1		✓
	Ion pair	6	✓	✓
$[C_4C_1Im][SCN]$	Monolayer (4 pairs)	1		✓
	Bulk (32 pairs)	2		✓

Geometry optimisations

Cell optimisation was carried out on a supercell of 4 × 4 × 6 of bulk TiO_2 rutile. Optimised bulk unit cell parameters $a = b = 4.67$ Å and $c = 2.97$ Å were in good agreement with experimental parameters, $a = b = 4.58$ Å and $c = 2.95$ Å.[61, 280] The TiO_2 slab model was constructed as a 7 × 3 × 1 supercell of the unit cell resulting from cleaving the rutile bulk unit cell at the 110 surface. For AIMD calculations, the zero-Kelvin-optimised cell parameters were expanded according to the reported experimental thermal expansion of rutile TiO_2 from 0 K to 300 K.[281]

Geometry optimisations of the single ion, single ion pair and bulk scale models were carried out in the CP2K code, using the QuickStep method. The FULL-ALL preconditioner was chosen with the conjugate gradients (CG) minimiser and the Broyden, Fletcher, Goldfarb, and Shanno (BFGS) optimiser. The PBE functional with Grimme-D3 dispersion corrections was employed with 5 multi-grids, a planewave cut-off of 1100 Ry and relative cut-off of 70 Ry.

For single ions, optimisations were carried out on single ion only (with charge compensation) and single ion with proton at a minimum distance of 13.00 Å (for charge neutralisation).

Molecular dynamics

Bulk $[C_2C_1Im][SCN]$ and $[C_4C_1Im][SCN]$ models were optimised for 25 steps in CP2K, using the same settings mentioned in geometry optimisation section. After a further pre-equilibration run

with the classical Dreiding force field in the canonical ensemble, a 20 ps production AIMD run was carried out in CP2K, using the Quickstep code and Gaussian and plane waves method (GPW), with the direct inversion in iterative subspace (DIIS) technique. The simulations were run at 298 K using the Nosé thermostat in the NVT ensemble. The PBE functional was used with DFT-D3 corrections by Grimme. A single run was carried out for $[C_2C_1Im][SCN]$ and two runs from different starting geometries were calculated for $[C_4C_1Im][SCN]$.

6.4. Experimental methods

Sample preparation

Approximately a monolayer of $[C_4C_1Im][SCN]$ was applied to the TiO_2 surface by vapour deposition at 140 °C using a custom-built organic evaporator.

X-ray Photoelectron Spectroscopy

Hard XPS was carried out at Diamond Light Source (UK) at the I09 beam line. A VG Scienta EW4000 HAXPES analyser was used, which had an angular acceptance of ±30°. The analyser was mounted with its centre approximately 80° (incident soft X-ray light) and 85° (incident hard X-ray light) away from the direction of the incident X-ray light (with respect to the sample) in the plane of the photon polarisation (linear horizontal); the analyser slits (and thus the angular acceptance direction) were also in the plane of the photon polarisation. The pass energy was 70 eV for the survey scan and 50 eV for the core level spectra.

Normal incidence X-ray Standing Waves

Normal incidence X-ray standing wave (NIXSW) data were collected at Diamond Light Source I09 beam line.[282] NIXSW was employed through five Bragg reflections from the rutile substrate to image the adsorbate positions. The crystal was aligned so that the X-ray beam was near normal incidence to a (*hkl*) Bragg reflection of the crystal. The beam energy was tuned through the Bragg energy and photoemission recorded, with multiple repeats in different spots across the crystal. As the beam

passes through the Bragg condition the phase of the standing wavefield changes allowing the high field regions to move spatially in a controlled manner. Thus the X-ray standing wavefield was swept through the adsorbates, selectively illuminating atoms depending on position. The X-ray reflectivity and photoemission response was fitted to give both the coherent position, P_{hkl}, and the coherent fraction f_{hkl}, for each scattering plane, element (or species if resolvable in photoelectron spectra). NIXSW was performed at the (220), (200), (1$\bar{1}$1), (101) and (121) Bragg planes to allow the atomic positions to be triangulated. By consideration of symmetrically equivalent planes (13 for most species, 9 for S), a volume probability density for a species could be defined. XPS core level shifts were utilised to discriminate between anionic and cationic species for the same element. *e.g.* N_{cation} 1s and N_{anion} 1s. The (101) reflection is at too low an energy to excite the S1s, so this species has significantly fewer reflections in the triangulation.

6.5. Results and discussion

6.5.1. Normal Incidence X-ray Standing Waves

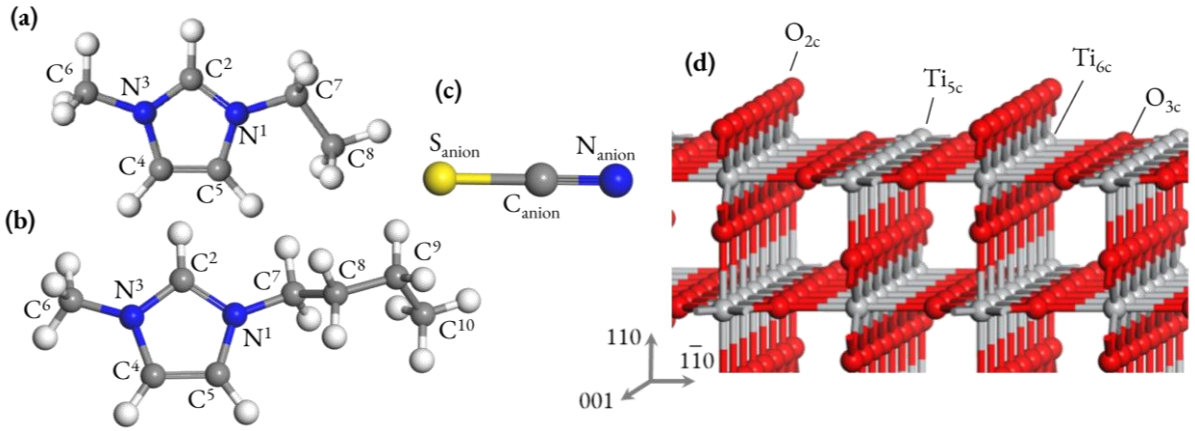

Figure 6.2 Labelling of all components of the ionic liquids, **(a)** $[C_2C_1Im]^+$, **(b)** $[C_4C_1Im]^+$, **(c)** $[SCN]^-$, and **(d)** rutile (110) surface, that are included in discussion. Hydrogens of the cations are named according to the carbon they are bonded to, *i.e.* H^2, H^4, H^5, *etc.*.

The NIXSW results were analysed to determine the most probable positions of N_{anion} and S_{anion} atoms on the rutile surface.[283] The labelling of the IL and TiO_2 atoms can be found in Figure 6.2. The initial finding was that the certainty of the N_{anion} positioning on the surface is much higher than that of S_{anion} atoms. The probability scale of the N_{anion} ranges from 0 to 22 (Figure 6.3), while the scale for the S_{anion} positioning ranges from 0 to 6 (Figure 6.4), indicating that the certainty of the N_{anion} positions is ~5 times higher than that of the S_{anion} positions. The N_{anion} positioning was found to be significantly more ordered than the S_{anion} atoms. The S_{anion} atom maps (Figure 6.4) depict far larger areas with similar probabilities, while the areas of high probability on the N_{anion} map are localised (Figure 6.3). This finding may be indicative of disorder or translational vibrations of the S_{anion} atoms, while the N_{anion} remain adsorbed in one position.

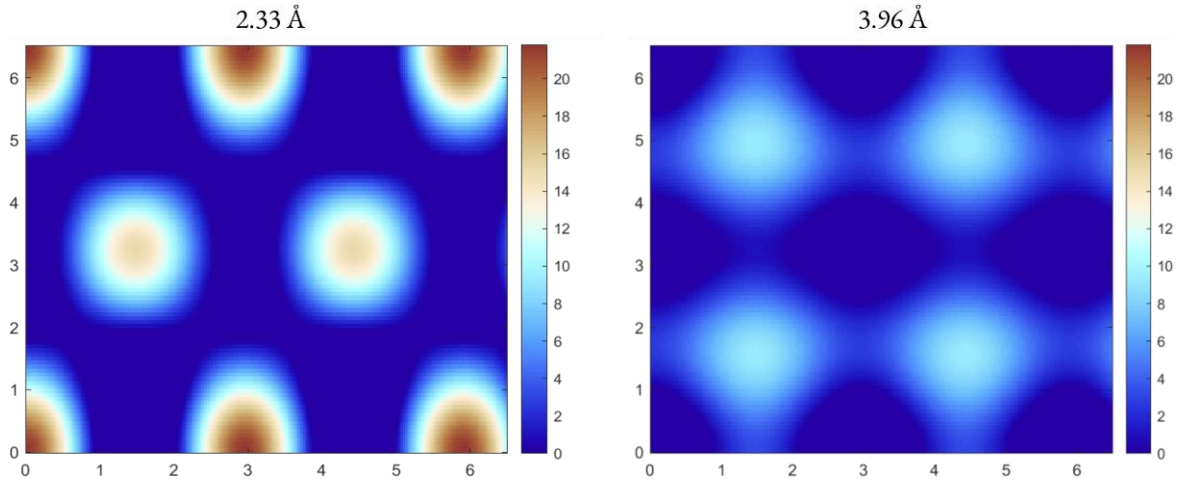

Figure 6.3 Heat maps of likely positions of the N_{anion} at fixed Z. **Left** is the highest probability arrangement, at a distance of 2.33 Å from the TiO_2 surface, with the highest probability of ~22. **Right** is the next most likely arrangement of N_{anion} at a height of 3.96 Å from the surface, although this probability is much lower, only reaching a value of ~11.

In terms of positioning on the surface, the N_{anion} atoms were found to predominantly lie directly above the Ti_{5c} centres, with a lower probability of interacting above Ti_{6c} positions (Figure 6.5). Figure 6.3 indicates that the Ti_{5c} - N_{anion} bond lengths can be estimated to be ~2.33 Å in length. The second most likely arrangement, at 3.96 Å from the surface, is too far removed from the surface to

be considered a bond, but some interaction is likely happening between the N_{anion} and the surface, as the order remains high, especially in comparison to S_{anion}, despite the overall lower probability of finding N_{anion} in these positions at this distance.

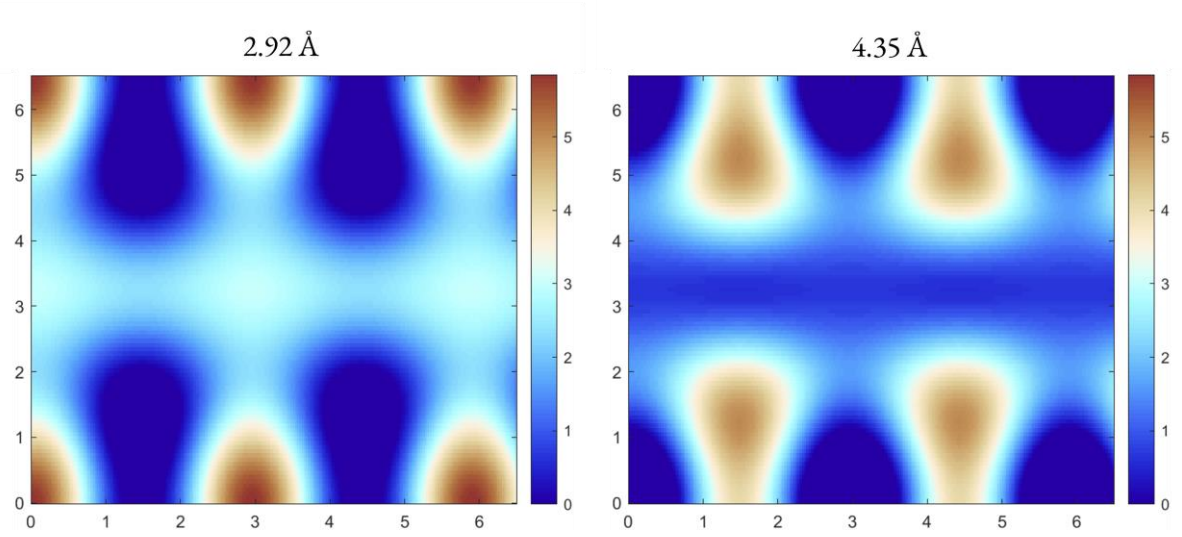

Figure 6.4 Heat maps of likely positions of S_{anion} atoms at fixed Z. **Left** is the highest probability arrangement, at a distance of 2.92 Å from the rutile (110) surface, with the highest probability of ~6. **Right** is the next most likely arrangement of S_{anion} at a distance of 4.35 Å from the surface. This probability is only slightly lower, with a value of ~5.

The highest probability distribution of S_{anion} atoms indicates that the atoms may also be adsorbed at the Ti_{5c} sites, with a probability of ~6, or interacting with the O_{2c}, with a probability closer to ~3 (Figure 6.5). The Ti_{5c} - S_{anion} bond length is estimated at ~2.92 Å. This arrangement (Figure 6.4, left) is only slightly more likely than the second arrangement extracted from analysis (Figure 6.4, right) at 4.35 Å. Due to adsorption on a terrace, this latter geometry also has an equivalent one surface step up or down, which is ½(110) in height or 1.1 Å, not included here. Together, the probability maps in Figures 6.3 and 6.4 suggest the S_{anion} atoms interact with the surface in a more fluid manner, at various heights and positions, while the N_{anion} atoms seem to be adsorbed more strongly on the surface, in an ordered manner, the majority above the Ti_{5c} centres. These results could be interpreted as an indication of the anion $[SCN]^-$ preferentially adsorbing on the surface in N-down or flat orientation (similar to geometries A1 and A3 respectively, illustrated in Figure 6.6). The map at a 1.1 Å distance from the surface may be indicative of a flat or possibly S-down orientation. The N-down

geometry seems likely to be the dominant adsorption geometry of the IL monolayer, as this would account for the localised nature of the N_{anion} positioning and also provide the S_{anion} atoms the freedom for translational vibration at the distances of the higher probability maps, 2.92 Å and 4.35 Å.

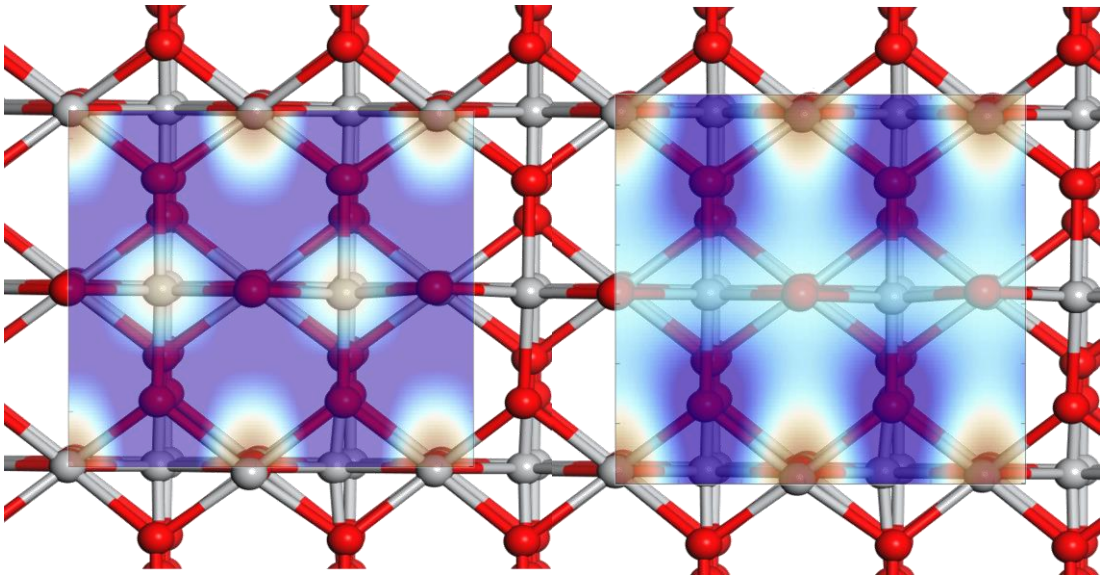

Figure 6.5 Highest probability heat maps of N_{anion} (left) and S (right) atoms from Figure 6.2 and 6.3 overlayed with the rutile slab geometry.

6.5.2. Geometry Optimisations

In all the geometry optimisations, the anion $[SCN]^-$ adsorbed onto the surface directly above Ti_{5c} sites. In the anion-only models, all three starting configurations optimised to the N-down orientation with a N_{anion} -Ti_{5c} bond length of 1.90 Å. In ion pair calculations, three of six (P2a, P2b, P3a, illustrated in Figure 6.7) starting geometries optimised with the anion $[SCN]^-$ in the N-down configuration. In these, the N_{anion} -Ti_{5c} bond lengths were slightly longer, from 1.92 Å to 1.94 Å. The remaining three starting configurations optimised with the anion in the S-down orientation, P1a, P1b and P3b (Figure 6.7). Inspection of the ion pair optimised geometries shows that these S-down orientated anions exhibit a strong interaction with the cation, seemingly by hydrogen bonds with the N_{anion}. These interactions occur from the N_{anion} to the H^2 and H^6 (P1b and P3b, Figure 6.8,

labelling of hydrogens explained in Figure 6.2) or the H^4 (P1a). Hydrogen bonds between the cation and the anion in imidazolium ILs have been well studied and characterised in existing literature, and ion-pair computational models have confirmed their formation.[34, 241, 284-290] The optimised S-down orientated models also exhibit a flatter orientation of the SCN anion than in the N-down orientated models, in which the S_{anion} is only interacting weakly (≥ 3.36 Å distance between anion and cation), or not at all, with the cation. Energetically, the three optimised N-down models are degenerate, and the three optimised S-down models are 0.53 to 0.63 eV higher in total potential energy of the system.

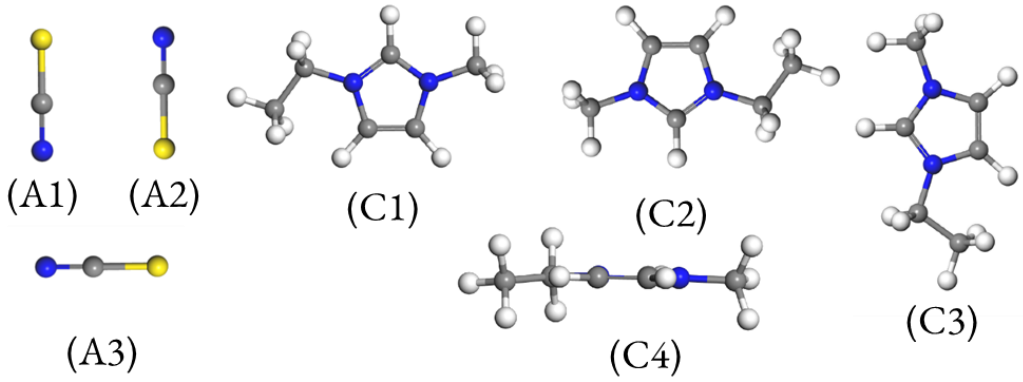

Figure 6.6 Starting geometries, labelled with nomenclature used in this work, of the single ion geometry optimisation calculations. The TiO_2 surface would be below the ion. Ions were set 3.5 Å away from the surface. A*n* refers to anion and C*n* refers to cation, where *n* is the configuration number.

In all geometry optimisation calculations, it was found that the Ti_{5c} protrudes between 0.53 to 0.63 Å from the rutile (110) surface, in comparison to the non-interacting or non-coordinating Ti_{5c}. The lower end of this range is seen in the ion pair models, while the higher end in the anion only models. This finding may suggest that the extent of Ti protrusion from the surface is indicative of the strength of the ion-surface interaction, in response to the cation-anion interaction or lack thereof. In the ion pair models, a stronger cation-anion interaction may cause a reduced coordination strength of the N_{anion} – Ti_{5c} interactions, and the Ti_{5c} atom is not 'pulled' out of the surface to the same extent.

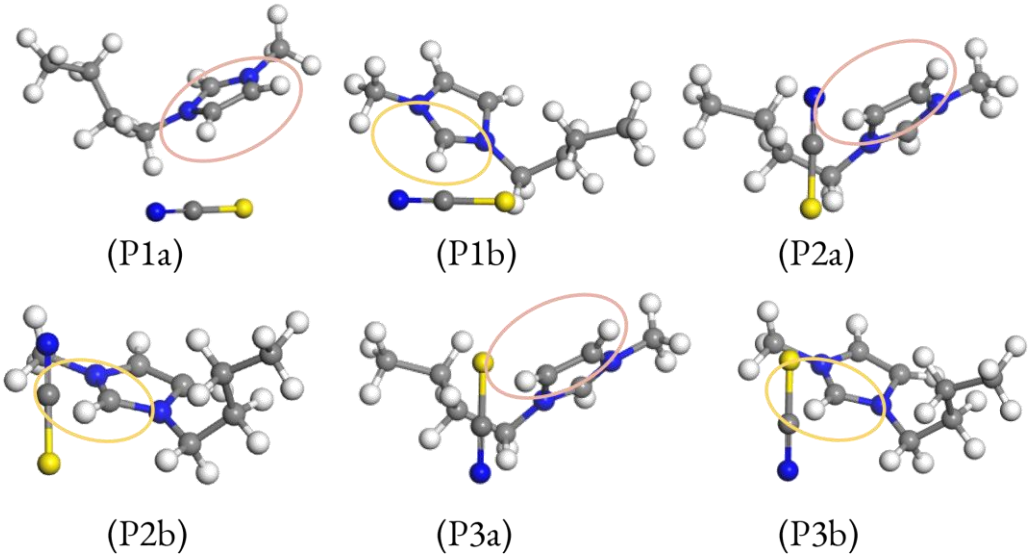

Figure 6.7 Starting geometries of the ion pair geometry optimisation calculations, assuming the surface is below the ion pairs. Ions were set 3.5 Å away from the surface. Pink circles highlight the C_{hetero} ring atoms facing the anion (P*n***a**), yellow circles denote C^2 facing the anion (P*n***b**). P denotes ion pair.

The influence of the cation-anion interaction strength on the coordination strength of the anion to the Ti_{5c} is also supported by the starting geometry P3b optimising in the S-down orientation. It seems that the inter-ion interaction N_{anion}–H^2 is sufficiently strong to prevent the anion from flipping, as it does from starting configuration P3a, and this overrides orientation to the preferred N-down coordination geometry. Configuration P1b, where the anion is interacting with the C^2 carbon of the cation, has the least protruding Ti_{5c} atom of all the models.

These geometry optimisation results align with the existing literature of calculated single-ion models on the anatase (101) surface, which has shown both N-down and flat orientations as the lowest-energy or preferred geometries in both classical and *ab initio* calculations[277, 291]. In this existing literature, anions in the S-down orientation were also observed in classical MD simulations, but these were far less abundant.[291] These classical simulations also further demonstrated that the Ti_{5c} is the preferred interaction site for both N_{anion} and S atoms in the $[SCN]^-$ anion and upon coordination with the anion atoms, the Ti_{5c} atom is found to rise away from the surface.

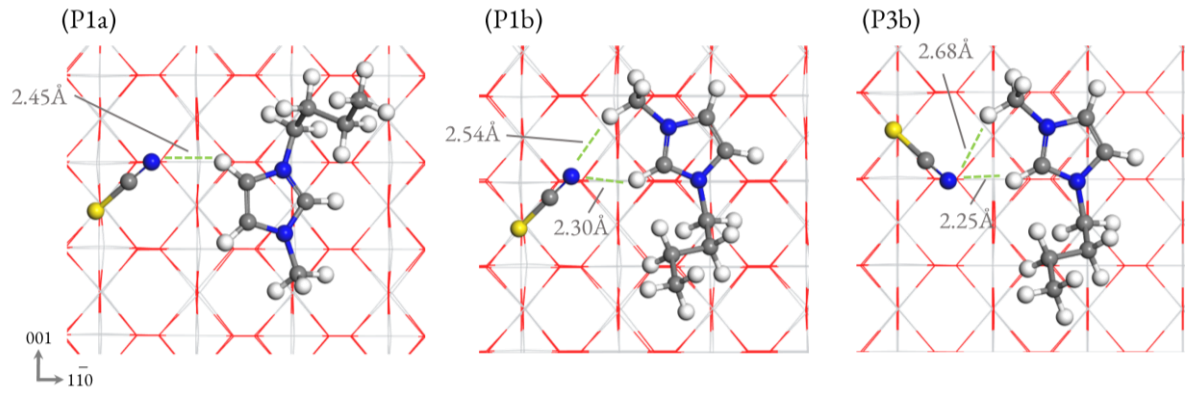

Figure 6.8 Geometries of all S-down anion optimised ion pair models. Potential hydrogen bonds are highlighted in green and lengths are labelled in grey.

In the optimised models with the anion in the N-down configuration, N_{anion} - Ti_{5c} bond lengths ranged from 1.90 to 1.94 Å, far shorter than the 2.33 Å estimated from the NIXSW experiments. The S-Ti_{5c} bonds are 2.44 to 2.47 Å, also shorter than the 2.92 Å estimate from experiment. Although these bond lengths are shorter than the measurement from NIXSW results, the prediction of N_{anion} - Ti_{5c} bonds being much shorter than the S - Ti_{5c} bonds is accurate, with a calculated difference of 0.54 to 0.57 Å between the two bond types, and a 0.59 Å difference in experiment.

Cation-only models relaxed into a range of orientations, from flat to perpendicular, with respect to surface. Orientation in relation to the surface was measured by maximum surface-ring angle θ (Figure 6.9), where $\theta = 180^{\circ}$ is perpendicular to surface and $\theta = 90^{\circ}$ is flat above surface. Energies were compared between all optimised configurations, and it was found that three of the four optimised geometries had angles $\theta = 104^{\circ}$ to 131°, all these were within an energy difference of 0.04 eV. Non-flat configurations were both arranged with the C^2 (and respective H) atom down. It is expected that H-C^2 would preferentially interact with the surface at O_{2c} sites, as the interactions would be characteristic of hydrogen bonds. The fourth and highest energy optimised configuration (from starting configuration C3) displayed $\theta = 169^{\circ}$, almost perpendicular to the surface. This geometry is 0.23 eV higher in energy than the lowest energy configuration. Optimised cation only models did not show any surface distortion.

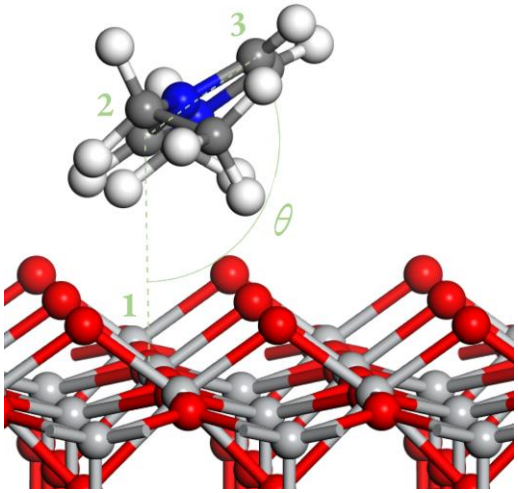

Figure 6.9 Optimised geometry of starting configuration C4 (Figure 6.6). Labelled angle θ, measured from 1 surface atom – 2 ring atom (a) – 3 ring atom (b). Ring atom (a) is whichever atom of the imidazolium ring is directly above the surface atom and ring atom (b) is the atom across from ring atom (a). This angle was measured in all optimised geometries and related to optimised energies. In this optimised configuration, θ = 123°. Lowest energy geometries, θ = 104° to 123°. Highest energy geometry, θ = 169°

6.5.3. Ab initio molecular dynamics

The 'flat' cation conformation continues to be the dominant adsorption geometry in the AIMD simulated ion-pair and monolayer models. The largest cation-surface angle exhibited in these models is only θ = 120° (Figure 6.10), despite raised simulation temperatures of 398 K, which may have caused the ions to exhibit higher-energy orientations. In the bulk models (34 ion pairs of $[C_2C_1Im][SCN]$ and 32 pairs of $[C_4C_1Im][SCN]$), however, the cation exhibits a larger range of geometries in relation to the surface. The 'flat' conformation is prevalent, but so are 'perpendicular' conformations.

In both ion pair and monolayer models, all the anions adsorb in the N-down configuration. With the introduction of more ion pairs, the monolayer model creates an environment where longer-range dispersion forces become more present. This may remove the strong (and potentially exaggerated) cation-anion interaction of the ion pair only models, as the monolayer exhibits only a single anion adsorption geometry (Figure 6.10). In bulk simulations, a variety of anion geometries appeared: the

majority in the N-down configuration, with a few in the S-down configuration and one anion in the flat configuration (Figure 6.11). The N_{anion} - Ti_{5c} bonds in all the AIMD models also cause the Ti_{5c} atoms to protrude from the surface, as seen in the geometry optimisations. Coordinating N_{anion} - Ti_{5c} protrude at a magnitude of 0.15 to 0.50 Å from the bulk surface.

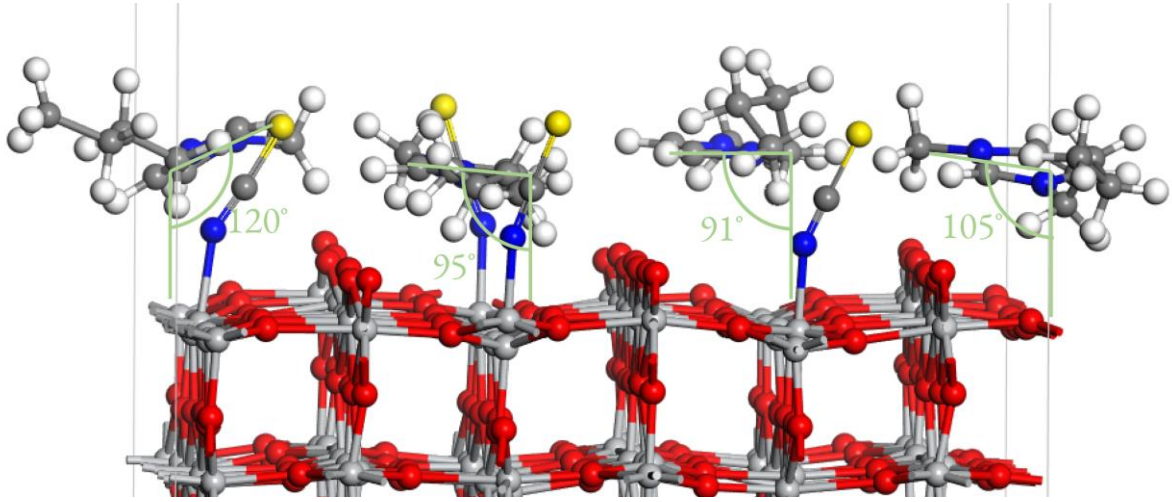

Figure 6.10 A single geometry from the monolayer (4 cation and 4 anion) pair model. In green, cation ring angles with respect to the TiO_2 surface are given.

In the AIMD models, bond lengths seem to be far closer to those estimated from the NIXSW experiments than in the ion pair geometry optimisations. This is expected, as the experiment is carried out around 298 K, more similar to the temperature at which the AIMD was simulated, compared to the 0 K temperature of the geometry optimisations. The N_{anion} - Ti_{5c} bond lengths range up to 2.15 Å, a lot closer to that of experimental predictions than seen in the geometry optimisations. S_{anion} - Ti_{5c} interaction distances are found to be up to 2.99Å, slightly longer than that of experiment. On average, both bond lengths are slightly longer in the bulk models than the monolayer model.

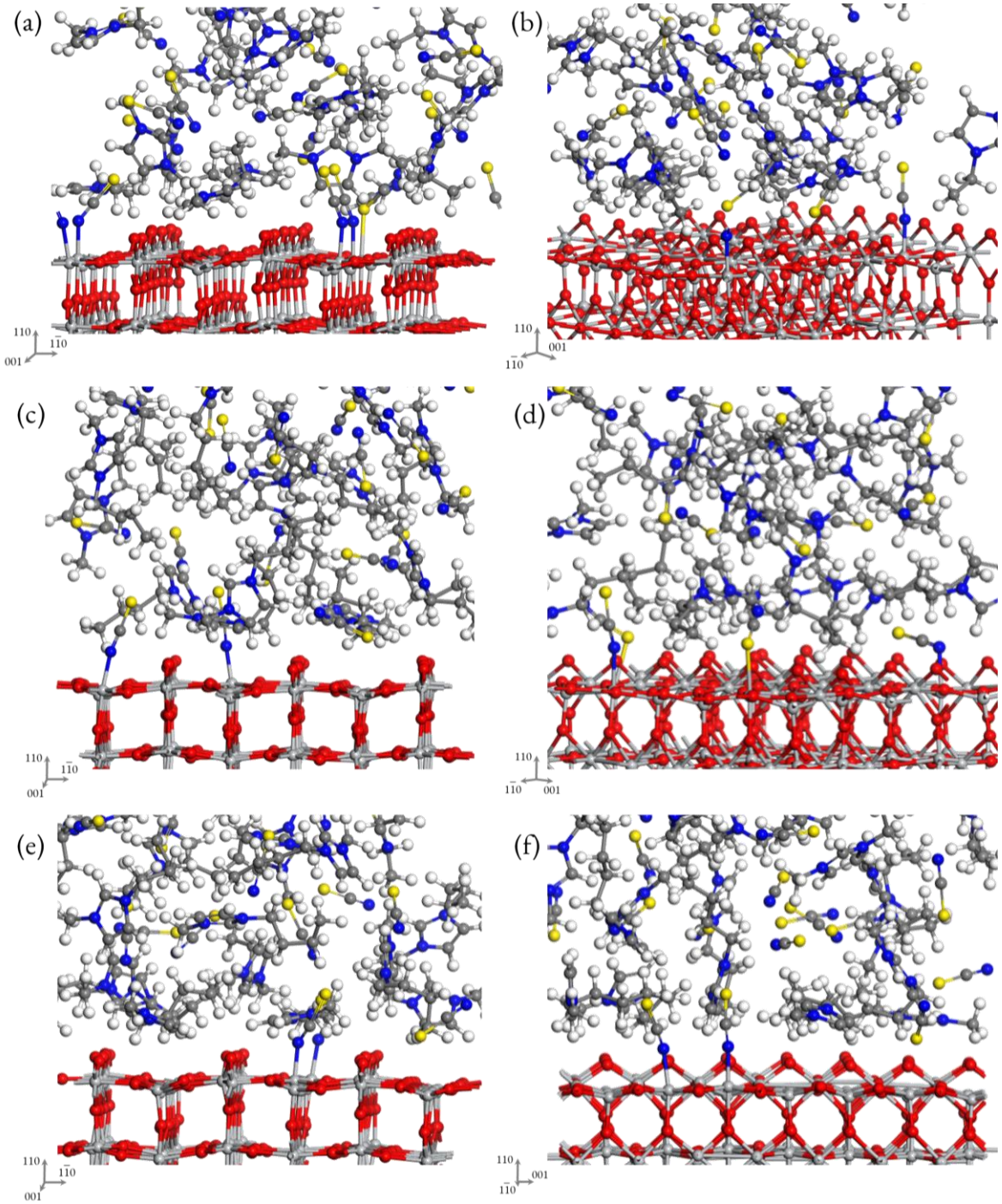

Figure 6.11 The last geometries of the surfaces of all bulk AIMD models, orientated for the best view of the anion adsorptions and interactions with the surface. Configurations **(a)** and **(b)** are surface 1 and 2 of $[C_2C_1Im][SCN]$ respectively, **(c)** and **(d)** show surface 1 and 2 of $[C_4C_1Im][SCN]$ (run 1), **(e)** and **(f)** depict surface 1 and 2 of $[C_4C_1Im][SCN]$ (run 2).

There are notable further differences in the surface composition between the monolayer and the bulk models of $[C_4C_1Im][SCN]$. In the monolayer models, all of the ions (4 cations, 4 anions) are adsorbed on the surface. Qualitative analysis shows only three anions are adsorbed per surface, on average (of four surfaces in total), in the bulk models. This creates a cation-rich environment in the interfacial layer of the IL. The $[C_2C_1Im][SCN]$ IL has four and five anions adsorbed at the two surfaces, and it seems to be more balanced between cations and anions, although it is difficult to determine visually and would require further analysis to confirm.

6.5.4. X-ray photoelectron spectroscopy

Core-level high-resolution XPS N1s spectra of a monolayer of $[C_4C_1Im][SCN]$ on the rutile (110) surface showed a substantial change in N_{anion}–N_{cation} peak separation compared to bulk liquid measurements. In the IL bulk, this separation is measured consistently as 4.10 eV, while on the TiO_2 surface, it was measured as 2.00 eV (Figure 6.12).

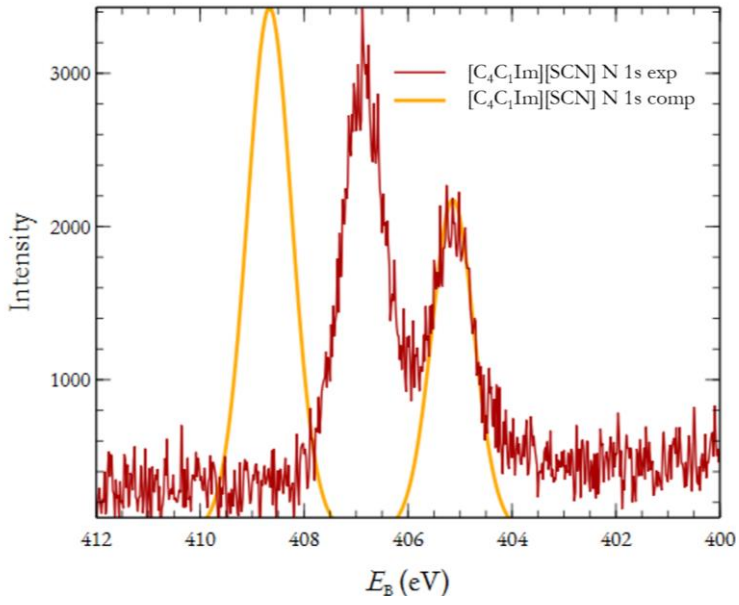

Figure 6.12 N 1s high resolution XP spectra of a $[C_4C_1Im][SCN]$ monolayer on the rutile (110) TiO_2 surface. Experimental raw data is displayed in red and calculated data is displayed in yellow. Intensity of the calculated data has been corrected for a good visual fit to the experimental data.

Considering the major differences in the strength of interactions between cation-TiO_2 compared to anion-TiO_2, it would be most reasonable to expect the N_{anion} 1s peak to be experiencing the majority of the E_B shift that contributes to this vast change in peak separations, rather than the N_{cation} 1s peak. As the SCN adsorbs to the electron deficient Ti_{5c}, the bonds created consist of a formal sharing of electrons, compared to the ambiguous network of IL interactions in the bulk form. Thus, it is expected that the N_{anion} 1s E_B would move to much higher values.

Calculated E_B in the initial state approximation (ground state effects only) on the monolayer model (4 cations, 4 anions) estimates the N_{anion}–N_{cation} peak separation as 3.34 eV. The discrepancy between experiment and the calculated IS approximation is very significant. Based on these results, the IS approximation may not describe the electronic behaviour as accurately at a semiconductor surface as it does in the bulk IL. Further calculations using the final state approximation (modelling of an electron being removed from the core level into vacuum) would clarify this. Another explanation for this deviation is limitations in the level of theory used to treat the TiO_2, and the improved electronic description using the DFT+U method may reflect in the E_B of the adsorbed ions.

6.6. Conclusions

This work has examined the interfacial behaviour of ILs with TiO_2 and found that experiment and simulation lead to similar conclusions in terms of the interface geometry. The benchmarking of the calculation by experiment allows the further exploration of calculated models (including the IL's bulk) that cannot be achieved in experiment. Calculated interaction distances were found in closer agreement with experiment in the AIMD method than in geometry optimisations at 0 K, which is not surprising as the former includes dynamic effects. This further demonstrates the accuracy (and the necessity) of AIMD in modelling ILs, presented in Chapters 4 and 5, on a very different type of system to the bulk liquid.

Surface composition was found to vary even by a difference of two carbons in the alkyl chain length of the $[C_nC_1Im]^+$ cation, from n = 2 to n = 4. A relatively cation-rich surface, when n = 4, would

have implications on the relative electronic behaviours of the materials, such as band structure of the TiO_2. This would require further calculations to confirm and assess any relationship between alkyl chain length and macroscopic parameters related to energy applications. While the results in Chapter 5 demonstrated that a changing cation with the same anion has no effect on E_B separations in the bulk IL, the effects of geometry and sterics could reveal significant changes to the electronic behaviour in the presence of the surface.

In core level XPS simulation, electronic behaviours were not replicated as successfully using the initial state approximation on the monolayer model, as they were in Chapters 4 and 5. N 1s peak separations deviated from the experiment by ~1.3 eV. This discrepancy could be attributed to final-state effects that the initial-state approximation used here does not account for, or this could be due to insufficient accuracy in the description of TiO_2 electronic behaviour. This method requires further refinement for interfacial structures, and the first steps to take would be to perform final-state calculations and calculate core XPS peaks for more configurations of the monolayer model, separated by reasonable time increments in the AIMD.

As the models grew in scale, from single ion models to ion pair to monolayer and to bulk, there were noticeable differences in preferred orientations, particularly of the anion, and the extent of disruption of the surface, by protrusion of the Ti_{5c} site upon adsorption. The adsorption strength between the IL and the surface was observed to depend on the strength of the cation-anion interactions, which were determined by the presence of other ions at the interface. Reduced cation-anion interactions, in turn led to more displacement of the Ti_{5c}. These subtle changes are likely to accumulate in real systems, and it would be interesting to build upon the experimental NIXSW study by increasing the number of monolayers and measuring the N 1s separation systematically to see if these results are significant in the real system.

7. Conclusions & Future work

7.1. Reflection and conclusions

In this thesis, a combined approach using experimental XPS and NIXSW techniques alongside computational simulations was developed and tested across a wide range of IL-based systems. This work presents a complete demonstration of a symbiotic relationship between experiment and theory; experimental data was used to benchmark calculation, and the validated calculation was further investigated to extract information otherwise unattainable through experiment alone. The selection of systems that were studied included five bulk ILs and two ILs on a rutile (110) TiO_2 surface.

Core level XPS spectra were simulated from bulk computational models of ILs for the first time. This approach offered a range of conformational distributions of E_B, a result of the complete range of interactions experienced by the bulk system. It is inherently impossible to describe these features to the same precision with gas phase ion pair calculations. The increased accuracy and detail of this approach has enabled us to meticulously compare the initial and the final states, and to assess broadening contributions from the sample *versus* the experiment. The results from this analysis have proven the long-held assumption that the initial state is dominant in XPS measured spectra. Following on from the initial development of this method, the process was carried out on five ILs in total. These liquids were selected representatives of a much wider range of ILs. This combined experimental and computational method continued to produce accurate core E_B calculations of these bulk systems across the range of core levels, anions, and cations. The component peaks were

consistently calculated to be in the correct relative positions and intensities. We can more confidently conclude that this simulation method can be applied to many more types of ILs with the same quality of results. This outcome has validated a wide array of previous publications in literature whose conclusions rely on a direct relationship between E_B shifts and the ground state system. Future work on bulk IL systems using the XPS method can be carried out with the confidence that E_B shifts originate from the ground state of the system. However, it is unclear from the presented calculated initial state core E_B data on the TiO_2 surface whether this result applies to ILs at interfaces, and the investigation of core E_B needs far more development to draw any reliable conclusions.

It has been noted that the research area of interfaces with ILs is colossal, particularly within the area of electrochemistry. Pairing the most studied metal oxide in materials science with one of the most common ILs, to investigate E_B shifts, was a step toward developing the area of fundamental research into this type of system. In the short-term, it may be considered more effective to directly measure properties such as conductivities or effects of the IL on the semiconductor band gap. It should be contemplated whether this approach may be a "shortcut" and offers a reduced payoff in the long term. Focusing on the fundamental electronic interactions, though a more tedious process, may have potential far exceeding the former approach. Combined with a computational atom-by-atom insight, continued work in this area would enable electronic measurements to be related to geometric and functional features of the ions. In time, a collection of this data can be related back to the macroscopic effects of these interacting materials and enable the evolution of a predictive technique for new ILs and surfaces. Though it was investigated in the context of electrochemistry for this work, the ability to make these predictions would benefit any application where solid meets IL.

As far as we are aware, this is the first NIXSW experiment presented to investigate the absorbed geometric structure of an IL on a semiconductor. Using vacuum deposition to achieve a monolayer of IL on the TiO_2 surface is a systematic technique and further experimental time would provide the opportunity to attempt building more monolayers on the surface. These measurements would produce a comprehensive representation of the IL order or disorder at the surface at different volumes. This deposition technique has been used once in combination with XPS to determine, monolayer by monolayer, the ordering or lack thereof as the quantity of IL grows on the surface.

Using XPS in this approach has the typical limitations of the breadth of information gleaned from the sample; the probe depth is limited and only average measurements of the top monolayer can be carried out while specific geometric information is lacking with this technique. This work has pioneered the use of the NIXSW technique with these IL-semiconductor systems which, combined with calculations, has enabled a thorough examination and conclusion of IL adsorption patterns. Hopefully the success of these first steps has validated the use of this method for these IL-semiconductor interfaces, particularly for the field of electrochemistry.

Overall, this thesis has presented work which has laid the foundation for new approaches to IL research methods. Experimentally, a method to probe ILs at interfaces, and computationally, simulating bulk and ILs at interfaces. These methods may require a higher investment of resources, but this investment is compensated with a high level of accuracy and a vast breadth of data.

7.2. Future work

Future work to develop on the results of this thesis should be based on improving the core level XPS simulation method and developing the experimental investigation of the IL-TiO_2 interface.

There is substantial potential for further analysis using the AIMD calculations carried out in this work for all the bulk ILs and the IL-TiO_2 models. Extracting a larger number of geometries from these AIMD calculations would help to evaluate whether the data set size of E_B chosen has any significant impact on the accuracy (evaluated by E_B shifts, broadening, peak asymmetry) of the simulated core level XP spectra. Although the results presented in this thesis have established a good level of accuracy across a variety of ILs, this is only the first step in simulating core levels using a bulk liquid model. Water, for example, has seen much development in accuracy of computational simulations, after a lot of work in this area.[292] The use of ILs is constantly increasing, so there is value in further improving and testing the accuracy of simulating these systems to, in the long-term, potentially avoid costly experimental work in the early stages of material research and development.

Calculated peak width or broadening has been particularly challenging to consolidate with experiment. It seems that in most ILs, the anion matches the experiment well in this area, but the cation peak is consistently simulated to be significantly less broad than experiment. In this work, a limited analysis of 2 further configurations added to the peak (3 configurations total, 192 data points for the cation, compared to 64 data points from a single configuration) did not make a significant difference to the broadening of the cation peak. If further analysis (10 configurations +) shows that there continues to be no difference, then computational settings would need to be tested. The first route to explore is the effect of inclusion of improved dispersion corrections (Grimme-D3 instead of Grimme-D2) in the bulk ILs and investigate any incurred computational costs across the various ILs. It has been has been shown including Grimme-D2 corrections does not increase the computational cost in the IL $[C_2C_1Im][SCN]$[216], but "upgrading" the dispersion force correction remains to be tested.

In the bulk ILs, it was found that site potentials, which are determined by both long-range interactions and short-range interactions, were the dominant influence in the E_B shifts (Section 4.5.3). It was also observed, in the IL-TiO_2 models, that short-range interactions were significant between interfacial ions of the IL, which influenced the anion's interaction with the surface, *via* bond lengths and adsorption geometries. Therefore, it would be prudent to further investigate the explicit interactions in all the ILs models presented and to what extent short-range interactions affect electronic behaviour compared to that of long-range interactions. The presence and effects of hydrogen-type bonding is of particular interest in ILs and no definitive conclusion on their significance in imidazolium-based ILs has been determined.[40] Further investigation of anion-H_{cation} interactions could be investigated further by extraction of RDFs across the latter, equilibrated halves of the AIMD calculations.

Finally, it is of particular interest to progress the natural extension of the experimental NIXSW IL-TiO_2 work in Chapter 6. Probing the formation of additional monolayers in the surface using this technique could provide fascinating insights to the real concentration and geometry at the buried interface and how additional monolayers influence these features. Further XPS measurements would bring intriguing insight into core E_B shifts as the IL volume is increased, and the transition into 'bulk' IL is made. To support this data, further core E_B calculations would need to be carried

out on the AIMD models presented in this work to accompany these measurements, on many more configurations of the monolayer and on the bulk scale systems. A good place to begin would be to gather 32-64 data points at each scale, to equate to the bulk IL work in Chapters 4 and 5, from a range of configurations at different potential energies and assess any E_B shifts exhibited. An extended investigation would also answer the question of initial state dominance in core E_B on this semiconducting surface. By the progression of this work, a solid understanding of the IL interfacial behaviour with this ubiquitous metal oxide can be constructed.

Bibliography

1. Punning, A.; Kim, K. J.; Palmre, V.; Vidal, F.; Plesse, C.; Festin, N.; Maziz, A.; Asaka, K.; Sugino, T.; Alici, G.; Spinks, G.; Wallace, G.; Must, I.; Poldsalu, I.; Vunder, V.; Temmer, R.; Kruusamae, K.; Torop, J.; Kaasik, F.; Rinne, P.; Johanson, U.; Peikolainen, A. L.; Tamm, T.; Aabloo, A., Ionic electroactive polymer artificial muscles in space applications. *Sci Rep* **2014,** *4*, 6913.

2. Somers, A.; Howlett, P.; MacFarlane, D.; Forsyth, M., A Review of Ionic Liquid Lubricants. *Lubricants* **2013,** *1* (1), 3-21.

3. Keplinger, C.; Sun, J. Y.; Foo, C. C.; Rothemund, P.; Whitesides, G. M.; Suo, Z., Stretchable, transparent, ionic conductors. *Science* **2013,** *341* (6149), 984-7.

4. Azimi, B.; Maleki, H.; Gigante, V.; Bagherzadeh, R.; Mezzetta, A.; Milazzo, M.; Guazzelli, L.; Cinelli, P.; Lazzeri, A.; Danti, S., Cellulose-based fiber spinning processes using ionic liquids. *Cellulose* **2022,** *29* (6), 3079-3129.

5. Endres, F.; Zein El Abedin, S., Air and water stable ionic liquids in physical chemistry. *Phys Chem Chem Phys* **2006,** *8* (18), 2101-16.

6. Plechkova, N. V.; Seddon, K. R., Applications of ionic liquids in the chemical industry. *Chem Soc Rev* **2008,** *37* (1), 123-50.

7. Forsyth, S. A.; Pringle, J. M.; MacFarlane, D. R., Ionic Liquids—An Overview. *Australian Journal of Chemistry* **2004,** *57* (2).

8. MacFarlane, D. R.; Seddon, K. R., Ionic Liquids—Progress on the Fundamental Issues. *Australian Journal of Chemistry* **2007,** *60* (1).

9. Welton, T., Room-Temperature Ionic Liquids. Solvents for Synthesis and Catalysis. *Chem Rev* **1999,** *99* (8), 2071-2084.

10. Jones, H. L.; Osteryoung, R. A., Organic Reactions in Molten Tetrachloroaluminate Solvents. In *Advances in Molten Salt Chemistry*, **1975**; pp 121-176.

11. Gabriel, S.; Weiner, J., Ueber einige Abkömmlinge des Propylamins. *Berichte der deutschen chemischen Gesellschaft* **1888,** *21* (2), 2669-2679.

12. Wilkes, J. S.; Zaworotko, M. J., Air and water stable 1-ethyl-3-methylimidazolium based ionic liquids. *Journal of the Chemical Society, Chemical Communications* **1992,** (13).

13. Chen, L.; Mullen, G. E.; Le Roch, M.; Cassity, C. G.; Gouault, N.; Fadamiro, H. Y.; Barletta, R. E.; O'Brien, R. A.; Sykora, R. E.; Stenson, A. C.; West, K. N.; Horne, H. E.; Hendrich, J. M.; Xiang, K. R.; Davis, J. H., Jr., On the formation of a protic ionic liquid in nature. *Angew Chem Int Ed Engl* **2014,** *53* (44), 11762-5.

14. Lovelock, K. R. J.; Villar-Garcia, I. J.; Maier, F.; Steinrück, H. P.; Licence, P., Photoelectron spectroscopy of ionic liquid-based interfaces. *Chem Rev* **2010,** *110* (9), 5158-90.

15. Kim, G., A PMMA composite as an optical diffuser in a liquid crystal display backlighting unit (BLU). *European Polymer Journal* **2005,** *41* (8), 1729-1737.

16. Dong, B. H.; Jiang, T.; Xu, Z. X.; Lu, H. B.; Wang, S. M., Coagulation Method for Preparing Antimony-Doped Tin Oxide (ATO)/Poly(methyl Methacrylate) Nanocomposites and their Electrical Conductivity and Thermal Stability. *Advanced Materials Research* **2011,** *194-196*, 610-613.

17. Clayton, L. M.; Sikder, A. K.; Kumar, A.; Cinke, M.; Meyyappan, M.; Gerasimov, T. G.; Harmon, J. P., Transparent Poly(methyl methacrylate)/Single-Walled Carbon Nanotube (PMMA/SWNT) Composite Films with Increased Dielectric Constants. *Advanced Functional Materials* **2005,** *15* (1), 101-106.

18. Tsurumaki, A.; Tajima, S.; Iwata, T.; Scrosati, B.; Ohno, H., Evaluation of ionic liquids as novel antistatic agents for polymethacrylates. *Electrochimica Acta* **2017,** *248*, 556-561.

19. Aaserud, O.; Hommeren, O. J.; Tvedt, B.; Nakstad, P.; Mowe, G.; Efskind, J.; Russell, D.; Jorgensen, E. B.; Nyberg-Hansen, R.; Rootwelt, K.; et al., Carbon disulfide exposure and neurotoxic sequelae among viscose rayon workers. *Am J Ind Med* **1990,** *18* (1), 25-37.

20. Rosenau, T.; Potthast, A.; Sixta, H.; Kosma, P., The chemistry of side reactions and byproduct formation in the system NMMO/cellulose (Lyocell process). *Progress in Polymer Science* **2001,** *26* (9), 1763-1837.

21. Fink, H. P.; Weigel, P.; Purz, H. J.; Ganster, J., Structure formation of regenerated cellulose materials from NMMO-solutions. *Progress in Polymer Science* **2001,** *26* (9), 1473-1524.

22. Brandt-Talbot, A.; Gschwend, F. J. V.; Fennell, P. S.; Lammens, T. M.; Tan, B.; Weale, J.; Hallett, J. P., An economically viable ionic liquid for the fractionation of lignocellulosic biomass. *Green Chemistry* **2017,** *19* (13), 3078-3102.

23. Brandt, A.; Gräsvik, J.; Hallett, J. P.; Welton, T., Deconstruction of lignocellulosic biomass with ionic liquids. *Green Chemistry* **2013,** *15* (3).

24. Ventura, S. P. M.; FA, E. S.; Quental, M. V.; Mondal, D.; Freire, M. G.; Coutinho, J. A. P., Ionic-Liquid-Mediated Extraction and Separation Processes for Bioactive Compounds: Past, Present, and Future Trends. *Chem Rev* **2017,** *117* (10), 6984-7052.

25. Amiril, S. A. S.; Rahim, E. A.; Syahrullail, S., A review on ionic liquids as sustainable lubricants in manufacturing and engineering: Recent research, performance, and applications. *Journal of Cleaner Production* **2017,** *168*, 1571-1589.

26. Tan, S. S.; Macfarlane, D. R., Ionic liquids in biomass processing. *Top Curr Chem* **2010,** *290*, 311-39.

27. Wasserscheid, P.; Welton, T., *Ionic liquids in synthesis*. Wiley-VCH: Weinheim, 2008.

28. Pham, T. P.; Cho, C. W.; Yun, Y. S., Environmental fate and toxicity of ionic liquids: a review. *Water Res* **2010,** *44* (2), 352-72.

29. Romero, A.; Santos, A.; Tojo, J.; Rodriguez, A., Toxicity and biodegradability of imidazolium ionic liquids. *J Hazard Mater* **2008,** *151* (1), 268-73.

30. Tsuzuki, S.; Tokuda, H.; Hayamizu, K.; Watanabe, M., Magnitude and directionality of interaction in ion pairs of ionic liquids: relationship with ionic conductivity. *J Phys Chem B* **2005,** *109* (34), 16474-81.

31. Weingartner, H., Understanding ionic liquids at the molecular level: facts, problems, and controversies. *Angew Chem Int Ed Engl* **2008,** *47* (4), 654-70.

32. Holloczki, O.; Malberg, F.; Welton, T.; Kirchner, B., On the origin of ionicity in ionic liquids. Ion pairing versus charge transfer. *Phys Chem Chem Phys* **2014,** *16* (32), 16880-90.

33. Morrow, T. I.; Maginn, E. J., Molecular Dynamics Study of the Ionic Liquid 1-n-Butyl-3-methylimidazolium Hexafluorophosphate. *The Journal of Physical Chemistry B* **2002,** *106* (49), 12807-12813.

34. Buhl, M.; Chaumont, A.; Schurhammer, R.; Wipff, G., Ab initio molecular dynamics of liquid 1,3-dimethylimidazolium chloride. *J Phys Chem B* **2005,** *109* (39), 18591-9.

35. Kossmann, S.; Thar, J.; Kirchner, B.; Hunt, P. A.; Welton, T., Cooperativity in ionic liquids. *J Chem Phys* **2006,** *124* (17), 174506.

36. Cremer, T.; Kolbeck, C.; Lovelock, K. R. J.; Paape, N.; Wölfel, R.; Schulz, P. S.; Wasserscheid, P.; Weber, H.; Thar, J.; Kirchner, B.; Maier, F.; Steinrück, H. P., Towards a molecular understanding of cation-anion interactions--probing the electronic structure of imidazolium ionic liquids by NMR spectroscopy, X-ray photoelectron spectroscopy and theoretical calculations. *Chemistry* **2010,** *16* (30), 9018-33.

37. Philippi, F.; Goloviznina, K.; Gong, Z.; Gehrke, S.; Kirchner, B.; Padua, A. A. H.; Hunt, P. A., Charge transfer and polarisability in ionic liquids: a case study. *Phys Chem Chem Phys* **2022,** *24* (5), 3144-3162.

38. Schroder, C.; Lyons, A.; Rick, S. W., Polarizable MD simulations of ionic liquids: How does additional charge transfer change the dynamics? *Phys Chem Chem Phys* **2020,** *22* (2), 467-477.

39. Youngs, T. G.; Hardacre, C., Application of static charge transfer within an ionic-liquid force field and its effect on structure and dynamics. *Chemphyschem* **2008,** *9* (11), 1548-58.

40. Lehmann, S. B.; Roatsch, M.; Schoppke, M.; Kirchner, B., On the physical origin of the cation-anion intermediate bond in ionic liquids Part I. Placing a (weak) hydrogen bond between two charges. *Phys Chem Chem Phys* **2010,** *12* (27), 7473-86.

41. Zhang, S.; Sun, N.; He, X.; Lu, X.; Zhang, X., Physical Properties of Ionic Liquids: Database and Evaluation. *Journal of Physical and Chemical Reference Data* **2006,** *35* (4), 1475-1517.

42. Lin, J.; Zhang, C.; Yan, Z.; Zhu, Y.; Peng, Z.; Hauge, R. H.; Natelson, D.; Tour, J. M., 3-Dimensional graphene carbon nanotube carpet-based microsupercapacitors with high electrochemical performance. *Nano Lett* **2013,** *13* (1), 72-8.

43. Li, B.; Wang, L.; Kang, B.; Wang, P.; Qiu, Y., Review of recent progress in solid-state dye-sensitized solar cells. *Solar Energy Materials and Solar Cells* **2006,** *90* (5), 549-573.

44. Noda, A.; Susan, M. A. B. H.; Kudo, K.; Mitsushima, S.; Hayamizu, K.; Watanabe, M., Brønsted Acid−Base Ionic Liquids as Proton-Conducting Nonaqueous Electrolytes. *The Journal of Physical Chemistry B* **2003,** *107* (17), 4024-4033.

45. Bai, S.; Da, P.; Li, C.; Wang, Z.; Yuan, Z.; Fu, F.; Kawecki, M.; Liu, X.; Sakai, N.; Wang, J. T.; Huettner, S.; Buecheler, S.; Fahlman, M.; Gao, F.; Snaith, H. J., Planar perovskite solar cells with long-term stability using ionic liquid additives. *Nature* **2019,** *571* (7764), 245-250.

46. Yang, D.; Zhou, X.; Yang, R.; Yang, Z.; Yu, W.; Wang, X.; Li, C.; Liu, S.; Chang, R. P. H., Surface optimization to eliminate hysteresis for record efficiency planar perovskite solar cells. *Energy & Environmental Science* **2016,** *9* (10), 3071-3078.

47. Merlet, C.; Rotenberg, B.; Madden, P. A.; Taberna, P. L.; Simon, P.; Gogotsi, Y.; Salanne, M., On the molecular origin of supercapacitance in nanoporous carbon electrodes. *Nat Mater* **2012,** *11* (4), 306-10.

48. Zeng, W.; Cao, Y.; Bai, Y.; Wang, Y.; Shi, Y.; Zhang, M.; Wang, F.; Pan, C.; Wang, P., Efficient Dye-Sensitized Solar Cells with an Organic Photosensitizer Featuring Orderly Conjugated Ethylenedioxythiophene and Dithienosilole Blocks. *Chemistry of Materials* **2010,** *22* (5), 1915-1925.

49. Lewandowski, A.; Świderska-Mocek, A., Ionic liquids as electrolytes for Li-ion batteries—An overview of electrochemical studies. *Journal of Power Sources* **2009,** *194* (2), 601-609.

50. Galiński, M.; Lewandowski, A.; Stępniak, I., Ionic liquids as electrolytes. *Electrochimica Acta* **2006,** *51* (26), 5567-5580.

51. Lukatskaya, M. R.; Dunn, B.; Gogotsi, Y., Multidimensional materials and device architectures for future hybrid energy storage. *Nat Commun* **2016,** *7*, 12647.

52. Balducci, A.; Henderson, W. A.; Mastragostino, M.; Passerini, S.; Simon, P.; Soavi, F., Cycling stability of a hybrid activated carbon//poly(3-methylthiophene) supercapacitor with N-

butyl-N-methylpyrrolidinium bis(trifluoromethanesulfonyl)imide ionic liquid as electrolyte. *Electrochimica Acta* **2005,** *50* (11), 2233-2237.

53. Liu, H.; He, P.; Li, Z.; Liu, Y.; Li, J., A novel nickel-based mixed rare-earth oxide/activated carbon supercapacitor using room temperature ionic liquid electrolyte. *Electrochimica Acta* **2006,** *51* (10), 1925-1931.

54. Zhu, Y.; Murali, S.; Stoller, M. D.; Ganesh, K. J.; Cai, W.; Ferreira, P. J.; Pirkle, A.; Wallace, R. M.; Cychosz, K. A.; Thommes, M.; Su, D.; Stach, E. A.; Ruoff, R. S., Carbon-based supercapacitors produced by activation of graphene. *Science* **2011,** *332* (6037), 1537-41.

55. Vatamanu, J.; Hu, Z.; Bedrov, D.; Perez, C.; Gogotsi, Y., Increasing Energy Storage in Electrochemical Capacitors with Ionic Liquid Electrolytes and Nanostructured Carbon Electrodes. *The Journal of Physical Chemistry Letters* **2013,** *4* (17), 2829-2837.

56. Sun, H.; Zhu, G.; Xu, X.; Liao, M.; Li, Y. Y.; Angell, M.; Gu, M.; Zhu, Y.; Hung, W. H.; Li, J.; Kuang, Y.; Meng, Y.; Lin, M. C.; Peng, H.; Dai, H., A safe and non-flammable sodium metal battery based on an ionic liquid electrolyte. *Nat Commun* **2019,** *10* (1), 3302.

57. Sun, H.; Zhu, G.; Zhu, Y.; Lin, M. C.; Chen, H.; Li, Y. Y.; Hung, W. H.; Zhou, B.; Wang, X.; Bai, Y.; Gu, M.; Huang, C. L.; Tai, H. C.; Xu, X.; Angell, M.; Shyue, J. J.; Dai, H., High-Safety and High-Energy-Density Lithium Metal Batteries in a Novel Ionic-Liquid Electrolyte. *Adv Mater* **2020,** *32* (26), e2001741.

58. Zhang, S. S., A review on electrolyte additives for lithium-ion batteries. *Journal of Power Sources* **2006,** *162* (2), 1379-1394.

59. Zhang, H.; Liu, X.; Li, H.; Hasa, I.; Passerini, S., Challenges and Strategies for High-Energy Aqueous Electrolyte Rechargeable Batteries. *Angew Chem Int Ed Engl* **2021,** *60* (2), 598-616.

60. Zhang, Y.; Ye, R.; Henkensmeier, D.; Hempelmann, R.; Chen, R., "Water-in-ionic liquid" solutions towards wide electrochemical stability windows for aqueous rechargeable batteries. *Electrochimica Acta* **2018,** *263*, 47-52.

61. Diebold, U., The surface science of titanium dioxide. *Surface Science Reports* **2003,** *48* (5-8), 53-229.

62. Chen, X.; Selloni, A., Introduction: titanium dioxide (TiO2) nanomaterials. *Chem Rev* **2014,** *114* (19), 9281-2.

63. O'Regan, B.; Grätzel, M., A low-cost, high-efficiency solar cell based on dye-sensitized colloidal TiO2 films. *Nature* **1991,** *353* (6346), 737-740.

64. Asahi, R.; Morikawa, T.; Ohwaki, T.; Aoki, K.; Taga, Y., Visible-light photocatalysis in nitrogen-doped titanium oxides. *Science* **2001,** *293* (5528), 269-71.

65. Linsebigler, A. L.; Lu, G.; Yates, J. T., Photocatalysis on TiO2 Surfaces: Principles, Mechanisms, and Selected Results. *Chemical Reviews* **2002,** *95* (3), 735-758.

66. Burschka, J.; Pellet, N.; Moon, S. J.; Humphry-Baker, R.; Gao, P.; Nazeeruddin, M. K.; Gratzel, M., Sequential deposition as a route to high-performance perovskite-sensitized solar cells. *Nature* **2013,** *499* (7458), 316-9.

67. Hagfeldt, A.; Boschloo, G.; Sun, L.; Kloo, L.; Pettersson, H., Dye-sensitized solar cells. *Chem Rev* **2010,** *110* (11), 6595-663.

68. Nazeeruddin, M. K.; Kay, A.; Rodicio, I.; Humphry-Baker, R.; Mueller, E.; Liska, P.; Vlachopoulos, N.; Graetzel, M., Conversion of light to electricity by cis-X2bis(2,2'-bipyridyl-4,4'-dicarboxylate)ruthenium(II) charge-transfer sensitizers (X = Cl-, Br-, I-, CN-, and SCN-) on nanocrystalline titanium dioxide electrodes. *Journal of the American Chemical Society* **2002,** *115* (14), 6382-6390.

69. Yella, A.; Lee, H. W.; Tsao, H. N.; Yi, C.; Chandiran, A. K.; Nazeeruddin, M. K.; Diau, E. W.; Yeh, C. Y.; Zakeeruddin, S. M.; Gratzel, M., Porphyrin-sensitized solar cells with cobalt (II/III)-based redox electrolyte exceed 12 percent efficiency. *Science* **2011,** *334* (6056), 629-34.

70. Fujishima, A.; Zhang, X.; Tryk, D., TiO2 photocatalysis and related surface phenomena. *Surface Science Reports* **2008,** *63* (12), 515-582.

71. Chen, X.; Liu, L.; Yu, P. Y.; Mao, S. S., Increasing solar absorption for photocatalysis with black hydrogenated titanium dioxide nanocrystals. *Science* **2011,** *331* (6018), 746-50.

72. Ramamoorthy, M.; Vanderbilt, D.; King-Smith, R. D., First-principles calculations of the energetics of stoichiometric TiO2 surfaces. *Phys Rev B Condens Matter* **1994,** *49* (23), 16721-16727.

73. Le Bideau, J.; Viau, L.; Vioux, A., Ionogels, ionic liquid based hybrid materials. *Chem Soc Rev* **2011,** *40* (2), 907-25.

74. Kilpelainen, I.; Xie, H.; King, A.; Granstrom, M.; Heikkinen, S.; Argyropoulos, D. S., Dissolution of wood in ionic liquids. *J Agric Food Chem* **2007,** *55* (22), 9142-8.

75. Shkrob, I. A.; Marin, T. W., The AHA Moment: Assessment of the Redox Stability of Ionic Liquids Based on Aromatic Heterocyclic Anions (AHAs) for Nuclear Separations and Electric Energy Storage. *J Phys Chem B* **2015,** *119* (46), 14766-79.

76. Armand, M.; Endres, F.; MacFarlane, D. R.; Ohno, H.; Scrosati, B., Ionic-liquid materials for the electrochemical challenges of the future. *Nat Mater* **2009,** *8* (8), 621-9.

77. Handy, S. T., Grignard reactions in imidazolium ionic liquids. *J Org Chem* **2006,** *71* (12), 4659-62.

78. Anderson, J. L.; Ding, R.; Ellern, A.; Armstrong, D. W., Structure and properties of high stability geminal dicationic ionic liquids. *J Am Chem Soc* **2005,** *127* (2), 593-604.

79. Jadhav, A. H.; Kim, H., Short oligo (ethylene glycol) functionalized imidazolium dicationic room temperature ionic liquids: Synthesis, properties, and catalytic activity in azidation. *Chemical Engineering Journal* **2012,** *200-202*, 264-274.

80. Jadhav, A. H.; Chinnappan, A.; Patil, R. H.; Kostjuk, S. V.; Kim, H., Green chemical conversion of fructose into 5-hydroxymethylfurfural (HMF) using unsymmetrical dicationic ionic liquids under mild reaction condition. *Chemical Engineering Journal* **2014,** *243*, 92-98.

81. Planellas, M.; Pleixats, R.; Shafir, A., Palladium Nanoparticles in Suzuki Cross-Couplings: Tapping into the Potential of Tris-Imidazolium Salts for Nanoparticle Stabilization. *Advanced Synthesis & Catalysis* **2012,** *354* (4), 651-662.

82. Nacham, O.; Martín-Pérez, A.; Steyer, D. J.; Trujillo-Rodríguez, M. J.; Anderson, J. L.; Pino, V.; Afonso, A. M., Interfacial and aggregation behavior of dicationic and tricationic ionic liquid-based surfactants in aqueous solution. *Colloids and Surfaces A: Physicochemical and Engineering Aspects* **2015,** *469*, 224-234.

83. Gousseva, E.; Midgley, S. D.; Seymour, J. M.; Seidel, R.; Grau-Crespo, R.; Lovelock, K. R. J., Understanding X-ray Photoelectron Spectra of Ionic Liquids: Experiments and Simulations of 1-Butyl-3-methylimidazolium Thiocyanate. *J Phys Chem B* **2022,** *126* (49), 10500-10509.

84. Einstein, A., Über einen die Erzeugung und Verwandlung des Lichtes betreffenden heuristischen Gesichtspunkt. *Annalen der Physik* **1905,** *322* (6), 132-148.

85. Siegbahn, K.; Edvarson, K., β-Ray spectroscopy in the precision range of 1 : 105. *Nuclear Physics* **1956,** *1* (8), 137-159.

86. Winter, B.; Thurmer, S.; Wilkinson, I., Absolute Electronic Energetics and Quantitative Work Functions of Liquids from Photoelectron Spectroscopy. *Acc Chem Res* **2023**.

87. Villar-Garcia, I. J.; Smith, E. F.; Taylor, A. W.; Qiu, F.; Lovelock, K. R. J.; Jones, R. G.; Licence, P., Charging of ionic liquid surfaces under X-ray irradiation: the measurement of absolute binding energies by XPS. *Phys Chem Chem Phys* **2011,** *13* (7), 2797-808.

88. Lembinen, M.; Nõmmiste, E.; Ers, H.; Docampo-Álvarez, B.; Kruusma, J.; Lust, E.; Ivaništšev, V. B., Calculation of core-level electron spectra of ionic liquids. *International Journal of Quantum Chemistry* **2020,** *120* (14), e26247.

89. Vickerman, J. C.; Gilmore, I. S., *Surface Analysis: The Principal Techniques*. John Wiley & Sons: Chichester, **2009**.

90. Briggs, D.; Grant, J. T., *Surface Analysis by Auger and x-Ray Photoelectron Spectroscopy*. IM Publications LLP: Chichester, **2003**; p 899.

91. Seymour, J. M.; Gousseva, E.; Large, A. I.; Clarke, C. J.; Licence, P.; Fogarty, R. M.; Duncan, D. A.; Ferrer, P.; Venturini, F.; Bennett, R. A.; Palgrave, R. G.; Lovelock, K. R. J., Experimental measurement and prediction of ionic liquid ionisation energies. *Phys Chem Chem Phys* **2021,** *23* (37), 20957-20973.

92. Bier, M.; Dietrich, S., Vapour pressure of ionic liquids. *Molecular Physics* **2010,** *108* (2), 211-214.

93. Kolbeck, C.; Cremer, T.; Lovelock, K. R.; Paape, N.; Schulz, P. S.; Wasserscheid, P.; Maier, F.; Steinruck, H. P., Influence of different anions on the surface composition of ionic liquids studied using ARXPS. *J Phys Chem B* **2009,** *113* (25), 8682-8.

94. Nicolas, C.; Miron, C., Lifetime broadening of core-excited and -ionized states. *J Electron Spectrosc* **2012,** *185* (8-9), 267-272.

95. Prince, K. C.; Vondráček, M.; Karvonen, J.; Coreno, M.; Camilloni, R.; Avaldi, L.; de Simone, M., A critical comparison of selected 1s and 2p core hole widths. *J Electron Spectrosc* **1999,** *101-103*, 141-147.

96. Krause, M. O.; Oliver, J. H., Natural widths of atomic K and L levels, Kα X-ray lines and several KLL Auger lines. *Journal of Physical and Chemical Reference Data* **1979,** *8* (2), 329-338.

97. Baer, D. R.; Artyushkova, K.; Cohen, H.; Easton, C. D.; Engelhard, M.; Gengenbach, T. R.; Greczynski, G.; Mack, P.; Morgan, D. J.; Roberts, A., XPS guide: Charge neutralization and binding energy referencing for insulating samples. *Journal of Vacuum Science & Technology A* **2020,** *38* (3), 031204.

98. Greczynski, G.; Hultman, L., C 1s Peak of Adventitious Carbon Aligns to the Vacuum Level: Dire Consequences for Material's Bonding Assignment by Photoelectron Spectroscopy. *Chemphyschem* **2017,** *18* (12), 1507-1512.

99. Greczynski, G.; Hultman, L., X-ray photoelectron spectroscopy: Towards reliable binding energy referencing. *Progress in Materials Science* **2020,** *107*.

100. Greczynski, G.; Hultman, L., Reliable determination of chemical state in x-ray photoelectron spectroscopy based on sample-work-function referencing to adventitious carbon: Resolving the myth of apparent constant binding energy of the C 1s peak. *Applied Surface Science* **2018,** *451*, 99-103.

101. Greczynski, G.; Hultman, L., Compromising Science by Ignorant Instrument Calibration-Need to Revisit Half a Century of Published XPS Data. *Angew Chem Int Ed Engl* **2020,** *59* (13), 5002-5006.

102. Lovelock, K. R. J.; Kolbeck, C.; Cremer, T.; Paape, N.; Schulz, P. S.; Wasserscheid, P.; Maier, F.; Steinrück, H. P., Influence of different substituents on the surface composition of ionic liquids studied using ARXPS. *J Phys Chem B* **2009,** *113* (9), 2854-64.

103. Smith, E. F.; Rutten, F. J.; Villar-Garcia, I. J.; Briggs, D.; Licence, P., Ionic liquids in vacuo: analysis of liquid surfaces using ultra-high-vacuum techniques. *Langmuir* **2006,** *22* (22), 9386-92.

104. Bedzyk, M. J.; Cheng, L., X-ray Standing Wave Studies of Minerals and Mineral Surfaces: Principles and Applications. *Reviews in Mineralogy and Geochemistry* **2002,** *49* (1), 221-266.

105. Dalton, J., *A New System of Chemical Philosophy*. Cambridge University Press: Cambridge, **1808**.

106. Newman, M. S., A notation for the study of certain stereochemical problems. *Journal of Chemical Education* **1955,** *32* (7).

107. Karplus, M.; Porter, R. N.; Sharma, R. D., Energy Dependence of Cross Sections for Hot Tritium Reactions with Hydrogen and Deuterium Molecules. *The Journal of Chemical Physics* **1966,** *45* (10), 3871-3873.

108. Bagus, P. S.; Brundle, C. R.; Illas, F.; Parmigiani, F.; Polzonetti, G., Evidence for oxygen-island formation on Al(111): Cluster-model theory and x-ray photoelectron spectroscopy. *Phys Rev B Condens Matter* **1991,** *44* (16), 9025-9034.

109. Del Popolo, M. G.; Lynden-Bell, R. M.; Kohanoff, J., Ab initio molecular dynamics simulation of a room temperature ionic liquid. *J Phys Chem B* **2005,** *109* (12), 5895-902.

110. Szabadi, A.; Elfgen, R.; Macchieraldo, R.; Kearns, F. L.; Lee Woodcock, H.; Kirchner, B.; Schröder, C., Comparison between ab initio and polarizable molecular dynamics simulations of 1-butyl-3-methylimidazolium tetrafluoroborate and chloride in water. *Journal of Molecular Liquids* **2021,** *337*.

111. Yue, K.; Doherty, B.; Acevedo, O., Comparison between Ab Initio Molecular Dynamics and OPLS-Based Force Fields for Ionic Liquid Solvent Organization. *J Phys Chem B* **2022,** *126* (21), 3908-3919.

112. Youngs, T. G.; Del Popolo, M. G.; Kohanoff, J., Development of complex classical force fields through force matching to ab initio data: application to a room-temperature ionic liquid. *J Phys Chem B* **2006,** *110* (11), 5697-707.

113. Kirchner, B.; di Dio, P. J.; Hutter, J., Real-world predictions from ab initio molecular dynamics simulations. *Top Curr Chem* **2012,** *307*, 109-53.

114. Jensen, F., *Introduction to Computational Chemistry*. 3rd edition ed.; John Wiley & Sons: Hoboken, New Jersey, **2017**.

115. Canongia Lopes, J. N.; Deschamps, J.; Pádua, A. A. H., Modeling Ionic Liquids Using a Systematic All-Atom Force Field. *The Journal of Physical Chemistry B* **2004,** *108* (6), 2038-2047.

116. Liu, Z.; Huang, S.; Wang, W., A Refined Force Field for Molecular Simulation of Imidazolium-Based Ionic Liquids. *The Journal of Physical Chemistry B* **2004,** *108* (34), 12978-12989.

117. Sambasivarao, S. V.; Acevedo, O., Development of OPLS-AA Force Field Parameters for 68 Unique Ionic Liquids. *J Chem Theory Comput* **2009,** *5* (4), 1038-50.

118. Chaban, V. V.; Voroshylova, I. V., Systematic refinement of Canongia Lopes-Padua force field for pyrrolidinium-based ionic liquids. *J Phys Chem B* **2015,** *119* (20), 6242-9.

119. Liu, Z.; Wu, X.; Wang, W., A novel united-atom force field for imidazolium-based ionic liquids. *Phys Chem Chem Phys* **2006,** *8* (9), 1096-104.

120. Liu, Z.; Chen, T.; Bell, A.; Smit, B., Improved united-atom force field for 1-alkyl-3-methylimidazolium chloride. *J Phys Chem B* **2010,** *114* (13), 4572-82.

121. Zhong, X.; Liu, Z.; Cao, D., Improved classical united-atom force field for imidazolium-based ionic liquids: tetrafluoroborate, hexafluorophosphate, methylsulfate, trifluoromethylsulfonate, acetate, trifluoroacetate, and bis(trifluoromethylsulfonyl)amide. *J Phys Chem B* **2011,** *115* (33), 10027-40.

122. Doherty, B.; Zhong, X.; Acevedo, O., Virtual Site OPLS Force Field for Imidazolium-Based Ionic Liquids. *J Phys Chem B* **2018,** *122* (11), 2962-2974.

123. Schroder, C., Comparing reduced partial charge models with polarizable simulations of ionic liquids. *Phys Chem Chem Phys* **2012,** *14* (9), 3089-102.

124. Borodin, O., Polarizable force field development and molecular dynamics simulations of ionic liquids. *J Phys Chem B* **2009,** *113* (33), 11463-78.

125. Schroder, C.; Steinhauser, O., Simulating polarizable molecular ionic liquids with Drude oscillators. *J Chem Phys* **2010,** *133* (15), 154511.

126. Yan, T.; Burnham, C. J.; Del Pópolo, M. G.; Voth, G. A., Molecular Dynamics Simulation of Ionic Liquids: The Effect of Electronic Polarizability. *The Journal of Physical Chemistry B* **2004,** *108* (32), 11877-11881.

127. Yan, T.; Wang, Y.; Knox, C., On the structure of ionic liquids: comparisons between electronically polarizable and nonpolarizable models I. *J Phys Chem B* **2010,** *114* (20), 6905-21.

128. Bedrov, D.; Piquemal, J. P.; Borodin, O.; MacKerell, A. D., Jr.; Roux, B.; Schroder, C., Molecular Dynamics Simulations of Ionic Liquids and Electrolytes Using Polarizable Force Fields. *Chem Rev* **2019,** *119* (13), 7940-7995.

129. Borodin, O.; Smith, G. D., Structure and dynamics of N-methyl-N-propylpyrrolidinium bis(trifluoromethanesulfonyl)imide ionic liquid from molecular dynamics simulations. *J Phys Chem B* **2006,** *110* (23), 11481-90.

130. Müller-Plathe, F.; van Gunsteren, W. F., Computer simulation of a polymer electrolyte: Lithium iodide in amorphous poly(ethylene oxide). *The Journal of Chemical Physics* **1995,** *103* (11), 4745-4756.

131. Kohagen, M.; Brehm, M.; Thar, J.; Zhao, W.; Muller-Plathe, F.; Kirchner, B., Performance of quantum chemically derived charges and persistence of ion cages in ionic liquids. A molecular dynamics simulations study of 1-n-butyl-3-methylimidazolium bromide. *J Phys Chem B* **2011,** *115* (4), 693-702.

132. Mondal, A.; Balasubramanian, S., Quantitative prediction of physical properties of imidazolium based room temperature ionic liquids through determination of condensed phase site charges: a refined force field. *J Phys Chem B* **2014,** *118* (12), 3409-22.

133. Kohagen, M.; Brehm, M.; Lingscheid, Y.; Giernoth, R.; Sangoro, J.; Kremer, F.; Naumov, S.; Iacob, C.; Karger, J.; Valiullin, R.; Kirchner, B., How hydrogen bonds influence the mobility of imidazolium-based ionic liquids. A combined theoretical and experimental study of 1-n-butyl-3-methylimidazolium bromide. *J Phys Chem B* **2011,** *115* (51), 15280-8.

134. Mayo, S. L.; Olafson, B. D.; Goddard, W. A., DREIDING: a generic force field for molecular simulations. *The Journal of Physical Chemistry* **2002,** *94* (26), 8897-8909.

135. Born, M.; Oppenheimer, R., Zur Quantentheorie der Molekeln. *Annalen der Physik* **1927,** *389* (20), 457-484.

136. Hohenberg, P.; Kohn, W., Inhomogeneous Electron Gas. *Physical Review* **1964,** *136* (3B), B864-B871.

137. Kohn, W.; Sham, L. J., Self-Consistent Equations Including Exchange and Correlation Effects. *Physical Review* **1965,** *140* (4A), A1133-A1138.

138. Perdew, J. P.; Burke, K.; Ernzerhof, M., Generalized Gradient Approximation Made Simple. *Phys Rev Lett* **1996,** *77* (18), 3865-3868.

139. Becke, A. D., Density-functional thermochemistry. III. The role of exact exchange. *The Journal of Chemical Physics* **1993,** *98* (7), 5648-5652.

140. Stephens, P. J.; Devlin, F. J.; Chabalowski, C. F.; Frisch, M. J., Ab Initio Calculation of Vibrational Absorption and Circular Dichroism Spectra Using Density Functional Force Fields. *The Journal of Physical Chemistry* **2002,** *98* (45), 11623-11627.

141. Shah, J. K., Ab Initio Molecular Dynamics Simulations of Ionic Liquids. In *Annual Reports in Computational chemistry*, Elsevier Science Bv: Amsterdam, **2018**; Vol. 14, pp 95-122.

142. Kuhne, T. D.; Iannuzzi, M.; Del Ben, M.; Rybkin, V. V.; Seewald, P.; Stein, F.; Laino, T.; Khaliullin, R. Z.; Schutt, O.; Schiffmann, F.; Golze, D.; Wilhelm, J.; Chulkov, S.; Bani-Hashemian, M. H.; Weber, V.; Borstnik, U.; Taillefumier, M.; Jakobovits, A. S.; Lazzaro, A.; Pabst, H.; Muller, T.; Schade, R.; Guidon, M.; Andermatt, S.; Holmberg, N.; Schenter, G. K.; Hehn, A.; Bussy, A.; Belleflamme, F.; Tabacchi, G.; Gloss, A.; Lass, M.; Bethune, I.; Mundy, C. J.; Plessl, C.; Watkins, M.; VandeVondele, J.; Krack, M.; Hutter, J., CP2K: An electronic structure and molecular dynamics software package - Quickstep: Efficient and accurate electronic structure calculations. *J Chem Phys* **2020,** *152* (19), 194103.

143. Fletcher, R., *Practical Methods of Optimization*. 2nd edition ed.; John Wiley & Sons: Hoboken, New Jersey, **2000**.

144. Kresse, G.; Furthmüller, J., Efficiency of ab-initio total energy calculations for metals and semiconductors using a plane-wave basis set. *Computational Materials Science* **1996,** *6* (1), 15-50.

145. Kresse, G.; Furthmüller, J., Efficient iterative schemes for ab initio total-energy calculations using a plane-wave basis set. *Phys Rev B Condens Matter* **1996,** *54* (16), 11169-11186.

146. Kresse, G.; Joubert, D., From ultrasoft pseudopotentials to the projector augmented-wave method. *Physical Review B* **1999,** *59* (3), 1758-1775.

147. Kresse, G.; Hafner, J., Norm-conserving and ultrasoft pseudopotentials for first-row and transition elements. *Journal of Physics: Condensed Matter* **1994,** *6* (40), 8245-8257.

148. Goedecker, S.; Teter, M.; Hutter, J., Separable dual-space Gaussian pseudopotentials. *Phys Rev B Condens Matter* **1996,** *54* (3), 1703-1710.

149. Blöchl, P. E., Projector augmented-wave method. *Phys Rev B Condens Matter* **1994,** *50* (24), 17953-17979.

150. Grimme, S., Semiempirical GGA-type density functional constructed with a long-range dispersion correction. *J Comput Chem* **2006,** *27* (15), 1787-99.

151. Grimme, S.; Antony, J.; Ehrlich, S.; Krieg, H., A consistent and accurate ab initio parametrization of density functional dispersion correction (DFT-D) for the 94 elements H-Pu. *J Chem Phys* **2010,** *132* (15), 154104.

152. Welton, T., Ionic liquids in catalysis. *Coordination Chemistry Reviews* **2004,** *248* (21-24), 2459-2477.

153. Chiappe, C.; Pieraccini, D., Ionic liquids: solvent properties and organic reactivity. *Journal of Physical Organic Chemistry* **2005,** *18* (4), 275-297.

154. Khan, A. S.; Man, Z.; Arvina, A.; Bustam, M. A.; Nasrullah, A.; Ullah, Z.; Sarwono, A.; Muhammad, N., Dicationic imidazolium based ionic liquids: Synthesis and properties. *Journal of Molecular Liquids* **2017,** *227*, 98-105.

155. Hallett, J. P.; Welton, T., Room-Temperature Ionic Liquids: Solvents for Synthesis and Catalysis. 2. *Chemical Reviews* **2011,** *111* (5), 3508-3576.

156. Wilkes, J., Properties of ionic liquid solvents for catalysis. *Journal of Molecular Catalysis A: Chemical* **2004,** *214* (1), 11-17.

157. Philippi, F.; Pugh, D.; Rauber, D.; Welton, T.; Hunt, P. A., Conformational design concepts for anions in ionic liquids. *Chemical Science* **2020,** *11* (25), 6405-6422.

158. Koutsoukos, S.; Philippi, F.; Malaret, F.; Welton, T., A review on machine learning algorithms for the ionic liquid chemical space. *Chem Sci* **2021,** *12* (20), 6820-6843.

159. Macchieraldo, R.; Esser, L.; Elfgen, R.; Voepel, P.; Zahn, S.; Smarsly, B. M.; Kirchner, B., Hydrophilic Ionic Liquid Mixtures of Weakly and Strongly Coordinating Anions with and without Water. *ACS Omega* **2018,** *3* (8), 8567-8582.

160. Briggs, D.; Grant, J. T., *Surface Analysis by Auger and X-Ray Photoelectron Spectroscopy*. IM Publications: Manchester, **2003**.

161. Lovelock, K. R. J.; Licence, P., Ionic Liquids Studied at Ultra-High Vacuum. In *Ionic Liquids UnCOILed: Critical Expert Overviews*, Seddon, K. R.; Plechkova, N. V., Eds. Wiley: Oxford, **2012**; pp 251-282.

162. Steinrück, H. P., Recent developments in the study of ionic liquid interfaces using X-ray photoelectron spectroscopy and potential future directions. *Phys Chem Chem Phys* **2012,** *14* (15), 5010-29.

163. Steinrück, H. P.; Libuda, J.; Wasserscheid, P.; Cremer, T.; Kolbeck, C.; Laurin, M.; Maier, F.; Sobota, M.; Schulz, P. S.; Stark, M., Surface science and model catalysis with ionic liquid-modified materials. *Adv Mater* **2011,** *23* (22-23), 2571-87.

164. Maier, F.; Cremer, T.; Kolbeck, C.; Lovelock, K. R. J.; Paape, N.; Schulz, P. S.; Wasserscheid, P.; Steinrück, H. P., Insights into the surface composition and enrichment effects of ionic liquids and ionic liquid mixtures. *Phys Chem Chem Phys* **2010,** *12* (8), 1905-15.

165. Steinrück, H.-P.; Wasserscheid, P., Ionic Liquids in Catalysis. *Catalysis Letters* **2014,** *145* (1), 380-397.

166. Hohlneicher, G.; Pulm, H.; Freund, H. J., On the Separation of Initial and Final-State Effects in Photoelectron-Spectroscopy Using an Extension of the Auger-Parameter Concept. *J Electron Spectrosc* **1985,** *37* (3), 209-224.

167. Egelhoff, W. F., Core-level binding-energy shifts at surfaces and in solids. *Surface Science Reports* **1987,** *6* (6-8), 253-415.

168. Men, S.; Lovelock, K. R. J.; Licence, P., X-ray photoelectron spectroscopy of pyrrolidinium-based ionic liquids: cation-anion interactions and a comparison to imidazolium-based analogues. *Phys Chem Chem Phys* **2011,** *13* (33), 15244-55.

169. Hurisso, B. B.; Lovelock, K. R. J.; Licence, P., Amino acid-based ionic liquids: using XPS to probe the electronic environment via binding energies. *Phys Chem Chem Phys* **2011,** *13* (39), 17737-48.

170. Taylor, A. W.; Men, S.; Clarke, C. J.; Licence, P., Acidity and basicity of halometallate-based ionic liquids from X-ray photoelectron spectroscopy. *RSC Advances* **2013,** *3* (24), 9436-9445.

171. Villar-Garcia, I. J.; Lovelock, K. R. J.; Men, S.; Licence, P., Tuning the electronic environment of cations and anions using ionic liquid mixtures. *Chem. Sci.* **2014,** *5* (6), 2573-2579.
172. Blundell, R. K.; Licence, P., Quaternary ammonium and phosphonium based ionic liquids: a comparison of common anions. *Phys Chem Chem Phys* **2014,** *16* (29), 15278-88.
173. Blundell, R. K.; Licence, P., Tuning cation-anion interactions in ionic liquids by changing the conformational flexibility of the cation. *Chem Commun (Camb)* **2014,** *50* (81), 12080-3.
174. Men, S.; Mitchell, D. S.; Lovelock, K. R. J.; Licence, P., X-ray Photoelectron Spectroscopy of Pyridinium-Based Ionic Liquids: Comparison to Imidazolium- and Pyrrolidinium-Based Analogues. *Chemphyschem* **2015,** *16* (10), 2211-8.
175. Longo, L. S.; Smith, E. F.; Licence, P., Study of the Stability of 1-Alkyl-3-methylimidazolium Hexafluoroantimonate(V) Based Ionic Liquids Using X-ray Photoelectron Spectroscopy. *ACS Sustainable Chemistry & Engineering* **2016,** *4* (11), 5953-5962.
176. Men, S.; Lovelock, K. R. J.; Licence, P., X-ray photoelectron spectroscopy of trihalide ionic liquids: Comparison to halide-based analogues, anion basicity and beam damage. *Chemical Physics Letters* **2017,** *679*, 207-211.
177. Men, S.; Licence, P.; Do-Thanh, C.-L.; Luo, H.; Dai, S., X-ray photoelectron spectroscopy of piperidinium ionic liquids: a comparison to the charge delocalised pyridinium analogues. *Physical Chemistry Chemical Physics* **2020,** *22* (21), 11976-11983.
178. Men, S.; Licence, P.; Luo, H.; Dai, S., Tuning the Cation-Anion Interactions by Methylation of the Pyridinium Cation: An X-ray Photoelectron Spectroscopy Study of Picolinium Ionic Liquids. *J Phys Chem B* **2020,** *124* (30), 6657-6663.
179. Santos, A. R.; Blundell, R. K.; Licence, P., XPS of guanidinium ionic liquids: a comparison of charge distribution in nitrogenous cations. *Phys Chem Chem Phys* **2015,** *17* (17), 11839-47.
180. Santos, A. R.; Hanson-Heine, M. W. D.; Besley, N. A.; Licence, P., The impact of sulfur functionalisation on nitrogen-based ionic liquid cations. *Chem Commun (Camb)* **2018,** *54* (81), 11403-11406.

181. Clarke, C. J.; Maxwell-Hogg, S.; Smith, E. F.; Hawker, R. R.; Harper, J. B.; Licence, P., Resolving X-ray photoelectron spectra of ionic liquids with difference spectroscopy. *Phys Chem Chem Phys* **2019,** *21* (1), 114-123.

182. Dick, E. J.; Fouda, A. E. A.; Besley, N. A.; Licence, P., Probing the electronic structure of ether functionalised ionic liquids using X-ray photoelectron spectroscopy. *Phys Chem Chem Phys* **2020,** *22* (3), 1624-1631.

183. Apperley, D. C.; Hardacre, C.; Licence, P.; Murphy, R. W.; Plechkova, N. V.; Seddon, K. R.; Srinivasan, G.; Swadzba-Kwasny, M.; Villar-Garcia, I. J., Speciation of chloroindate(III) ionic liquids. *Dalton Trans* **2010,** *39* (37), 8679-87.

184. Taylor, A. W.; Qiu, F.; Villar-Garcia, I. J.; Licence, P., Spectroelectrochemistry at ultrahigh vacuum: in situ monitoring of electrochemically generated species by X-ray photoelectron spectroscopy. *Chem Commun (Camb)* **2009,** (39), 5817-9.

185. Men, S.; Lovelock, K. R. J.; Licence, P., Directly probing the effect of the solvent on a catalyst electronic environment using X-ray photoelectron spectroscopy. *RSC Advances* **2015,** *5* (45), 35958-35965.

186. Men, S.; Jiang, J., X-ray photoelectron spectroscopy as a probe of the interaction between rhodium acetate and ionic liquids. *Chemical Physics Letters* **2016,** *646*, 125-129.

187. Men, S.; Lovelock, K. R. J.; Licence, P., X-ray photoelectron spectroscopy as a probe of rhodium-ligand interaction in ionic liquids. *Chemical Physics Letters* **2016,** *645*, 53-58.

188. Men, S.; Jiang, J., Probing the impact of the cation acidity on the cation-anion interaction in ionic liquids by X-ray photoelectron spectroscopy. *Chemical Physics Letters* **2017,** *677*, 60-64.

189. Men, S.; Jiang, J.; Licence, P., Spectroscopic analysis of 1-butyl-2,3-dimethylimidazolium ionic liquids: Cation-anion interactions. *Chemical Physics Letters* **2017,** *674*, 86-89.

190. Men, S.; Jiang, J.; Liu, Y., X-Ray Photoelectron Spectroscopy of Imidazolium Zwitterionic Salts: Comparison to Acetate Analogs and the Impact of the Alkyl Chain Length on the Charge Distribution. *Journal of Applied Spectroscopy* **2017,** *84* (5), 906-910.

191. Men, S.; Licence, P., Tuning the electronic environment of the anion by using binary ionic liquid mixtures. *Chemical Physics Letters* **2017,** *681*, 40-43.

192. Men, S.; Licence, P., Probing the electronic environment of binary and ternary ionic liquid mixtures by X-ray photoelectron spectroscopy. *Chemical Physics Letters* **2017,** *686*, 74-77.

193. Liu, Y.; Ma, C.; Men, S.; Jin, Y., An investigation of trioctylmethylammonium ionic liquids by X-ray photoelectron spectroscopy: The cation-anion interaction. *J Electron Spectrosc* **2018,** *223*, 79-83.

194. Men, S.; Jiang, J., Probing the Formation of the NHC-Palladium Species in Ionic Liquids by X-ray Photoelectron Spectroscopy. *Russian Journal of Physical Chemistry A* **2018,** *92* (8), 1627-1630.

195. Men, S.; Jiang, J., X-Ray Photoelectron Spectroscopy of Chlorometallate Ionic Liquids: Speciation and Anion Basicity. *Journal of Applied Spectroscopy* **2018,** *85* (1), 55-60.

196. Men, S.; Jin, Y., X-ray Photoelectron Spectroscopy of Imidazolium-Based Zwitterions: The Intramolecular Charge-Transfer Effect. *Russian Journal of Physical Chemistry A* **2018,** *92* (11), 2337-2340.

197. Men, S.; Rong, J.; Zhang, T.; Wang, X.; Feng, L.; Liu, C.; Jin, Y., Spectroscopic Analysis of 1-Butyl-3-methylimidazolium Ionic Liquids: Selection of the Charge Reference and the Electronic Environment. *Russian Journal of Physical Chemistry A* **2018,** *92* (10), 1975-1979.

198. Liu, Y.; Chen, X.; Men, S.; Licence, P.; Xi, F.; Ren, Z.; Zhu, W., The impact of cation acidity and alkyl substituents on the cation-anion interactions of 1-alkyl-2,3-dimethylimidazolium ionic liquids. *Phys Chem Chem Phys* **2019,** *21* (21), 11058-11065.

199. Wei, L.; Men, S., X-ray Photoelectron Spectroscopy of 1-Butyl-2,3-Dimethylimidazolium Ionic Liquids: Charge Correction Methods and Electronic Environment of the Anion. *Russian Journal of Physical Chemistry A* **2020,** *93* (13), 2676-2680.

200. He, Y.; Men, S., Charge Distribution of Phosphonium Ionic Liquids: Phosphonium versus Phosphate. *Russian Journal of Physical Chemistry A* **2020,** *94* (10), 2091-2095.

201. Men, S.; Jin, Y.; Licence, P., Probing the impact of the N3-substituted alkyl chain on the electronic environment of the cation and the anion for 1,3-dialkylimidazolium ionic liquids. *Phys Chem Chem Phys* **2020,** *22* (30), 17394-17400.

202. Mu, R.; Deng, A.; Men, S., Tribromide Ionic Liquids: Probing the Charge Distribution of the Anion by XPS. *Russian Journal of Physical Chemistry A* **2020,** *94* (5), 1053-1056.

203. Wei, L.; Wang, S.; Men, S., Electronic Effects in the Structure of 1-Ethyl-3-Methylimidazolium Ionic Liquids. *Russian Journal of Physical Chemistry A* **2021,** *95* (4), 736-740.
204. Taccardi, N.; Niedermaier, I.; Maier, F.; Steinrück, H. P.; Wasserscheid, P., Cyclic thiouronium ionic liquids: physicochemical properties and their electronic structure probed by X-ray induced photoelectron spectroscopy. *Chemistry* **2012,** *18* (27), 8288-91.
205. Heller, B. S. J.; Kolbeck, C.; Niedermaier, I.; Dommer, S.; Schatz, J.; Hunt, P.; Maier, F.; Steinrück, H. P., Surface Enrichment in Equimolar Mixtures of Non-Functionalized and Functionalized Imidazolium-Based Ionic Liquids. *Chemphyschem* **2018,** *19* (14), 1733-1745.
206. Reinmöller, M.; Ulbrich, A.; Ikari, T.; Preiss, J.; Höfft, O.; Endres, F.; Krischok, S.; Beenken, W. J., Theoretical reconstruction and elementwise analysis of photoelectron spectra for imidazolium-based ionic liquids. *Phys Chem Chem Phys* **2011,** *13* (43), 19526-33.
207. Fogarty, R. M.; Rowe, R.; Matthews, R. P.; Clough, M. T.; Ashworth, C. R.; Brandt, A.; Corbett, P. J.; Palgrave, R. G.; Smith, E. F.; Bourne, R. A.; Chamberlain, T. W.; Thompson, P. B. J.; Hunt, P. A.; Lovelock, K. R. J., Atomic charges of sulfur in ionic liquids: experiments and calculations. *Faraday Discuss* **2017,** *206*, 183-201.
208. Fogarty, R. M.; Matthews, R. P.; Ashworth, C. R.; Brandt-Talbot, A.; Palgrave, R. G.; Bourne, R. A.; Vander Hoogerstraete, T.; Hunt, P. A.; Lovelock, K. R. J., Experimental validation of calculated atomic charges in ionic liquids. *J Chem Phys* **2018,** *148* (19), 193817.
209. Rangan, S.; Viereck, J.; Bartynski, R. A., Electronic Properties of Cyano Ionic Liquids: a Valence Band Photoemission Study. *The Journal of Physical Chemistry B* **2020,** *124* (36), 7909-7917.
210. Dhungana, K. B.; Faria, L. F.; Wu, B.; Liang, M.; Ribeiro, M. C.; Margulis, C. J.; Castner, E. W., Jr., Structure of cyano-anion ionic liquids: X-ray scattering and simulations. *J Chem Phys* **2016,** *145* (2), 024503.
211. Liu, J.; Zhang, H.; Li, Y.; Liu, Z., Disorder in Aqueous Solutions and Peak Broadening in X-ray Photoelectron Spectroscopy. *J Phys Chem B* **2018,** *122* (46), 10600-10606.
212. Sprenger, D.; Anderson, O., Deconvolution of XPS spectra. *Fresenius' Journal of Analytical Chemistry* **1991,** *341* (1-2), 116-120.

213. Fuggle, J. C.; Alvarado, S. F., Core-level lifetimes as determined by x-ray photoelectron spectroscopy measurements. *Physical Review A* **1980,** *22* (4), 1615-1624.

214. Lundholm, M.; Siegbahn, H.; Holmberg, S.; Arbman, M., Core electron spectroscopy of water solutions. *J Electron Spectrosc* **1986,** *40* (2), 163-180.

215. Winter, B.; Aziz, E. F.; Hergenhahn, U.; Faubel, M.; Hertel, I. V., Hydrogen bonds in liquid water studied by photoelectron spectroscopy. *J Chem Phys* **2007,** *126* (12), 124504.

216. Pensado, A. S.; Brehm, M.; Thar, J.; Seitsonen, A. P.; Kirchner, B., Effect of dispersion on the structure and dynamics of the ionic liquid 1-ethyl-3-methylimidazolium thiocyanate. *Chemphyschem* **2012,** *13* (7), 1845-53.

217. Campetella, M.; Macchiagodena, M.; Gontrani, L.; Kirchner, B., Effect of alkyl chain length in protic ionic liquids: an AIMD perspective. *Molecular Physics* **2017,** *115* (13), 1582-1589.

218. Kiefer, J.; Noack, K.; Penna, T. C.; Ribeiro, M. C. C.; Weber, H.; Kirchner, B., Vibrational signatures of anionic cyano groups in imidazolium ionic liquids. *Vibrational Spectroscopy* **2017,** *91*, 141-146.

219. Cassone, G.; Sponer, J.; Saija, F., Ab Initio Molecular Dynamics Studies of the Electric-Field-Induced Catalytic Effects on Liquids. *Topics in Catalysis* **2021**.

220. Brehm, M.; Weber, H.; Pensado, A. S.; Stark, A.; Kirchner, B., Liquid Structure and Cluster Formation in Ionic Liquid/Water Mixtures – An Extensive ab initio Molecular Dynamics Study on 1-Ethyl-3-Methylimidazolium Acetate/Water Mixtures – Part. *Zeitschrift für Physikalische Chemie* **2013,** *227* (2-3), 177-204.

221. Brussel, M.; Brehm, M.; Voigt, T.; Kirchner, B., Ab initio molecular dynamics simulations of a binary system of ionic liquids. *Phys Chem Chem Phys* **2011,** *13* (30), 13617-20.

222. Payal, R. S.; Balasubramanian, S., Dissolution of cellulose in ionic liquids: an ab initio molecular dynamics simulation study. *Phys Chem Chem Phys* **2014,** *16* (33), 17458-65.

223. Zahn, S.; Brehm, M.; Brüssel, M.; Hollóczki, O.; Kohagen, M.; Lehmann, S.; Malberg, F.; Pensado, A. S.; Schöppke, M.; Weber, H.; Kirchner, B., Understanding ionic liquids from theoretical methods. *Journal of Molecular Liquids* **2014,** *192*, 71-76.

224. Ghatee, M. H.; Ansari, Y., Ab initio molecular dynamics simulation of ionic liquids. *J Chem Phys* **2007,** *126* (15), 154502.

225. Bhargava, B. L.; Yasaka, Y.; Klein, M. L., Hydrogen evolution from formic acid in an ionic liquid solvent: a mechanistic study by ab initio molecular dynamics. *J Phys Chem B* **2011,** *115* (48), 14136-40.

226. Goel, H.; Windom, Z. W.; Jackson, A. A.; Rai, N., CO2 sorption in triethyl(butyl)phosphonium 2-cyanopyrrolide ionic liquid via first principles simulations. *Journal of Molecular Liquids* **2019,** *292*, 111323.

227. Clarke-Hannaford, J.; Breedon, M.; Rüther, T.; Spencer, M. J. S., Stability of Boronium Cation-Based Ionic Liquid Electrolytes on the Li Metal Anode Surface. *ACS Applied Energy Materials* **2020,** *3* (6), 5497-5509.

228. Esser, L.; Macchieraldo, R.; Elfgen, R.; Sieland, M.; Smarsly, B. M.; Kirchner, B., TiCl4 Dissolved in Ionic Liquid Mixtures from ab Initio Molecular Dynamics Simulations. *Molecules* **2021,** *26* (1), 79.

229. Almeida, H. F. D.; Canongia Lopes, J. N.; Rebelo, L. P. N.; Coutinho, J. A. P.; Freire, M. G.; Marrucho, I. M., Densities and Viscosities of Mixtures of Two Ionic Liquids Containing a Common Cation. *Journal of Chemical & Engineering Data* **2016,** *61* (8), 2828-2843.

230. Seddon, K. R.; Stark, A.; Torres, M.-J., Viscosity and Density of 1-Alkyl-3-methylimidazolium Ionic Liquids. In *Clean Solvents - Alternative Media for Chemical Reactions and Processing*, Abraham, M. A.; Moens, L., Eds. American Chemical Society: Washington, **2002**; pp 34-49.

231. Seidel, R.; Pohl, M. N.; Ali, H.; Winter, B.; Aziz, E. F., Advances in liquid phase soft-x-ray photoemission spectroscopy: A new experimental setup at BESSY II. *Rev Sci Instrum* **2017,** *88* (7), 073107.

232. Haghani, A.; Hoffmann, M. M.; Iloukhani, H., Density, Speed of Sound, and Refractive Index of Binary Mixtures of 1-Butyl-3-methylimidazolium Thiocyanate + 2-Alkanols (C3–C6) at Different Temperatures T = (288.15-338.15) K. *Journal of Chemical & Engineering Data* **2021,** *66* (5), 1956-1969.

233. Grimme, S., Accurate description of van der Waals complexes by density functional theory including empirical corrections. *J Comput Chem* **2004,** *25* (12), 1463-73.

234. Frisch, M. J.; Trucks, G. W.; Schlegel, H. B.; Scuseria, G. E.; Robb, M. A.; Cheeseman, J. R.; Scalmani, G.; Barone, V.; Petersson, G. A.; Nakatsuji, H.; Li, X.; Caricato, M.; Marenich, A. V.; Bloino, J.; Janesko, B. G.; Gomperts, R.; Mennucci, B.; Hratchian, H. P.; Ortiz, J. V.; Izmaylov, A. F.; Sonnenberg, J. L.; Williams; Ding, F.; Lipparini, F.; Egidi, F.; Goings, J.; Peng, B.; Petrone, A.; Henderson, T.; Ranasinghe, D.; Zakrzewski, V. G.; Gao, J.; Rega, N.; Zheng, G.; Liang, W.; Hada, M.; Ehara, M.; Toyota, K.; Fukuda, R.; Hasegawa, J.; Ishida, M.; Nakajima, T.; Honda, Y.; Kitao, O.; Nakai, H.; Vreven, T.; Throssell, K.; Montgomery Jr., J. A.; Peralta, J. E.; Ogliaro, F.; Bearpark, M. J.; Heyd, J. J.; Brothers, E. N.; Kudin, K. N.; Staroverov, V. N.; Keith, T. A.; Kobayashi, R.; Normand, J.; Raghavachari, K.; Rendell, A. P.; Burant, J. C.; Iyengar, S. S.; Tomasi, J.; Cossi, M.; Millam, J. M.; Klene, M.; Adamo, C.; Cammi, R.; Ochterski, J. W.; Martin, R. L.; Morokuma, K.; Farkas, O.; Foresman, J. B.; Fox, D. J. *Gaussian 16 Rev. C.01*, Gaussian, Inc.: Wallingford, CT, **2016**.

235. Petersson, G. A.; Al-Laham, M. A., A complete basis set model chemistry. II. Open-shell systems and the total energies of the first-row atoms. *The Journal of Chemical Physics* **1991,** *94* (9), 6081-6090.

236. Petersson, G. A.; Bennett, A.; Tensfeldt, T. G.; Al-Laham, M. A.; Shirley, W. A.; Mantzaris, J., A complete basis set model chemistry. I. The total energies of closed-shell atoms and hydrides of the first-row elements. *The Journal of Chemical Physics* **1988,** *89* (4), 2193-2218.

237. Jain, V.; Biesinger, M. C.; Linford, M. R., The Gaussian-Lorentzian Sum, Product, and Convolution (Voigt) functions in the context of peak fitting X-ray photoelectron spectroscopy (XPS) narrow scans. *Applied Surface Science* **2018,** *447*, 548-553.

238. Fogarty, R. M.; Palgrave, R. G.; Bourne, R. A.; Handrup, K.; Villar-Garcia, I. J.; Payne, D. J.; Hunt, P. A.; Lovelock, K. R. J., Electron spectroscopy of ionic liquids: experimental identification of atomic orbital contributions to valence electronic structure. *Phys Chem Chem Phys* **2019,** *21* (35), 18893-18910.

239. Pi, J. M.; Stella, M.; Fernando, N. K.; Lam, A. Y.; Regoutz, A.; Ratcliff, L. E., Predicting Core Level Photoelectron Spectra of Amino Acids Using Density Functional Theory. *J Phys Chem Lett* **2020,** *11* (6), 2256-2262.

240. Heid, E.; Szabadi, A.; Schroder, C., Quantum mechanical determination of atomic polarizabilities of ionic liquids. *Phys Chem Chem Phys* **2018,** *20* (16), 10992-10996.

241. Low, K.; Tan, S. Y. S.; Izgorodina, E. I., An ab initio Study of the Structure and Energetics of Hydrogen Bonding in Ionic Liquids. *Front Chem* **2019,** *7*, 208.

242. Holbrey, J. D.; Rogers, R. D.; Mantz, R. A.; Trulove, P. C.; Cocalia, V. A.; Visser, A. E.; Anderson, J. L.; Anthony, J. L.; Brennecke, J. F.; Maginn, E. J.; Welton, T.; Mantz, R. A., Physicochemical Properties. In *Ionic Liquids in Synthesis*, **2007**; pp 57-174.

243. Vila, J.; Varela, L. M.; Cabeza, O., Cation and anion sizes influence in the temperature dependence of the electrical conductivity in nine imidazolium based ionic liquids. *Electrochimica Acta* **2007,** *52* (26), 7413-7417.

244. Stoppa, A.; Zech, O.; Kunz, W.; Buchner, R., The Conductivity of Imidazolium-Based Ionic Liquids from (−35 to 195) °C. A. Variation of Cation's Alkyl Chain. *Journal of Chemical & Engineering Data* **2009,** *55* (5), 1768-1773.

245. Crowhurst, L.; Falcone, R.; Lancaster, N. L.; Llopis-Mestre, V.; Welton, T., Using Kamlet-Taft solvent descriptors to explain the reactivity of anionic nucleophiles in ionic liquids. *J Org Chem* **2006,** *71* (23), 8847-53.

246. Spange, S.; Lungwitz, R.; Schade, A., Correlation of molecular structure and polarity of ionic liquids. *Journal of Molecular Liquids* **2014,** *192*, 137-143.

247. Lungwitz, R.; Friedrich, M.; Linert, W.; Spange, S., New aspects on the hydrogen bond donor (HBD) strength of 1-butyl-3-methylimidazolium room temperature ionic liquids. *New Journal of Chemistry* **2008,** *32* (9).

248. Nieto de Castro, C. A.; Langa, E.; Morais, A. L.; Lopes, M. L. M.; Lourenço, M. J. V.; Santos, F. J. V.; Santos, M. S. C. S.; Lopes, J. N. C.; Veiga, H. I. M.; Macatrão, M.; Esperança, J. M. S. S.; Marques, C. S.; Rebelo, L. P. N.; Afonso, C. A. M., Studies on the density, heat capacity, surface tension and infinite dilution diffusion with the ionic liquids [C4mim][NTf2], [C4mim][dca], [C2mim][EtOSO3] and [Aliquat][dca]. *Fluid Phase Equilibria* **2010,** *294* (1-2), 157-179.

249. Gardas, R. L.; Freire, M. G.; Carvalho, P. J.; Marrucho, I. M.; Fonseca, I. M. A.; Ferreira, A. G. M.; Coutinho, J. A. P., PρT Measurements of Imidazolium-Based Ionic Liquids. *Journal of Chemical & Engineering Data* **2007,** *52* (5), 1881-1888.

250. Mac Dowell, N.; Llovell, F.; Sun, N.; Hallett, J. P.; George, A.; Hunt, P. A.; Welton, T.; Simmons, B. A.; Vega, L. F., New experimental density data and soft-SAFT models of alkylimidazolium ([C(n)C(1)im](+)) chloride (Cl(-)), methylsulfate ([MeSO(4)](-)), and dimethylphosphate ([Me(2)PO(4)](-)) based ionic liquids. *J Phys Chem B* **2014,** *118* (23), 6206-21.

251. AlTuwaim, M. S.; Alkhaldi, K. H. A. E.; Al-Jimaz, A. S.; Mohammad, A. A., Temperature Dependence of Physicochemical Properties of Imidazolium-, Pyroldinium-, and Phosphonium-Based Ionic Liquids. *Journal of Chemical & Engineering Data* **2014,** *59* (6), 1955-1963.

252. Almantariotis, D.; Pensado, A. S.; Gunaratne, H. Q.; Hardacre, C.; Padua, A. A.; Coxam, J. Y.; Costa Gomes, M. F., Influence of Fluorination on the Solubilities of Carbon Dioxide, Ethane, and Nitrogen in 1-n-Fluoro-alkyl-3-methylimidazolium Bis(n-fluoroalkylsulfonyl)amide Ionic Liquids. *J Phys Chem B* **2017,** *121* (2), 426-436.

253. Khalil, R.; Chaabene, N.; Azar, M.; Malham, I. B.; Turmine, M., Effect of the chain lengthening on transport properties of imidazolium-based ionic liquids. *Fluid Phase Equilibria* **2020,** *503*.

254. Pandit, S. A.; Rather, M. A.; Bhat, S. A.; Rather, G. M.; Bhat, M. A., Influence of the Anion on the Equilibrium and Transport Properties of 1-Butyl-3-methylimidazolium Based Room Temperature Ionic Liquids. *Journal of Solution Chemistry* **2016,** *45* (12), 1641-1658.

255. Harris, K. R.; Kanakubo, M.; Woolf, L. A., Temperature and Pressure Dependence of the Viscosity of the Ionic Liquids 1-Hexyl-3-methylimidazolium Hexafluorophosphate and 1-Butyl-3-methylimidazolium Bis(trifluoromethylsulfonyl)imide. *Journal of Chemical & Engineering Data* **2007,** *52* (3), 1080-1085.

256. Martins, M. A. R.; Sharma, G.; Pinho, S. P.; Gardas, R. L.; Coutinho, J. A. P.; Carvalho, P. J., Selection and characterization of non-ideal ionic liquids mixtures to be used in CO2 capture. *Fluid Phase Equilibria* **2020,** *518*.

257. Tu, J.; Song, W. L.; Lei, H.; Yu, Z.; Chen, L. L.; Wang, M.; Jiao, S., Nonaqueous Rechargeable Aluminum Batteries: Progresses, Challenges, and Perspectives. *Chem Rev* **2021,** *121* (8), 4903-4961.

258. Eliseeva, S. V.; Bunzli, J. C., Lanthanide luminescence for functional materials and bio-sciences. *Chem Soc Rev* **2010,** *39* (1), 189-227.

259. Zhong, C.; Deng, Y.; Hu, W.; Qiao, J.; Zhang, L.; Zhang, J., A review of electrolyte materials and compositions for electrochemical supercapacitors. *Chem Soc Rev* **2015,** *44* (21), 7484-539.

260. Beguin, F.; Presser, V.; Balducci, A.; Frackowiak, E., Carbons and electrolytes for advanced supercapacitors. *Adv Mater* **2014,** *26* (14), 2219-51, 2283.

261. Simon, P.; Gogotsi, Y., Capacitive energy storage in nanostructured carbon-electrolyte systems. *Acc Chem Res* **2013,** *46* (5), 1094-103.

262. Dubal, D. P.; Chodankar, N. R.; Kim, D. H.; Gomez-Romero, P., Towards flexible solid-state supercapacitors for smart and wearable electronics. *Chem Soc Rev* **2018,** *47* (6), 2065-2129.

263. Liu, C.; Yu, Z.; Neff, D.; Zhamu, A.; Jang, B. Z., Graphene-based supercapacitor with an ultrahigh energy density. *Nano Lett* **2010,** *10* (12), 4863-8.

264. MacFarlane, D. R.; Forsyth, M.; Howlett, P. C.; Pringle, J. M.; Sun, J.; Annat, G.; Neil, W.; Izgorodina, E. I., Ionic liquids in electrochemical devices and processes: managing interfacial electrochemistry. *Acc Chem Res* **2007,** *40* (11), 1165-73.

265. MacFarlane, D. R.; Forsyth, M.; Howlett, P. C.; Kar, M.; Passerini, S.; Pringle, J. M.; Ohno, H.; Watanabe, M.; Yan, F.; Zheng, W.; Zhang, S.; Zhang, J., Ionic liquids and their solid-state analogues as materials for energy generation and storage. *Nature Reviews Materials* **2016,** *1* (2).

266. MacFarlane, D. R.; Tachikawa, N.; Forsyth, M.; Pringle, J. M.; Howlett, P. C.; Elliott, G. D.; Davis, J. H.; Watanabe, M.; Simon, P.; Angell, C. A., Energy applications of ionic liquids. *Energy Environ. Sci.* **2014,** *7* (1), 232-250.

267. Yuan, M.; Liu, K., Rational design on separators and liquid electrolytes for safer lithium-ion batteries. *Journal of Energy Chemistry* **2020,** *43*, 58-70.

268. Karuppasamy, K.; Theerthagiri, J.; Vikraman, D.; Yim, C. J.; Hussain, S.; Sharma, R.; Maiyalagan, T.; Qin, J.; Kim, H. S., Ionic Liquid-Based Electrolytes for Energy Storage Devices: A Brief Review on Their Limits and Applications. *Polymers (Basel)* **2020,** *12* (4).

269. Kanan, S.; Moyet, M. A.; Arthur, R. B.; Patterson, H. H., Recent advances on TiO2-based photocatalysts toward the degradation of pesticides and major organic pollutants from water bodies. *Catalysis Reviews* **2019,** *62* (1), 1-65.

270. Chen, X., Titanium Dioxide Nanomaterials and Their Energy Applications. *Chinese Journal of Catalysis* **2009,** *30* (8), 839-851.

271. Kavan, L., Electrochemistry of titanium dioxide: some aspects and highlights. *Chem Rec* **2012,** *12* (1), 131-42.

272. Abdullah, N.; Kamarudin, S. K., Titanium dioxide in fuel cell technology: An overview. *Journal of Power Sources* **2015,** *278*, 109-118.

273. Chen, X.; Shen, S.; Guo, L.; Mao, S. S., Semiconductor-based photocatalytic hydrogen generation. *Chem Rev* **2010,** *110* (11), 6503-70.

274. Bourikas, K.; Kordulis, C.; Lycourghiotis, A., Titanium dioxide (anatase and rutile): surface chemistry, liquid-solid interface chemistry, and scientific synthesis of supported catalysts. *Chem Rev* **2014,** *114* (19), 9754-823.

275. Qi, K.; Li, D.; Fu, J.; Zhu, L.; Duan, X.; Qin, Q.; Wang, G.; Zheng, W., Elucidating Ionic Liquid Environments That Affect the Morphology of TiO2 Nanocrystals: A DFT+D Study. *The Journal of Physical Chemistry C* **2014,** *118* (40), 23320-23327.

276. Pensado, A. S.; Malberg, F.; Gomes, M. F. C.; Pádua, A. A. H.; Fernández, J.; Kirchner, B., Interactions and structure of ionic liquids on graphene and carbon nanotubes surfaces. *RSC Adv.* **2014,** *4* (35), 18017-18024.

277. Weber, H.; Bredow, T.; Kirchner, B., Adsorption Behavior of the 1,3-Dimethylimidazolium Thiocyanate and Tetracyanoborate Ionic Liquids at Anatase (101) Surface. *The Journal of Physical Chemistry C* **2015,** *119* (27), 15137-15149.

278. Du Hill, L.; De Keersmaecker, M.; Colbert, A. E.; Hill, J. W.; Placencia, D.; Boercker, J. E.; Armstrong, N. R.; Ratcliff, E. L., Rationalizing energy level alignment by characterizing Lewis

acid/base and ionic interactions at printable semiconductor/ionic liquid interfaces. *Mater Horiz* **2022,** *9* (1), 471-481.

279. Freire, M. G.; Teles, A. R. R.; Rocha, M. A. A.; Schröder, B.; Neves, C. M. S. S.; Carvalho, P. J.; Evtuguin, D. V.; Santos, L. M. N. B. F.; Coutinho, J. A. P., Thermophysical Characterization of Ionic Liquids Able To Dissolve Biomass. *Journal of Chemical & Engineering Data* **2011,** *56* (12), 4813-4822.

280. Samsonov, G. V., *The Oxide Handbook*. **1973**.

281. Kirby, R. K., Thermal Expansion of Rutile from 100 to 700 degrees K. *J Res Natl Bur Stand A Phys Chem* **1967,** *71A* (5), 363-369.

282. Lee, T.-L.; Duncan, D. A., A Two-Color Beamline for Electron Spectroscopies at Diamond Light Source. *Synchrotron Radiation News* **2018,** *31* (4), 16-22.

283. Zegenhagen, J., X-ray standing waves technique: Fourier imaging active sites. *Japanese Journal of Applied Physics* **2019,** *58* (11).

284. Hunt, P. A.; Kirchner, B.; Welton, T., Characterising the electronic structure of ionic liquids: an examination of the 1-butyl-3-methylimidazolium chloride ion pair. *Chemistry* **2006,** *12* (26), 6762-75.

285. Matthews, R. P.; Welton, T.; Hunt, P. A., Competitive pi interactions and hydrogen bonding within imidazolium ionic liquids. *Phys Chem Chem Phys* **2014,** *16* (7), 3238-53.

286. Hunt, P. A.; Gould, I. R.; Kirchner, B., The Structure of Imidazolium-Based Ionic Liquids: Insights From Ion-Pair Interactions. *Australian Journal of Chemistry* **2007,** *60* (1).

287. Skarmoutsos, I.; Dellis, D.; Matthews, R. P.; Welton, T.; Hunt, P. A., Hydrogen bonding in 1-butyl- and 1-ethyl-3-methylimidazolium chloride ionic liquids. *J Phys Chem B* **2012,** *116* (16), 4921-33.

288. Housaindokht, M. R.; Hosseini, H. E.; Sadeghi Googheri, M. S.; Monhemi, H.; Najafabadi, R. I.; Ashraf, N.; Gholizadeh, M., Hydrogen bonding investigation in 1-ethyl-3-methylimidazolium based ionic liquids from density functional theory and atoms-in-molecules methods. *Journal of Molecular Liquids* **2013,** *177*, 94-101.

289. Watanabe, H.; Doi, H.; Saito, S.; Matsugami, M.; Fujii, K.; Kanzaki, R.; Kameda, Y.; Umebayashi, Y., Hydrogen bond in imidazolium based protic and aprotic ionic liquids. *Journal of Molecular Liquids* **2016,** *217*, 35-42.

290. Kempter, V.; Kirchner, B., The role of hydrogen atoms in interactions involving imidazolium-based ionic liquids. *Journal of Molecular Structure* **2010,** *972* (1-3), 22-34.

291. Weber, H.; Salanne, M.; Kirchner, B., Toward an Accurate Modeling of Ionic Liquid–TiO2 Interfaces. *The Journal of Physical Chemistry C* **2015,** *119* (45), 25260-25267.

292. Tsimpanogiannis, I. N.; Moultos, O. A.; Franco, L. F. M.; Spera, M. B. d. M.; Erdős, M.; Economou, I. G., Self-diffusion coefficient of bulk and confined water: a critical review of classical molecular simulation studies. *Molecular Simulation* **2018,** *45* (4-5), 425-453.

Appendix

Effects of chain length, anion and temperature on X-ray photoelectron spectra of ionic liquids: supplementary information

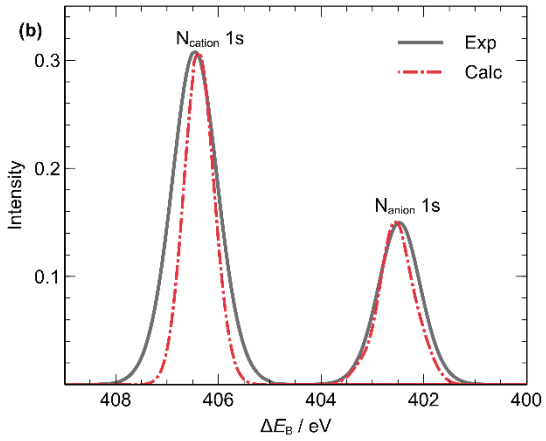

Figure A1 High resolution scan of N 1s peaks. The calculated peaks were broadened with a 0.5 eV width. Computed peaks shifted +27.00 eV for charge referencing to $E_B(C_{alkyl}\ 1s) = 289.58$ eV

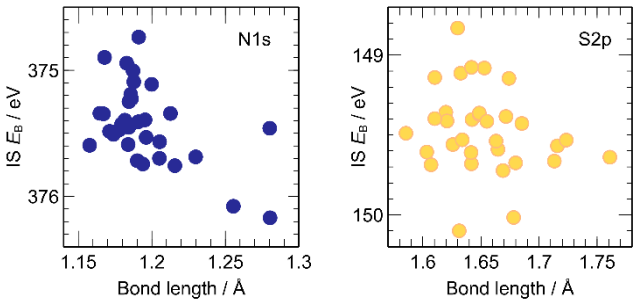

Figure A2 Plot of IS E_B with bond length for N_{anion} 1s (left, blue) and S 2p (right, yellow)

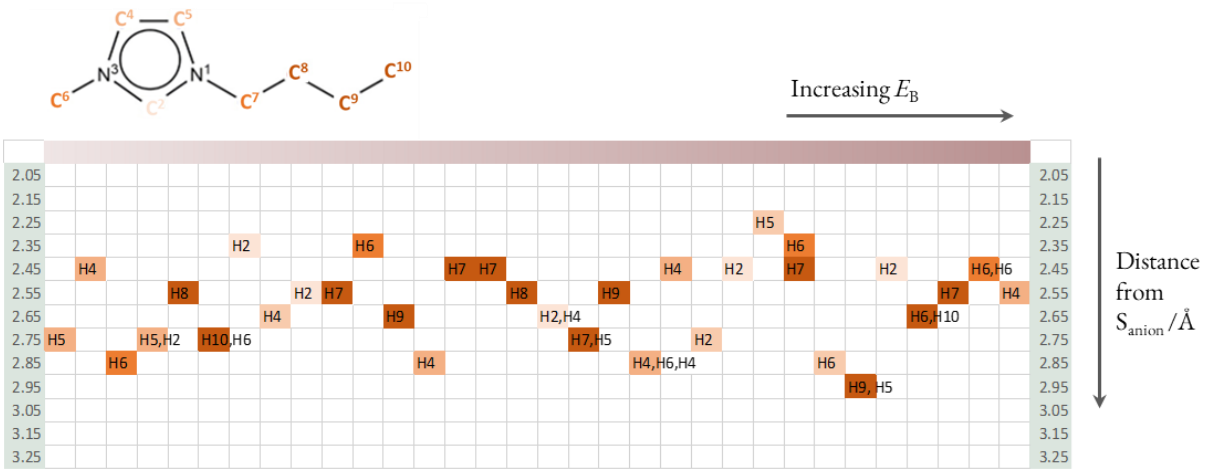

Figure A3 Scheme marking the closest cation atom to S_{anion} in $[C_4C_1Im][SCN]$, ordered from lowest E_B (left) to highest E_B (right) of S_{anion} 2p. Hydrogens labelled and coloured according to carbons in $[C_4C_1Im]^+$, illustrated top left.

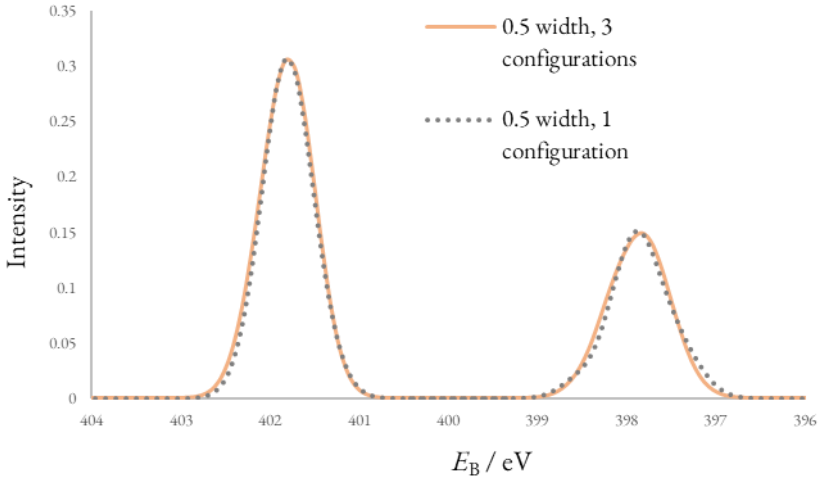

Figure A4 Plot of calculated high resolution N 1s spectrum from $[C_4C_1Im][SCN]$ using a data set of 3 configurations (orange) and 1 configuration (grey, dotted). Each configuration offers 64 data points for the N_{cation} and 32 data points for the N_{anion}. Width reduced to 0.5 eV to increase clarity of peak asymmetry.